TU Clausthal

Jakub Bibrzycki

Investigations of Coal Particle Combustion and Gasification

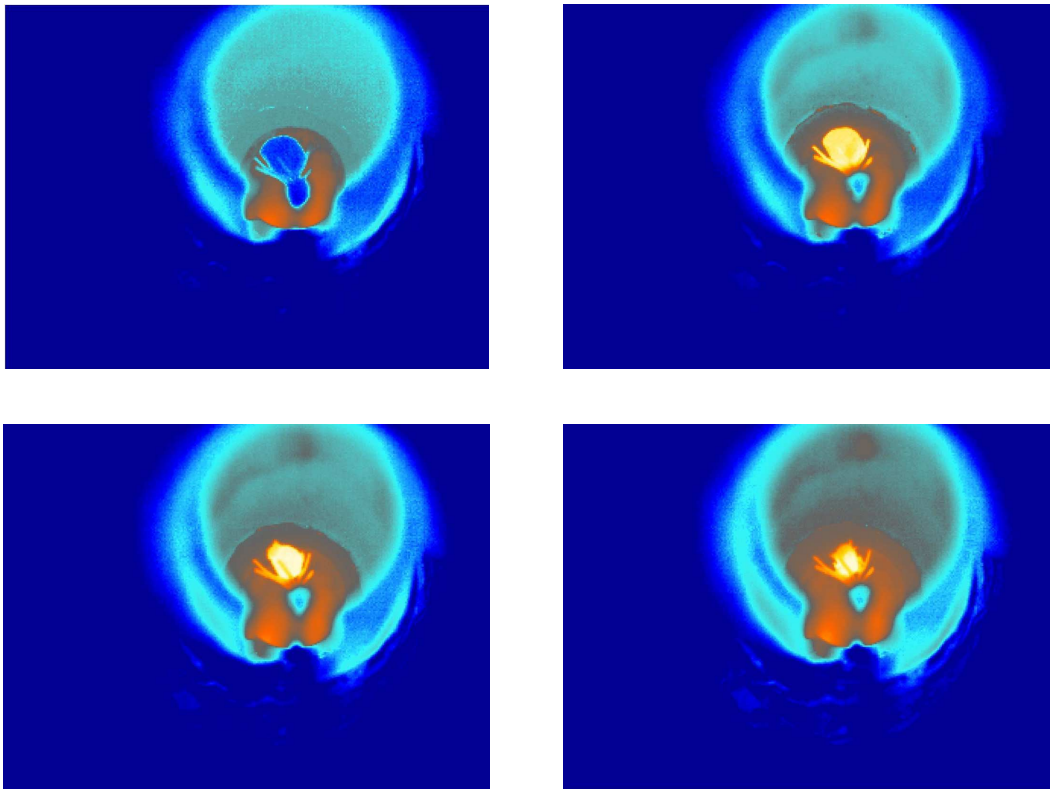

SILESIAN UNIVERSITY OF TECHNOLOGY
FACULTY OF ENVIRONMENTAL ENGINEERING AND ENERGY

CLAUSTHAL UNIVERSITY OF TECHNOLOGY
FACULTY OF ENERGY AND MANAGEMENT SCIENCE

INSTITUTE OF THERMAL TECHNOLOGY

INSTITUTE OF ENERGY PROCESS ENGINEERING
AND FUEL TECHNOLOGY

PH.D. THESIS

INVESTIGATIONS OF COAL PARTICLE COMBUSTION AND GASIFICATION

Author:
JAKUB BIBRZYCKI

This thesis was realized in the frame of the agreement between
Silesian University of Technology and Clausthal University of Technology

Final exam took place on 5th December 2014

GLIWICE & CLAUSTHAL-ZELLERFELD, 2015

Author:

Mgr inż. Jakub Bibrzycki
Silesian University of Technology
Faculty of Environmental Engineering
and Energy
Institute of Thermal Technology

Gliwice, Poland
jakub.bibrzycki@wp.pl

Dipl.-Ing. Jakub Bibrzycki
Clausthal University of Technology
Faculty of Energy and Management
Science
Institute of Energy Process Engineering
and Fuel Technology
Clausthal-Zellerfeld, Germany
jakub.bibrzycki@tu-clausthal.de

Chairman of the examination committee:

Prof. dr hab. inż. Zbigniew Popiołek
Silesian University of Technology
Faculty of Environmental Engineering
and Energy
Department of Heating, Ventilation
and Dust Removal Technology
Gliwice, Poland
zbigniew.popiolek@polsl.pl

Supervisors:

Prof. dr hab. inż. Andrzej Szlęk
Silesian University of Technology
Faculty of Environmental Engineering
and Energy
Institute of Thermal Technology

Gliwice, Poland
andrzej.szlek@polsl.pl

Prof. Dr.-Ing. Roman Weber
Clausthal University of Technology
Faculty of Energy and Management
Science
Institute of Energy Process Engineering
and Fuel Technology
Clausthal-Zellerfeld, Germany
roman.weber@ievb.tu-clausthal.de

Reviewers:

Dr hab. inż. Andrzej Strugała, prof. AGH
AGH University of Science and Technology
Faculty of Energy and Fuels
Department of Fuels Technology
Kraków, Poland
strugala@agh.edu.pl

Ao.Univ.Prof. Dipl.-Ing. Dr.techn. Franz Winter
Vienna University of Technology
Faculty of Technical Chemistry
Institute of Chemical Engineering
Vienna, Austria
franz.winter@tuwien.ac.at

Życie to ciągła walka z przeciwnościami losu i z samym sobą...

Nie można się poddawać, gdy istnieje chociaż iskierka nadziei na wygraną.

Każde zwycięstwo nas wzmacnia i daje siłę na kolejną bitwę.

Jakub Bibrzycki

Contents

List of Figures

List of Tables

Acknowledgements

First of all I would like to express my gratitude to promoters Prof. Andrzej Szlęk and Prof. Roman Weber. Prof. Andrzej Szlęk gave me opportunities to start this interesting topic. He had always good will to help me when it was needed and opened many doors of possibilities, especially at the very beginning of my journey with this project. Prof. Roman Weber on the other hand let out all the decks of his patience when correcting carefully my PhD thesis. Both professors gave me important advices and valuable remarks, without which I could not finish my work.

Invaluable assistance has been provided by Marco Mancini PhD, since I have come the first time to Clausthal. He helped me to develop the model in Ansys Fluent from the first sketch. He also assisted me during the zero-dimensional models improvement. For Marco Mancini continuous help and huge patience I would like to thanks hundredfold.

I would like to thank Anna Katelbach-Woźniak who was my best teacher in the field of thermo-gravimetric analysis. She always supported me and gave me many good advises when any kind of problem appeared with the TGA and also when the GTB test rig was being built. Moreover, I am grateful for her kind help when two people were needed sometimes to operate the GTB test rig.

I would also like to take this opportunity in thanking Anna Pajdak from the Institute of Advanced Energy Technologies, from the Częstochowa University of Technology, who carried out for me measurements using mercury porosimetry and to all colleagues from this Institute for their kindness.

I must thank Zygmunt Zieliński for his continuous help with retrofitting of the GTB test rig and for taking care of my safety during series of measurements.

I am also grateful for good advices regarding my work given by Sławomir Sładek and Rafał Buczyński. I would like also to thank Sławomir Sładek for some good photos shown in this thesis.

I would like to express my gratitude to Michael Alberti for the abstract translation into German and to Barbara Jagoda for careful corrections of Polish version of the abstract.

Special thanks to prof. Thierry Poinsot who was my supervisor during half-year training at the CERFACS/IMFT in Toulouse and besides teaching me basics of combustion kinetics also advised me to use Latex. Because of this advise this thesis looks much better than it could be if other software is used. Here, I would like to thank also to Sunil Patel and Steven Gunn, who created and shared Latex thesis template in the internet, which was very helpful when creating my own files.

It is not possible to forget the support of my parents, sister and some family members. They have been always ready to help me in different situations, since I was born. I am also grateful to all my friends for believing in me and making me to be more optimistic day by day.

And finally I would like to give my gratitude to each person from the Institute of Thermal Technology in Gliwice and from the Institute for Energy Process Engineering and Fuel Technology in Clausthal-Zellerfeld, who with good words or any other kind of support encouraged me to finish this work.

This work has been done with financial assistance within the frame of the statute research of the Institute of Thermal Technology, the Silesian University of Technology.

KAPITAŁ LUDZKI
NARODOWA STRATEGIA SPÓJNOŚCI

Author of this thesis is a beneficiary
of the project
*"DoktoRIS – Scholarship program
for innovative Silesia"*
co-financed by the European Union
from the European Social Fund.

UNIA EUROPEJSKA
EUROPEJSKI
FUNDUSZ SPOŁECZNY

Abstract

This work presents a comprehensive description of combustion phenomena of char particles, with dedication to fluidized bed combustion technology. This technology has many advantages, therefore a need of its further optimization exists. One of the largest energy losses in the fluidized bed boiler are associated with unburned carbon, which is found in a fly ash as well as in a slag. In order to minimize these loses, better mixing of fuel with air and prolongation of the residence time of coal particles in a high temperature region, are required.

Nowadays, to optimize processes in a furnace, CFD (Computational Fluid Dynamics) is often used. To take advantage of this method a mathematical model of the boiler has to be built. In such models, one of the most important input data are fuel conversion rates at various conditions. This information affects heat fluxes, temperature, flow field and many other variables, which are crucial for process optimization in the boiler. Therefore, delivering reliable information regarding coal particles combustion rates is essential.

The knowledge of single coal particle conversion rates is often delivered into CFD-based model by simple 0D particle combustion models. One of the major difficulties, occurring when this kind of models are being developed, is the reliable determination of kinetic constants for combustion and gasification processes. Additionally, the coal/char morphology has to be also determined, since it influences considerably combustion rates.

This work describes the path of obtaining combustion rates of a single char particle from basic investigations. The first basic investigation is the thermogravimetric analysis which delivers information about fuel conversion rates at different temperatures and controlled atmosphere. The second basic investigation performed within the present study is mercury porosimetry. From this investigation fuel porosity, specific surface area and particle density have been obtained. These two investigations allow for determination of Arrhenius constants, which describe the reactions rate of char with both oxygen and carbon dioxide.

On the basis of thermogravimetry and mercury porosimetry, several zero-dimensional models have been developed to be used in conjunction with CFD boiler models. These models have been validated with experimental data obtained from a newly built test rig (Grain Thermo-Balance (GTB) test rig), which allows for recording particle mass loss and particle surface temperature during combustion. Experimental conditions, in the GTB test rig, have been chosen to reflect, to some extent, these occurring in fluidized bed boilers. From the comparison of the experimental and modeling data the most suitable zero-dimensional model for fluidized bed combustion has been chosen.

In order to better understand the combustion and gasification processes of a single, few millimeters size, char particle, a transient two-dimensional mathematical model of 6 *mm*-size char particle has been developed so as to simulate the GTB test rig experiments. Time dependent temperature field, reactant concentration field and particle morphology changes with burnout are obtained and compared with the measured data. Generally a good agreement between the model predictions and the experimentally-obtained particle mass loss and particle surface temperatures have been obtained.

The main achievement of this thesis is the development of a methodology (a series of actions) needed for calculating conversion rates of millimeter size char particles. The methodology begins with TGA measurements of kinetically-controlled char conversion rates, which is followed by determination of particle morphology. On the basis of such information, zero-dimensional or multi-dimensional models can be developed depending on what is needed.

Streszczenie

W niniejszej pracy przedstawiono obszerny opis procesu spalania pojedynczej, kilkumilimetrowej cząstki koksiku, który może zostać wykorzystany w pracach nad ulepszeniem technologii fluidalnego spalania węgla. Technologia ta ma wiele zalet, dlatego też istnieje potrzeba jej dalszego rozwoju. Jedna z największych strat energii występujących w kotłach fluidalnych jest związana z niecałkowitym wypaleniem paliwa. Pierwiastkowy węgiel można znaleźć w popiele lotnym oraz w żużlu. Aby zminimalizować ilość niedopalonego koksiku, należy doprowadzić do lepszego wymieszania paliwa z powietrzem oraz do wydłużenia przebywania cząstek węgla w odpowiednio wysokiej temperaturze.

Obecnie do optymalizacji procesu spalania w kotle stosuje się często metody komputerowej symulacji (Computational Fluid Dynamics – CFD). Aby z nich skorzystać, należy utworzyć model matematyczny kotła. W tego rodzaju modelach najważniejszymi danymi wejściowymi są szybkości spalania paliwa w różnych warunkach. Dane te wpływają na strumienie ciepła, pola temperatury i prędkości oraz na wiele innych zmiennych, które są istotne w optymalizacji procesu spalania w kotle. Dlatego też podstawową kwestią jest dostarczenie do modelu wiarygodnych informacji określających szybkość spalania cząstki węgla.

Informacje na temat szybkości spalania pojedynczej cząstki węgla są dostarczane do modelu opartego na CFD przez proste, zerowymiarowe modele spalania cząstki paliwa. Najistotniejszą trudnością napotkaną podczas budowania takich modeli jest uzyskanie wiarygodnych stałych kinetycznych procesu spalania i zgazowania. Dodatkowo prawidłowe wyznaczenie morfologii koksiku/węgla jest niezwykle istotne, gdyż wpływa ona znacząco na szybkość spalania.

W niniejszej pracy opisano sposób uzyskiwania informacji dotyczących szybkości spalania pojedynczej cząstki koksiku z badań podstawowych. Pierwszym z tych badań jest analiza termograwimetryczna (TGA), która dostarcza informacji dotyczących szybkości wypalenia paliwa w różnych temperaturach, przy kontrolowanej atmosferze. Drugim badaniem podstawowym jest porozymetria rtęciowa pozwalająca na określenie porowatości, powierzchni właściwej i gęstości cząstki koksiku. Wymienione badania pozwalają na wyznaczenie parametrów równania Arrheniusa, które opisują szybkość zachodzenia reakcji koksiku z tlenem i dwutlenkiem węgla.

Na podstawie przeprowadzonej analizy termograwimetrycznej oraz badań przy użyciu porozymetru rtęciowego zbudowano kilka zerowymiarowych modeli spalania pojedynczej cząstki koksiku, które to mogą zostać użyte w modelach CFD kotła. Modele te następnie zostały zwalidowane poprzez wyniki otrzymane z badań eksperymentalnych przeprowadzonych na nowo zbudowanym stanowisku pomiarowym (Grain Thero-Balance – GTB), pozwalającym na ciągły pomiar masy cząstki paliwa oraz temperatury jej powierzchni podczas procesu spalania. Warunki

przeprowadzenia badań na tym stanowisku pomiarowym zostały dobrane tak, aby w pewnym stopniu odzwierciedlały te panujące w kotłach fluidalnych. Z porównania wyników badań eksperymentalnych i danych otrzymanych z modeli wybrano najodpowiedniejszy dla warunków spalania fluidalnego zerowymiarowy model.

Aby lepiej zrozumieć procesy spalania i zgazowania pojedynczej cząstki koksiku, utworzono dwuwymiarowy model spalania, w warunkach nieustalonych, sześciomilimetrowej cząstki koksiku, pozwalający na odzwierciedlenie części badań eksperymentalnych przeprowadzonych za pomocą GTB. Z obliczeń uzyskano zależne od czasu profile prędkości, temperatury, koncentracji poszczególnych składników gazowych oraz zmiany morfologii cząstki koksiku. Z porównania wyników otrzymanych z modelu dwuwymiarowego, a także z badań eksperymentalnych uzyskano generalnie satysfakcjonującą zgodność w odniesieniu do ubytku masy cząstki oraz temperatury jej powierzchni.

Głównym osiągnięciem niniejszej pracy jest utworzenie pewnej metodologii postępowania umożliwiającej obliczanie szybkości konwersji pojedynczej, kilkumilimetrowej cząstki koksiku. W pierwszym etapie przeprowadzane są pomiary szybkości konwersji koksiku w TGA, w warunkach umożliwiających zminimalizowanie oddziaływania, z wyjątkiem szybkości reakcji, innych czynników wpływających na konwersję paliwa. W kolejnym etapie wyznaczana jest morfologia cząstek paliwa używanego w badaniach. Na podstawie zgromadzonych informacji możliwe jest utworzenie modeli zerowmiarowych lub wielowymiarowych w zależności od aktualnej potrzeby.

Zusammenfassung

In der vorliegenden Arbeit werden die Phänomene während der Verbrennung von Kokspartikeln umfangreich dargestellt, insbesondere in der Wirbelschichtfeuerung. Durch die vielen Vorteile der Wirbelschichtfeuerung bedarf es der weitergehenden Optimierung dieser Feuerungsart. Die größten Energieverluste entstehen durch unverbrannten Kohlenstoff, der sowohl in der Flugasche als auch in der Schlacke zu finden ist. Um diese Verluste zu minimieren, muss die Durchmischung von Brennstoff und Luft verbessert sowie die Verweilzeit der Partikel in der Hochtemperaturzone vergrößert werden.

Heutzutage wird häufig die numerische Strömungssimulation (CFD) zur Optimierung von Ofenprozessen benutzt. Um die Vorteile dieses Werkzeuges nutzen zu können, muss ein mathematisches Modell des Kessels erstellt werden. Die Brennstoffumsatzrate bei unterschiedlichen Betriebsbedingungen ist hierbei einer der wichtigsten Modellparameter, der Einfluss hat auf die Wärmeströme, die Temperatur, das Strömungsfeld und weitere Parameter, welche ausschlaggebend für den Optimierungsprozess sind. Deshalb ist eine zuverlässige Information der Partikel-Verbrennungsrate essentiell.

Die Reaktionsraten einzelner Kohlepartikel werden in CFD-Modellen häufig mittels einfacher 0D-Verbrennungsmodelle implementiert. Die größte Schwierigkeit bei der Verwendung solcher Modelle ist die zuverlässige Bestimmung der kinetischen Konstanten für die Verbrennungs- und Vergasungsprozesse. Zusätzlich muss die Kohle- / Koksmorphologie bestimmt werden, welche die Verbrennungsraten erheblich beeinflussen kann.

Die Arbeit beschreibt die notwendigen Schritte zur Bestimmung der Verbrennungsrate von einzelnen Kohlepartikeln aus der Grundlagenforschung. Die thermogravimetrische Analyse (TGA) stellt dabei die erste grundlegende Untersuchungsmethode dar, die Informationen über die Umsatzrate als Funktion der Temperatur bei bekannter Atmosphäre liefert. Die zweite Untersuchungsmethode ist die Quecksilberporosimetrie. Hieraus wurden die Brennstoffporosität, die spezifische Partikeloberfläche und die spezifische Partikeldichte bestimmt. Aus den Ergebnissen beider Untersuchungen wurden Arrhenius-Koeffizienten, die die Reaktionsrate von Kohle in einer Sauerstoff- bzw. einer Kohlenstoffdioxid-Atmosphäre beschreiben, bestimmt.

Aus den Ergebnissen der Thermogravimetrie und der Quecksilberporosimetrie wurden verschiedene 0D-Modelle entwickelt, die innerhalb von CFD-Kesselmodellen zum Einsatz kommen können. Alle Modelle wurden experimentell mit Hilfe eines neu entwickelten Prüfstandes (Grain Thermo-Balance, kurz: GTB) validiert. Der GTB-Prüfstand erlaubt die Aufzeichnung des Masseverlustes der Partikel sowie die Partikel-Oberflächentemperatur während der Verbrennung. Die Versuchsbedingungen im Prüfstand wurden derart gewählt, dass sie möglichst

den realen Bedingungen im Wirbelschicht-Kessel entsprechen. Aus dem Vergleich der unterschiedlichen 0D-Modelle mit den experimentellen Daten wurde das für die Wirbelschicht-Verbrennung am besten geeignete Modell gewählt.

Um das Verbrennungsverhalten eines einzelnen Koks-Partikel im Millimeter-Bereich besser zu verstehen, wurde ein instationäres 2D-Modell eines im Durchmesser 6 *mm* großen Koks-Partikels erarbeitet. Dieses Modell wurde benutzt, um die Ergebnisse aus dem GTB-Prüfstand zu simulieren. Das Temperaturfeld, die Reaktandenkonzentration und die Partikelmorphologie wurden als Funktion des Ausbrandes zeitaufgelöst mit den Messungen verglichen. Die Über-einstimmung zwischen der berechneten und experimentell bestimmten Massenabnahme des Partikels sowie der Oberflächentemperatur war insgesamt gut.

Das wesentliche Ergebnis dieser Arbeit ist die Entwicklung einer Methodik zur Berechnung von Umsatzraten von Kokspartikeln in der Größenordnung von wenigen Millimetern. Die Methodik beginnt mit der TGA-Messung von kinetisch kontrollierten Umsatzraten, der sich die Bestimmung der Partikelmorphologie anschließt. Anhand der so gewonnenen Informationen können mehrdimensionale Modelle entwickelt werden.

Abbreviations

CFD	**C**omputational **F**luid and **D**ynamics
FB	**F**luidized **B**ed
FBB	**F**luidized **B**ed **B**oiler
GB	**G**rate **B**oiler
GTB	**G**rain **T**hermo-**B**alance
IGCC	**I**ntegrated **G**asification **C**ombined **C**ycle
IPCC	**I**ntergovernmental **P**anel on **C**limate **C**hange
IR	**I**nfra**R**ed
OECD	**O**rganization for **E**conomic **C**o-operation and **D**evelopment
PFB	**P**ulverized **F**uel **B**oiler
SCM	**S**hrinking **C**ore **M**odel
SChPCM	**S**ingle **Ch**ar **P**article **C**ombustion **M**odel
SCPCM	**S**ingle **C**oal **P**article **C**ombustion **M**odel
SPM	**S**hrinking **P**article **M**odel
TGA	**T**hermo**G**ravimetric **A**nalysis/**A**nalyzer
UN	**U**nited **N**ations

Physical Constants

Stefan-Boltzmann constant	σ	=	$5.67 \cdot 10^{-8} W/(m^2 \cdot K^4)$
Universal gas constant	R	=	$8.314\ kJ/(kmol \cdot K)$

Symbols

A	Ash content in coal	$\%$
A_{int}	Pre-exponential factor for intrinsic kinetics	m/s
c_{ash}	Ash specific heat capacity	$kJ/(kg \cdot K)$
c_C	Carbon specific heat capacity	$kJ/(kg \cdot K)$
c_{char}	Specific heat capacity of solid material in char	$kJ/(kg \cdot K)$
C_{CO2}	Molar concentration of carbon dioxide	$kmolCO_2/m_g^3$
C_j	The j^{th} species molar concentration	$kmol\ j/m^3$
C_{O2}	Molar concentration of oxygen	$kmolO_2/m_g^3$
$c_{p\ air}(T_p)$	Air specific heat capacity at constant pressure, at T_p	$kJ/(kg \cdot K)$
c_p	Specific heat capacity	$kJ/(kg \cdot K)$
$c_{p\ i}$	Specific heat capacity of the i^{th} species	$J/(kg\ i \cdot K)$
c_r	Char conversion rate	kg/s
$c_{r\ av}$	Average char conversion rate	mg/s
$c_{r\ B}$	Carbon conversion rate caused by reaction with CO_2	$kg\ C/(m^3 \cdot s)$
$c_{r\ oxy}$	Carbon conversion rate caused by reaction with O_2	$kg\ C/(m^3 \cdot s)$
d_{core}	Diameter of unreacted particle core	m
D_{eff}	Effective diffusivity	m^2/s
$D_{eff\ i}$	Effective diffusivity of the i^{th} species	m^2/s
D_g	Gas diffusivity	m^2/s
$D_{g\ b}$	Gas diffusivity at bulk temperature	m^2/s
D_{i-j}	Binary pair mass diffusion coefficient of the i^{th} species in the j^{th} species	m^2/s
D_k	Knudsen diffusivity	m^2/s
$d_{pore\ av}$	Average pore diameter at time τ	m
$d_{pore\ av0}$	Initial average pore diameter	m

d_p	Particle diameter	m
$d_{p\ e}$	Equivalent spherical particle diameter	mm
d_{tbead}	Diameter of thermocouple bead	m
$E_{a\ int}$	Activation energy	$kJ/kmol$
$\vec{F}$	Vector of external body forces	N/m^3
g_{ash}	Ash mass fraction	$kg\ ash/kg\ char$
g_C	Carbon mass fraction	$kg\ C/kg\ char$
g_i	Mass fraction of the ith species	$kg\ i/kg$
h_{CO2}^{Tp}	Specific enthalpy of carbon dioxide at T_p	kJ/kg
$h_{CO2}^{298.15}$	Specific enthalpy of carbon dioxide at 298.15 K	kJ/kg
h_{CO}^{Tp}	Specific enthalpy of carbon monoxide at T_p	kJ/kg
$h_{CO}^{298.15}$	Specific enthalpy of carbon monoxide at 298.15 K	kJ/kg
h_g	Specific gas enthalpy	J/kg
h_i	Specific enthalpy of the ith species	$kJ/kg\ i$
h_{O2}^{Tp}	Specific enthalpy of oxygen at T_p	kJ/kg
$h_{O2}^{298.15}$	Specific enthalpy of oxygen at 298.15 K	kJ/kg
Δh_r	Specific reaction enthalpy of carbon oxidation	$kJ/kg\ C$
$\Delta h_r(B)$	Specific enthalpy of Boudouard reaction	$kJ/kg\ C$
$\Delta h_r(CO)$	Specific reaction enthalpy of carbon oxidation to CO	$kJ/kg\ C$
$\Delta h_r(CO_2)$	Specific reaction enthalpy of carbon oxidation to CO_2	$kJ/kg\ C$
$h_{ref\ i}^0$	The i^{th} species specific enthalpy of formation at reference temperature (T_{ref})	$J/kg\ i$
h_s	Specific solids enthalpy	J/kg
k_b	Backward reaction rate constants	$\frac{kmol\ i}{kmol\ CO_2 \cdot s}$
k_f	Forward reaction rate constants	$\frac{kmol\ i \cdot m^{0.75}}{kmol\ CO \cdot kmol\ O_2^{0.25} \cdot s}$
k_{int}	Intrinsic kinetics constant	m/s
L_V	Volumetric pore length	m/m^3
m	Sample mass at time τ	mg
M	Moisture content in coal	$\%$
m_0	Sample mass at the time of O_2/CO_2 flow initialization	mg
m_{ash}	Mass of ash at time τ	kg
m_C	Mass of carbon in char at time τ	mg
m_c	Mass of individual cell τ	kg

M_C	Molar mass of carbon	$kgC/kmolC$
M_{CO}	Molar mass of carbon monoxide	$kgCO/kmolCO$
M_{CO2}	Molar mass of carbon dioxide	$kgCO_2/kmolCO_2$
m_{C0}	Initial mass of carbon in char	mg or g
m_{end}	Sample mass at the end of experiment	mg
$m_{i\ S}$	Mass flux of the ith species	$kg\ i/(m^2 \cdot s)$
M_{N2}	Molar mass of nitrogen	$kgN_2/kmolN_2$
M_{O2}	Molar mass of oxygen	$kgO_2/kmolO_2$
p	Absolute pressure	Pa
R_i	Net source of the ith species due to homogenous reactions	$kg\ i/(m_g^3 \cdot s)$
$r_{i,l}$	Arrhenius molar rate of creation of the	
	in the l^{th} reaction	$kmol\ i/(m^3 \cdot s)$
S_C	Solid mass source term	$kg\ C/(m^3 \cdot s)$
S_e	Heterogeneous reaction enthalpy source term	W/m^3
S_{er}	Radiation source term	W/m^3
S_{ext}	External particle surface	m^2
S_g	Gas mass source term	$kg/(m^3 \cdot s)$
$S_{g\ i}$	Mass source term of the ith species	$kg\ i/(m^3 \cdot s)$
S_{he}	Homogenous reaction enthalpy source term	W/m^3
S_m	Char specific internal surface area at time τ	m^2/g
S_{m0}	Initial char specific internal surface area	m^2/g
S_{pipe}	Surface of the inner surface of steel pipe	m^2
S_{tbead}	Surface of the thermocouple bead	m^2
S_{inner}	Outlet area of ceramic pipe	m^2
S_V	Char volumetric internal surface area at time τ	m^2/m^3
S_{V0}	Initial char volumetric internal surface area at $\tau = 0$	m^2/m^3
T_A	Activation temperature	K
T_b	Gas temperature at bulk conditions	K
T_p	Particle temperature	K
T_{rot}	Scaling temperature of rotameter	K
T_{tbead}	Thermocouple bead temperature	K
T_{wall}	Pipe internal surface temperature	K
V	Volatiles content in coal	%

$\dot{V}_b$	Volumetric flow rate at bulk conditions	m^3/s
V_c	Volume of individual cell	m^3
V_{core}	Unreacted core volume of char particle	m^3
V_p	Particle volume	m^3
V_{pore}	Total intrusion volume of mercury per gram of char	m^3/g
$\dot{V}_{rot}$	Volumetric flow rate at scaling conditions of rotameter	m^3/s
V_{ring}	Volume of the Interior-3	m^3
V_{sample}	Sample volume	m^3
w	Average velocity from outflow of the ceramic pipe	m/s
$\vec{w}$	Velocity vector	m/s
X	Char burnout	–
z'_j	mole fraction of the j^{th} species in the gas mixture evaluated on the i^{th} species free basis	–
z_{N2}	Molar content of N_2 in the gas mixture	–
z_{O2}	Molar content of O_2 in the gas mixture	–
DTG	Normalized sample mass loss rate	$1/s$
HHV	Higher heating value of coal	kJ/kg
LHV	Lower heating value of coal	kJ/kg
TG	Normalized sample mass	–
c	carbon mass fraction in coal	%
h	hydrogen mass fraction in coal	%
s	sulfur mass fraction in coal	%
n	nitrogen mass fraction in coal	%
o	oxygen mass fraction in coal	%
`Bi`	Biot number	–
`Nu`	Nusselt number	–
`Re`	Reynolds number	–
`Pr`	Prandtl number	–
`Sc`	Schmidt number	–
`Sh`	Sherwood number	–

α	Convective heat transfer coefficient	$W/(m^2 \cdot K)$
β_{eff}	Effective mass transfer coefficient of O_2	m/s
β_{eff2}	Effective mass transfer coefficient of O_2 used in SCM	m/s
δ_{m-mod}	Relative difference of average conversion rates	$\%$
ϵ	Char porosity at time τ	m_g^3/m^3
ϵ_0	Initial char porosity	m_g^3/m^3
ϵ_{ash}	Final porosity of external ash layer	$m^3\ gas/m^3$
ϵ_{aver}	Mutual emissivity of the thermocouple bead-wall arrangement	–
ϵ_p	Emissivity of the char particle surface	–
ϵ_{pipe}	Emissivity of the inner surface of steel pipe	–
ϵ_{p-pw}	Mutual emissivity of the char particle-wall arrangement	–
ϵ_{tbead}	Emissivity of the thermocouple bead	–
η	Effectiveness factor	–
η'_j	The jth species rate exponent for reactant	–
μ_b	Gas dynamic viscosity at bulk temperature	$Pa \cdot s$
μ_{tbead}	Gas dynamic viscosity at thermocouple bead temperature	$Pa \cdot s$
ν''_i and ν'_i	The ith species stoichiometric coefficient for product and substrate	–
ν''_j	The jth species stoichiometric coefficient for product	–
λ_b	Gas thermal conductivity at bulk temperature	$W/(m \cdot K)$
λ_{eff}	Effective thermal conductivity of porous medium	$W/(m \cdot K)$
λ_g	Gas thermal conductivity at temperature of gas	$W/(m \cdot K)$
λ_r	Effective thermal conductivity due to radiative heat transfer	$W/(m \cdot K)$
λ_s	Solids thermal conductivity	$W/(m \cdot K)$
γ	Stoichiometric coefficient of carbon/O_2 global reaction	$kmolO_2/kmolC$
γ_{CO2}	Stoichiometric coefficient of carbon/CO_2 reaction	$kmolCO_2/kmolC$
γ_{surf}	Surface tension of the liquid	N/m
ρ_{app}	Apparent char density at τ	kg/m^3
ρ_{app0}	Initial apparent char density at $\tau = 0s$	kg/m^3
Φ	Angle of liquid contact with solid	deg
ψ	Pore structural parameter	–
$\rho_{air}(T_p, p)$	Density of air calculated at $p = 1\ bar$ and T_p	kg/m^3

ρ_g	Density of gas at bulk temperature and standard pressure	kg/m^3
ρ_{true}	True char density	kg/m^3_{solid}
τ	Time	s
$\Delta\tau$	Time step	s
τ_{pore}	pore tortuosity	kg/m^3
$\bar{\bar{\tau}}$	stress tensor	N/m^2

Subscripts

0	Initial
b	Bulk
g	Gas
i	The i^th species
j	The j^th species
p	Particle

Superscripts

a	Analytical conditions
daf	Dry ash-free basis
exp	Experimental
mod	Modeling

Chapter 1

Introduction

1.1 Coal as the main source of energy

Primary energy demand for the World reached 19.1 *Gtce*[1] in 2012 [1]. Energy needs are covered by various primary energy sources, from which coal is one of the most important. Figure 1.1 shows that the share of coal in the primary energy mix is 29% [1]. Oil and gas provide 32% and 21% of the demand, respectively. Renewable energy sources are responsible for covering 13% of the World's primary energy demand. For Germany and Poland, the primary energy demand is 469.4 *Mtce* and 140.4 *Mtce*, respectively. This means that primary energy consumption per capita is 5.83 *tce* in case of Germany and 3.65 *tce* in case of Poland [1]. In Germany coal covered in 2012 circa 24.8% of the energy demand, oil 32.9%, gas 21.5%, renewables 11.6% and nuclear energy 7.9% [1]. Poland in contrast had in 2012 the largest share of coal (55%) in the primary energy mix, while oil, gas and renewables provide 26%, 15% and 4% share, respectively [2].

The electricity production in the World (total production of 22 500 TWh, which corresponds to 2.76 *Gtce*) is dominated by coal, as shown in Figure 1.2; in 2012 the share was 41%, which means that 9225 TWh was converted from coal [1]. Furthermore, the share of electricity production from coal is growing continuously since 1990 [3]. This is partially associated with reserves and resources of coal, which are much larger than the other non-renewable energy sources [1]. Furthermore, coal prices are relatively low if compared to oil and gas, which allows for electricity generation with competitive prices. This is one of the reason why Poland and Germany still relay on coal as a reliable energy source for electricity generation. Germany produced 628.7 TWh of electricity in 2012, from which 44.2% was converted from coal, 22.6% from renewable energy sources, 15.8% from nuclear, 12.0% from natural gas and the rest from other sources [1]. Poland in contrary produced in 2011 163.2 TWh of electric energy, from

[1] $\approx$ 560 EJ/a or $\approx$ 155.5 PWh/a; tce - tonne of coal equivalent

which 88% was produced from coal, 3% from natural gas, 2% from oil and 7% from renewables [4].

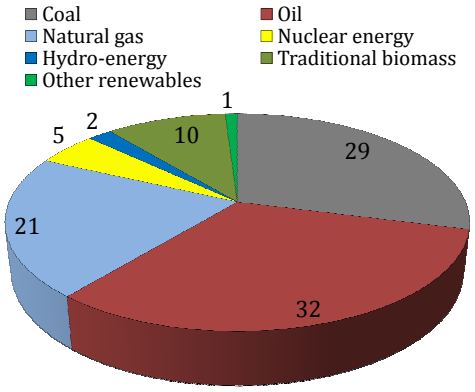

FIGURE 1.1: World's primary energy demand share by source in 2012 [1] (19.1 *Gtce* in total); Values in %

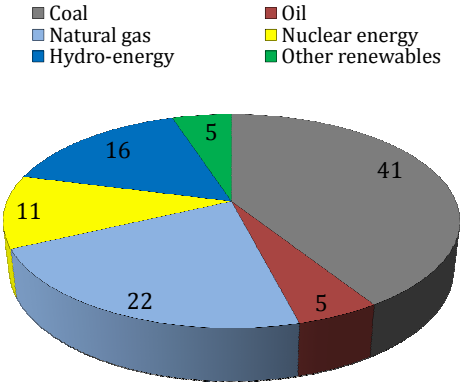

FIGURE 1.2: World's electricity generation share by source in 2012 [1] (2.76 *Gtce* in total); Values in %

The share of coal reserves in entire World's non-renewable energy deposit was estimated in 2012 to be more than 50% [5]. When World's resources of non-renewable energy sources are considered, the energy stored in coal constitute up to 90% of total non-renewable energy deposit [5]. Coal resources are deposits of coal in the Earth's crust, which are in the form and in the quantity that the perspective exists for their eventual future economic extraction. Reserves of coal are the part of resources, which are from economical, social and environmental reasons feasible to be extracted with the present technology. For Europe the coal share in non-renewable energy deposit, in 2011 was 88%, when reserves were considered and almost 95%, when resources were taken into account [1]. World's coal resources were estimated in 2012 to be almost 16 195 billions tonnes of coal equivalent, while reserves were 769 billions tonnes of hard coal and circa 283 billions tonnes of lignite [5].

The World's coal production has risen during past ten years and in 2012 it reached 7.941 *Gt* [5]. Production of hard coal accounted for 86% of this amount [5]. In the OECD

countries (OECD - Organization for Economic Co-operation and Development), the coal share in energy mix is decreasing [6], while in the non-OECD countries the intensive growth of energy demand is in large extend covered by coal. In contrary to oil or natural gas, coal resources are widely spread in the World. Therefore, coal market is much more predictable, because politically-stable countries are major producers, as shown in Figures 1.3 and 1.4. The biggest producer of hard coal in 2012 was China, which accounts for more than 50% of World's production [5]. The second biggest is the USA and the third is India, which together produced 1408 *Mt* of hard coal (Figure 1.3) [5]. In case of lignite (Figure 1.4), the biggest production of 185.4 *Mt* was in 2012 in Germany [5]. China was the second biggest producer, while Russia had the third biggest lignite production of 77.9 *Mt* (in case of Russia and Ukraine, lignite and sub-bituminous coals are included in the statistics of lignite) [5].

The USA and China have the largest reserves of hard coal in the World (together around 404 *Gt*) (Figure 1.3) [5]. Together they account for more than 50% of World's documented and possible to extract, with the present technology, resources. In case of lignite, the largest reserves are found in Russia, Australia and Germany [5].

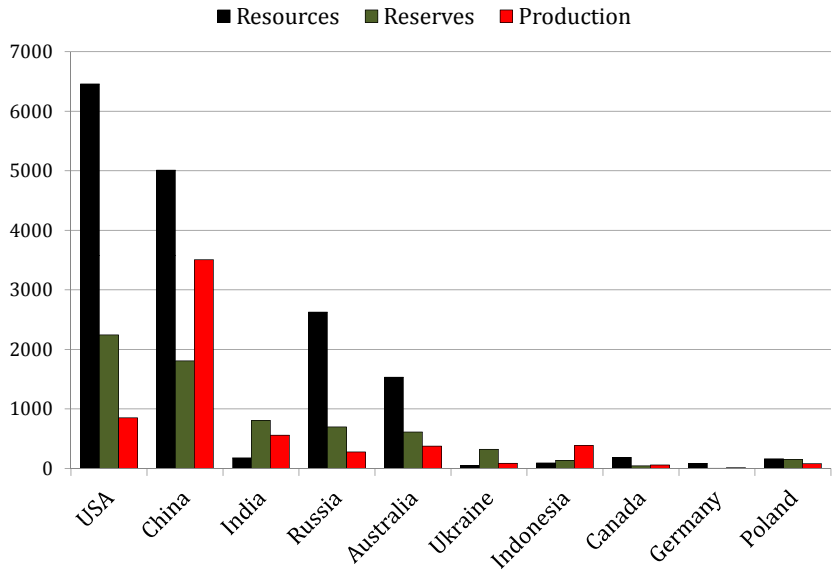

FIGURE 1.3: Hard coal resources, reserves and production for ten countries [5]; Data for year 2012; Resources in *Gt*, reserves in $Gt \cdot 10$ and production is shown in *Mt*

The European Union's hard coal and lignite reserves are estimated to be sufficient for the next 130 years [7]. Nevertheless, free market economy, environmental and social issues are responsible for closing of coal mines, which are not profitable or are too harmful for the environment. The gradual closing of hard coal mines is observed for example in Germany. German politicians, despite the fact that Germany in 2012 was already the biggest hard coal importer in the European Union (circa 44.9 *Mt*) [1], are determined to close all still running hard coal mines [8]. Total import of coal into the EU (European Union) has already reached

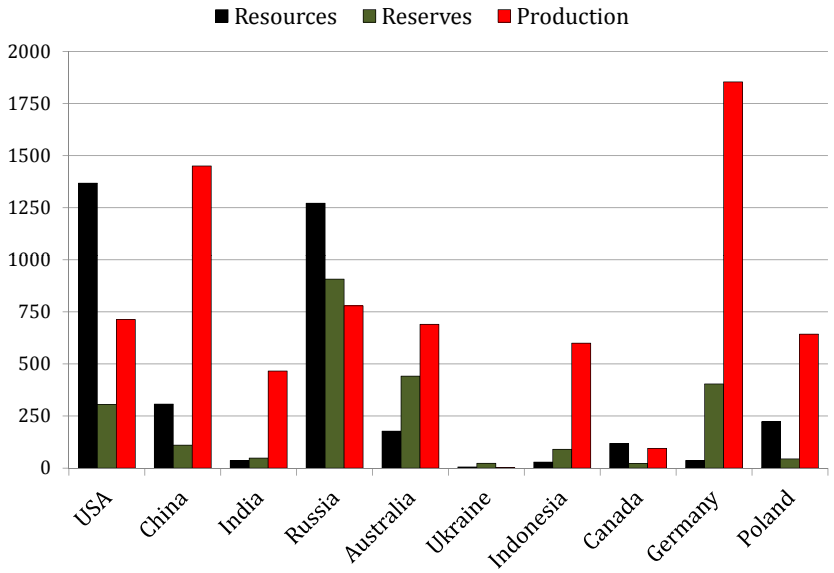

FIGURE 1.4: Lignite resources, reserves and production for ten countries [5]; Data for year 2012; Resources in Gt, reserves in $Gt \cdot 10$ and production is shown in $Mt \cdot 10$

213 Mt in 2012 [1]. It is foreseen that this import will grow in the next twenty years [1]. This increase is partially associated with high prices of natural gas and with German plans to withdraw from nuclear power. On the other hand lignite-fired power plants are still considered by European governments as important for many years ahead. In contrary to hard coal, a free market for lignite almost does not exist, what is due to low energy density of this fuel. This causes that its transport over long distances is not economically justified [1]. However, because opencast mining of this fuel makes it the cheapest among all energy sources, new power plants are being built in Europe [9].

Despite the German's energy policy, outlined by the Federal Ministry of Economics and Technology, to promote renewable energy sources [8], Germany still generates 44.2% (data for 2012) of its electricity needs from hard coal and lignite [1]. This is because electricity production from fossil fuels can provide a reliable supply of power when is needed, also in conditions, which for photovoltaic panels and wind power are inappropriate. Therefore, even if the share of renewable energy sources in German "energy mix" increases considerably [10], the gas- and coal-fired power plants are needed to secure reliability of the electricity supply [8].

Poland, in contrary to many EU countries, coverts 88% of electricity from coal, which makes this country to have the second largest coal share in electricity production after Republic of South Africa [11]. From the viewpoint of electricity production, the most important are resources of Polish hard coal type 31-33[2] (thermal coals). Estimated coal resources allow for covering the Polish needs for the next 450 years (data for 2011), however, reserves of 31-33 coal type, which are profitable and technologically available, are projected to last for the next

[2]Polish classification for coals

30 years [11]. The future situation of Polish hard coal mining will depend on both World's coal prices and the new mining technologies. When the hard coal prices fall, mines in Poland are likely to be closed, unless Polish government institutes subsidies. Nevertheless, production of electricity from coal will remain competitive, unless too high taxes for CO_2 emission allowances are introduced. According to the Polish Ministry of Administration and Digitization [12], the share of coal in Polish energy mix will decrease till the year 2030. However, both hard coal and lignite will still be dominant and should guarantee the energy independence of Poland. In order to secure coal supply, the preparation and opening of new coal deposits are foreseen by Polish Ministry of Economy. These predictions are underlined in the Polish energy policy document, accepted by the Polish government in 2009 [13].

1.2 Available technologies of coal utilization for heat and electricity production

Coal combustion is recently been carried out in three types of boilers: pulverized fuel boilers (PFBs), fluidized bed boilers (FBBs) and grate boilers (GBs). The comparison of the most important parameters concerning combustion in these boilers is shown in Table 1.1.

Table 1.1: Boiler technolgy comparison

Parameter	**PFB**	**FBB**	**GB**
Temperature, °C	1320 – 1700 [14]	850 [15]	circa 1300 [16]
Particle size, *mm*	< 0.1 [17]	1 – 10 [18]	6 – 32 [17]
Heating rate, K/s	10^4 – 10^6 [19]	10^3 – 10^4 [19]	10^0 – 10^2 [19]
Gas velocity through combustion zone, m/s	15 – 30 [17]	0.5 – 6 [17]	1 – 3 [17]
Single coal particle residence time, s	2 – 5 [14]	30 – 600 [17]	> 1000 [19]
Combustion efficiency, %	circa 99.5 [17]	90 – 99.5 [17]	circa 87 [17]
Air excess ratio, $kmol\ air/kmol\ air_{stoich}$	1.15 – 1.3 [17]	1.1 – 1.25 [17]	circa 1.2 – 1.3 [17]

Pulverized fuel boiler technology is the most commonly used. Coal has to be milled to the size of hundreds of micrometers (see Table 1.1). Such small particles are fed into boiler using special burners, which are located either in corners of the combustion chamber or on the boiler walls. In corner-fired boilers the flow direction is turned slightly from the combustion chamber center allowing vortex formation, which extends the particle residence time in high temperature zone and improves the mixing of fuel with combustion air. In wall-fired boilers, burners are located on the opposite walls of the boiler. Pulverized fuel boilers are usually used in large power plants up to 1100 MW_e [3]. Considerably large amounts of nitrogen oxides are formed in PFBs, which have to be removed from the flue gases, in order to meet emission requirements.

Also flue gases have to be treated to remove sulfur oxides. Usually wet scrubbing is used for flue gas desulfurization. To remove ash from flue gases the electrostatic precipitators are used.

The second type of boilers are FBBs, which are generally lower power units than PFBs. The World's largest FBB unit (circulating fluidized bed boiler) belongs to Łagisza power plant (Poland) and has the nominal power output of 460 MW_e [20]. Here the particles of solid fuel are much larger (a few millimeters). Apart from fuel, also bed material is added into the combustion chamber. The bed material is usually limestone, which allows for in-furnace desulfurization. Because temperatures in FBB are relatively low (see Table 1.1), NO_x emissions are usually low enough to meet environment protection regulations. Similarly to PFBs, an electrostatic precipitator is often used for ash removal. This type of boilers is used in facilities, which generate electricity alone, supply heat or co-generate heat and electricity. Further description of this technology is given in Section 1.2.1.

In contrary, grate boilers (GB) are small units (15 kW_{th} – 30 MW_{th} [21]), which are mostly used for heat generation. Coal, used in these boilers, have granulation of a few centimeters, as indicated in Table 1.1. Combustion takes place on the grate and combustion air is supplied beneath the grate. Because of the size, these boilers do not have electrostatic precipitators, but rather cyclonic separators or fabric filters for dust removal. Desulfurization and denitrification of flue gases are rather rare.

Another possible technology for conversion of coal chemical energy into electricity is the Integrated Gasification Combined Cycle (IGCC). Here the conversion progresses in two stages. The first stage is coal gasification. In the second stage, produced gas is combusted in a gas turbine, which drives the electricity generator. This technology is characterized by high net efficiency, due to two-staged electricity production: the first in a gas turbine, the second in the conventional Clausius-Rankine cycle (using enthalpy of gas turbine exhaust gases), and also by low emissions [3]. Nevertheless, this technology has the highest investment and operating costs among the above presented technologies [3].

1.2.1 Closer look at fluidized bed boiler technology

All above presented boiler technologies are continuously being optimized to improve boiler efficiency and to meet new emissions regulations. Because combustion in fluidized bed is not so well understood as pulverized fuel combustion, the World's research is directed to a large extend toward FBBs technology. This technology has advantages, since is much more tolerant to the quality of supplied fuel. Organic wastes, biomass and low-quality coals are examples of fuels which could be burned in FBBs. Besides the fuel tolerance, these boilers have many other advantages, the most important being:

- Intensive heat transfer, which equalizes the temperature in the combustion chamber and allows for compact design of FBB. Uniform and relatively low temperature (see Table 1.1) prevents thermal nitrogen oxides formation and reduces thermal stresses of material in the boiler;
- Desulfurization is often performed in the combustion chamber by limestone, which decomposes into calcium oxide, which reacts then with SO_2. Calcium sulfate is produced from this reaction, which is a stable and environmentally-inert compound. Therefore, it is not necessary to built desulfurization facility next to FBB, so that the investment cost of entire power plant is reduced;
- In case of coal combustion, because of temperatures lower than ash softening point, ashes are in form of powder, which makes soot blowing relatively non-problematic.

There are two types of FBBs: Bubbling FBBs and Circulating FBBs. Bubbling FBBs are smaller units, which in comparison to circulating FBBs have worse substrates mixing conditions, thus their efficiency is lower. Therefore, studies are predominantly focused on Circulating FB technology. In the Circulating FBBs the fuel, limestone and part of air are supplied into the combustion chamber. The fluidization air (2) (see Figure 1.5) causes that coal and limestone particles pass into fluidized state, which means that particles behave like boiling liquid. Gas velocity is large enough to carry away the smallest char and bed material particles, which are subsequently separated from gases using cyclonic separator (6). Unburned char and bed material is then recirculated through loop seal (7) to the combustion chamber (5). The flue gases elutriate the smallest solid particles and carry them to the part of furnace, where heat exchangers (i.e. economizer and superheater) are located (8). After cooling down, the flue gases undergo the process of ash separation in electrostatic precipitator.

1.3 Environmental and political issues concerning coal usage in power plants

During coal combustion, substantial amounts of pollutants are produced. The most important hazardous gases, besides sulfur dioxides, are nitrogen oxides. Their formation takes place in three possible paths: thermal, prompt and fuel. Fuel NO_x are associated with nitrogen, which is bound with hydrocarbon material in the fuel, while in prompt mechanism reactions between fuel and nitrogen from air cause nitrogen oxides production. Thermal path of NO_x formation is highly dependent on temperature present in the boiler. This mechanism (Zeldovich mechanism) becomes important when temperature exceeds 1673 K [23]. The third important pollutant, produced during coal combustion, is fly ash. The most hazardous are the smallest particles $< 2.5\ \mu m$, which can be inhaled into lungs and then transported with blood favoring

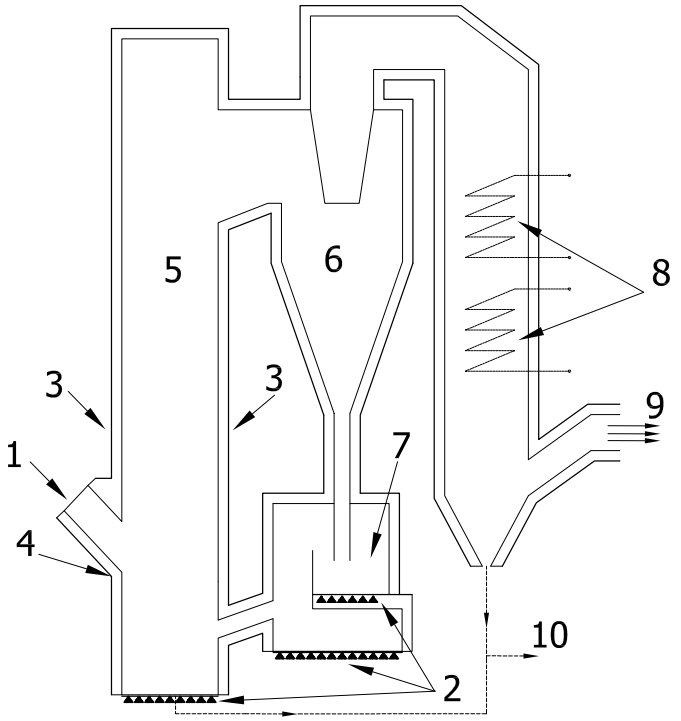

FIGURE 1.5: Scheme of Circulating Fluidized Bed Boiler [15, 22]; 1 - Fuel feeding; 2 - Fluidization air; 3 - Secondary air; 4 - Limestone/bed material feeding; 5 - Combustion chamber; 6 - Hot cyclone; 7 - Loop seal; 8 - Heat exchangers; 9 - Exhaust gases; 10 - Ash removal

diseases. Additionally, many toxic substances can be absorbed on the ash surface (for instance: arsenic, cadmium, mercury, uranium, lead and polycyclic aromatic hydrocarbons), causing even bigger damage to the human body. From these substances, mercury is one of the most dangerous and its content in Polish hard coals is in range of $50 - 350$ ppb (ppb - parts per billion) [24, 25].

Nowadays, carbon dioxide is also considered as pollutant by some politicians and environmentalists and CO_2 is blamed for causing global warming. The IPCC (Intergovernmental Panel on Climate Change) next to the UN suggested that observed increase of CO_2 content in the troposphere and of World's average tropospheric air temperature are caused by human activities [26]. This was one of the reasons for formulating the Kyoto protocol, which was signed by many countries and which committed contributed parties to decrease emissions of greenhouse gases. Nowadays new climate policies are being formulated. A new agreement, which is foreseen to be accomplished in 2015, may remain hardly acceptable by many countries, since the climate policies are in conflict with economic growth. Especially at present time, the climate protection policies are in risk, due to economic crisis, which started in 2007/2008 and many countries still experience recession [27]. Recession is also present in some European Union's countries. Despite this fact, the European Union does not strengthen the economic growth by reducing high taxes assessed on energy carriers. Instead, the EU wants to be the World's leader of a new strict climate policy. Electricity cost in the EU is 70% higher than in the USA and

natural gas prices are almost three times higher (Germany has been taken here as a reference country; data for 2012) [28, 29]. Low energy prices are the base of strong economy when labor costs are at the fixed level. When the electricity and fuel prices become too high, many factories are being closed and moved to, for instance, the Far East. This is one of the reasons for Chinese fast economic growth, where fuel is less expensive and labor costs are low. Moving an industry into a country, where the production is cheaper, does not mean, however, that the global emissions of greenhouse gases are reduced. The global CO_2 emission has risen by 50% since 1990 [7]. This means that even if carbon dioxide emissions in Europe and other countries involved in Kyoto protocol are reduced, they effect on the World's CO_2 emission is marginal. If CO_2 emission are calculated on the consumption basis, the 'carbon footprint' of the European Union increases significantly [7]. Summing up, the greenhouse gases reduction has no sense if the emission limits are being observed within the EU only.

Supplying heat and electricity to the market is mainly done by burning of fossil fuels. However, each fossil fuel causes carbon dioxide formation, which is not possible to be avoided, since they contain carbon. Moreover, carbon dioxide is highly required product, since during its formation the biggest possible amount of heat is released. Because the EU policy influences the research directions, thus they are targeted toward non-carbon technologies development. Since the renewable energy sources cannot meet the demand alone, thus studies are also directed to obtain higher electricity and heat production efficiency from fossil fuels and to make the appliances less energy-consuming. These directions are reasonable in opinion of this thesis author, because higher efficiency means that less fuel is consumed to produce the same amount of energy. Due to that less pollutants are emitted and more fuel resources are preserved. Nevertheless, new policies require a carbon dioxide cut, which is considerably larger than it could be obtained through power plants efficiency increase and increase of renewable energy share in the energy mix. Therefore, a new technology is being developed for carbon capture and storage (CCS). Probably, the largest disadvantage of this technology is a significantly lower net efficiency of the power plant (a decrease up to 12% [7]) due to high energy requirements for CO_2 separation units. This causes that more fuel is needed to produce the same amount of electricity in comparison with the plant without the CCS. Not without significance is also the high cost of a carbon dioxide storage. Carbon dioxide can be stored only in special geological formations. Usually, empty natural gas fields are considered as good storage sites. Carbon dioxide injection into oil wells is considered to accelerate gas and oil exploitation. However, no absolute certainty as to the tightness of such storage sites can be provided. In case of CO_2 leaks, not only the investments are wasted, but also a nearby region would have to be evacuated, since higher CO_2 content in air (several %) can be very harmful to human and environment.

Summing up, research should focus more on possibilities for boiler efficiency improvements, which will contribute to reducing the demand and usage of the coal, while reducing the negative impact of power and heat generation on the environment.

Chapter 2

Motivations, aim and scope of the work

2.1 Motivations

To reduce pollutants emissions and to increase boilers efficiency it is necessary to optimize processes occurring during coal combustion. Is it important to decrease energy losses, which are associated with incomplete fuel combustion. The largest part in these energy loses is associated with unreacted carbon, which is found in a fly ash as well as in a slag. In order to minimize these loses, better mixing of fuel with air and prolongation of the residence time of coal particles in a high temperature region, are required. Optimized distribution of fuel and air allows for decreasing air excess ratio, causing mass flux decrease of flue gases, which diminish the flue gases thermal energy losses.

Nowadays, to optimize processes in a furnace, CFD (Computational Fluid Dynamics) is often used. To take advantage of this method a mathematical model of the boiler has to be built. In such models, one of the most important input data are fuel conversion rates at various conditions. Having coal conversion rates, the energy release rates can be calculated. This information affects heat fluxes, temperature, flow field and many other variables, which are crucial for process optimization in the boiler. Therefore, delivering reliable information regarding coal particles combustion rates is essential.

In case of FB combustion particles are treated separately in the CFD model, therefore, the knowledge of single coal particle conversion rates is crucial. Large particles (a few millimeters in diameter), which are delivered to FBBs, burn differently in comparison to particles supplied to PFBs (see Table 1.1). The burnout time of such large particles reaches even 2-5 minutes [14]. Because of large particle sizes, the gradients of temperature and oxygen concentration are present inside the particle, as shown in Figure 2.1. Due to the size, combustion of larger particles is more dependent on diffusion of reactants in comparison with pulverized coal particles.

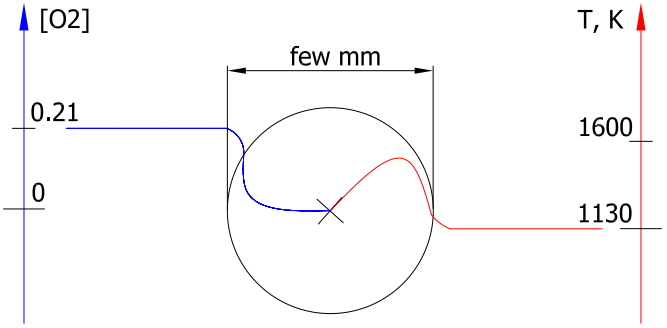

FIGURE 2.1: Schematic diagram of single larger coal particle combustion in air; Blue lines show change of molar content of oxygen, red lines temperature

The literature provides information on conversion rates of a single fuel particle of several millimeters in size. Many different approaches are used when char combustion is modeled, as reviewed by Laurendeau [30] and Smith [31]. The research, in coal combustion field, is focused mostly on char conversion, due to the fact that char combustion provides considerably larger energy portion in comparison to volatiles combustion and because heterogeneous reactions are much slower than homogenous. Therefore the combustion time is dependent, in large extent, on char burnout time. Different approaches for mathematical description of char combustion are for instance described in works of Laurendeau [30] and Smith [31]. Laurendeau [30] divided single char particle models into the classical unreacted shrinking core model and to the progressive conversion model. In the classical shrinking core model, reactions progress on the external surface of the unreacted char core. This simplification in case of slow reaction and/or high porosity is not reliable and can cause underestimation of char conversion rate. In reality, reactions progress inside the unreacted core because reacting gas can penetrate the particle [30]. Thus, the classical unreacted shrinking core model should be restricted to non-porous solids [30]. The ash layer diffusion resistance in this model can be omitted and in this case the model is called as shrinking particle model. The progressive conversion model in contrary assumes that heterogeneous reactions occur on the internal surface of the particle. Therefore the reacting gas concentration is not zero inside the particle [30]. Here the effectiveness factor (η) is introduced, which determines the percentage of entire internal surface area (available if no pore diffusion resistance exists), which is available for reactions to occur [31]. Also in progressive conversion models ash influence can be taken into consideration [30]. Most of mathematical models of char combustion threat particles as a sphere. The change of thermodynamic and physical char parameters with time are taken into account in the simplest zero-dimensional models, which are quite rarely used in comparison to one-dimensional models. One-dimensional models include also the change of these parameters (temperature, char burnout, porosity, etc.) with the particle radius. Author of this thesis have not found many models in the literature [32, 33], which allow for calculation of species concentration, temperature, burnout degree, etc. at any location

within the particle. The combustion models, which allow to do so are two-dimensional or three-dimensional. These models are capable for determination of the particle combustion asymmetry, caused by reactive gas flow.

One of the major difficulties, occurring when the combustion model is being developed is the reliable determination of kinetic constants for combustion and gasification processes. Kinetic constants are calculated from data obtained using thermogravimetric analyzers (TGA), drop tube reactors, small fluidized bed reactors and similar devices [34]. Because of low cost of a single run and its short time requirements, the most popular is the TGA. This apparatus continuously measures sample mass during its thermal treatment at required temperature. The study can be carried out in isothermal or non-isothermal modes. However, all measurement techniques and thus also the TGA has its specificity and limitations. The question arises, if the TGA can be used for combustion kinetics determination of larger char particles, which are used in FBBs. There is no obvious answer to this question since substantially different conditions are present in the TGA and in FBBs. Particles heating rates, for instance, in the TGA are around 50 K/min, while in FBBs are 1000-10000 K/s [34]. Therefore the char obtained due to devolatilization in FBBs have different reactivity to the char samples obtained by slow devolatilization in the TGA. It necessary to mention that char reactivity depends on sample chemical structure, inorganic constituents and porosity [30]. The first element is associated with concentration of carbon edges and defects, the occurrence of which enables char to react. The influence of mineral matter is usually catalytic for heterogeneous reactions. Important is also the oxygen and hydrogen content in the char; the higher the content of these elements, the more reactive is the char. The porosity is also important, because of its influence on diffusion rates [30]. Larger porosity facilitates mass transfer. Therefore it is interesting to determine the physical properties (morphology) of char, which is produced in conditions found in FBBs and in the TGA. Nevertheless, this is not the only problem when determining kinetics using the TGA. Experiments have to be carried out in conditions, in which both bulk and pore diffusion do not influence the char conversion rates. This is difficult since gas availability to the sample surface is restricted in TGA through crucible and device design. All these factors cause that the determination of fuel conversion rates using TGA is problematic and has to be carried out with special caution.

2.2 Aim and scope of the work

The aim of this study is to understand the combustion and gasification processes of a single, a few millimeters size coal/char particle for the application to fluidized bed boilers. The following investigations have been undertaken, which can be divided into the experimental part (points 1, 2 and 3) and the theoretical/modeling part (points 4 and 5).

1. In order to develop any combustion model, kinetic constants have to be determined and thermogravimetric analysis (TGA) is used to this end. To obtain correct values, proper experimental procedures have been developed, in order to eliminate diffusion influence on the char conversion. The procedures for kinetic constants acquiring for char combustion in oxygen and gasification in carbon dioxide have been developed. The kinetic constants are then used in char combustion models. Additionally, the influence of char preparation methods on the combustion rates and kinetic parameters is being studied.

2. The second experimental investigation, which is the mercury porosity analysis, has been used for determination of physical properties of char. This analysis is crucial when intrinsic kinetic parameters have to be estimated from the thermogravimetric analysis. Also values obtained by this analysis are used in the mathematical description of char combustion models. This investigation will help to answer the question regarding the influence of char preparation method on its reactivity.

3. In order to investigate the process of a single coal/char combustion the new test rig has been built. The rig allows for continuous measurement of mass loss and surface temperature of the burning particle. Experimental conditions have been chosen to reflect to some extent these, which occur during coal combustion in fluidized bed boilers.

4. In this thesis several models are created. Zero-dimensional models are being developed to be used in conjunction with CFD boiler models. The zero-dimensional shrinking core model and the shrinking particle model have been created and tested, taking various models simplification into account. Comparison of results obtained by these models with measurements, described in point 3, allows for determination of both their accuracy and applicability range.

5. A transient 2-dimensional mathematical model of single (large) char particle combustion is developed to simulate the GTB experiments (described in point 3). The model accounts for the reactant transport to the particle surface (fluid flow) as well as inside the reacting particle. Time dependent temperature field, reactant concentration field as well as particle properties (morphology) are computed and compared with the measured data. The model is used to answer the following specific questions:

   - How large are temperature and species gradients inside the particle and how these gradients influence the char conversion rates?
   - Is carbon monoxide oxidized already inside the particle or within the particle boundary layer, or far away from the particle surface?
   - To which extend the Boudouard reaction is important at conditions found in the GTB test rig?
   - What is the influence of air flow on the char burnout?

As it has been pointed out the work is related to coal combustion in fluidized bed boilers. One should however realize that mathematical modeling of fixed bed combustion and gasification requires single-particle sub-models, which are very similar to the ones developed in this thesis (see for example [35–38]).

Chapter 3

Coal characterization

3.1 General information

Experimental investigations described in this work have been performed on Polish hard coal extracted from "Janina" coal mine, which is located in Libiąż in Lesser Poland Voivodeship and lies on the Upper Silesian Coal Basin. Coal mine "Janina" belongs to Południowy Koncern Węglowy S.A. The company owner is partially the Kompania Węglowa S.A. (the largest Polish hard coal mining company) and the Tauron Polska Energia S.A. (second biggest electricity producer in Poland). Industrial reserves of this coal field are the biggest among all the running coal mines in Poland and were estimated in 2012 to amount to 357 *mln Mg* [39]. The coal production in 2012 was 2.333 *mln Mg* [39]. Despite the fact that this coal mine has been operated since the beginning of XX century, its operation is foreseen to be ongoing for next 80 - 100 years, taking actual production into account [40]. The reduction of foreseen operation time in comparison with the theoretical one, calculated from two above-mentioned factors, is a consequence of economical aspects, tectonic discontinuities in the deposit and relatively high losses of coal during mining (20-30% [41]) [40]. Nevertheless, even the 50 years period of coal production is long enough to supply a newly build power plant, of which the life time is usually 50 years. Taking into account foreseen operational time of the mine, the selected fuel is perspective.

3.2 Proximate and ultimate analysis

Used in this study fuel is a bituminous gas coal and gas-flame coal, which, in Polish classification, has no. 31 and 32 [42]. Table 3.1 shows proximate and ultimate analysis of coal "Janina". The analysis has been made by Energopomiar Sp. z o.o.

TABLE 3.1: Proximate and ultimate analysis of coal "Janina"

Parameter	**Symbol**	**Unit**	**Value**
Moisture content	M^a	%	11.0
Ash content	A^a	%	12.3
Volatiles content	V^a (V^{daf})	%	30.4 (39.7)
Higher heating value	HHV^a	kJ/kg	22 910
Lower heating value	LHV^a	kJ/kg	21 831
carbon	c^a	%	58.2
hydrogen	h^a	%	4.0
nitrogen	n^a	%	0.9
sulfur	s^a	%	1.5
oxygen	o^a	%	12.1

Chapter 4

Experimental study on single particle devolatilization and combustion

In order to compare the models outcomes (Chapters 7 and 8), an experimental stand has been built, so as to reproduce the combustion conditions occurring in fluidized bed boilers. Among parameters that are the most important to be reproduced are: temperature, gas velocity and particle size. In the preliminary experiments, conditions for final tests have been determined. The basic experiments include the following studies:

- Devolatilization of single coal particle in nitrogen;
- Single char particle combustion in air;
- Single coal particle combustion in air.

4.1 Test bench specifications

The studies on devolatilization and combustion of a single coal or a char particle have been performed in the test rig, which allows for continuous measurements of sample mass and particle surface temperature. The test rig (see Fig. 4.1), named Grain Thermo-Balance (GTB), is composed of analytical balance RADWAG AS 110/Y, electric tube furnace Czylok PRC 20HP, infrared camera (FLIR ThermaCAM SC2000), rotameter ROL 06 NR 792040, computer and a special stand, which holds the fuel particle. The scheme of the entire test rig is presented in Figure 4.1, while the photo in Figure 4.2.

The analytical balance allows for sample mass measurements with 0.1 *mg* precision. The connection to a computer and Pomiar Win software allows for mass recording during experiment. A special particle holder is placed on the analytical balance. The holder is built out

of twisted cooper wires, however, the top grip is made out of temperature resistant alloy. The infrared camera provides the particle surface temperature with the ±2% accuracy and thermal sensitivity $< 0.1°C$. The camera is able to detect the electromagnetic radiation in the range of $7.5 - 13\ \mu m$. Gas, which is provided by the gas supply system or from a gas bottle, passes through the ceramic pipe inserted in the electric tube furnace. The temperature inside the furnace ($1.4\ kW$) is regulated in the 20°C - 1200°C range.

After a particle is placed on the particle holder and the electric pipe furnace is heated up to a required temperature, a gas flow is initialized. Because the gas is flowing through the ceramic pipe inserted into the electric pipe furnace, its temperature and velocity increase. The particle is positioned in the ceramic pipe outflow, as shown in Figure 4.3. The particle is heated up by the gas and the process of devolatilization and combustion (depending on the atmosphere) is initialized. The particle mass and its surface temperature are continuously recorded.

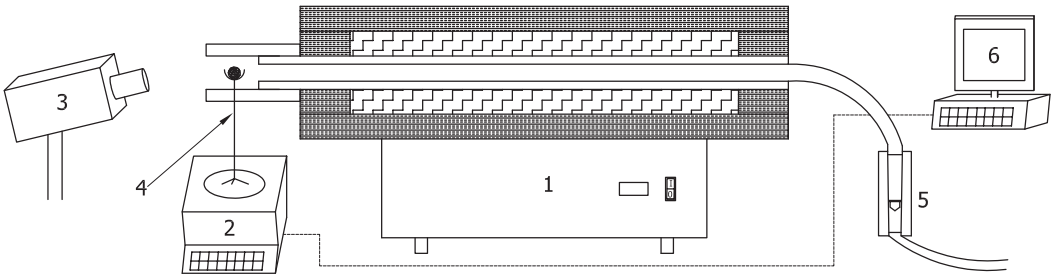

FIGURE 4.1: The scheme of the entire test rig; 1 - Electric tube furnace, 2 - Analytical balance, 3 - Infrared camera, 4 - Particle holder, 5 - Rotameter, 6 - Computer

FIGURE 4.2: Photo of the GTB test rig

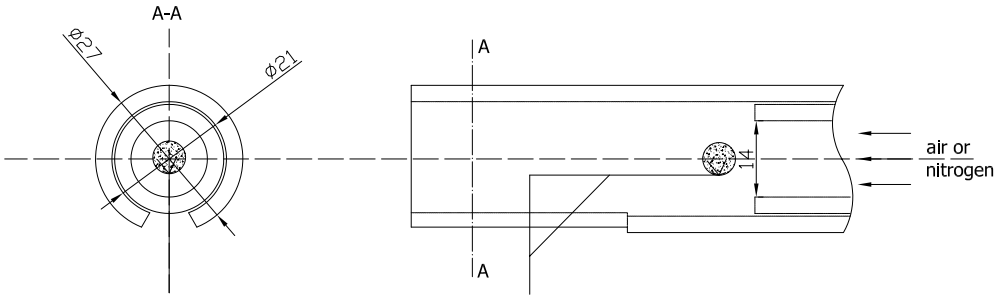

FIGURE 4.3: The scheme of the outlet pipe and the particle holder

4.2 Preliminary studies

Preliminary experiments have been performed in order to determine experimental conditions for detailed research. One of the important parameters is the gas temperature, which is controlled by the electrical furnace and the gas flow rate. The highest temperature of the electric pipe furnace has been determined to be 1200°C. A K-type NiCr-NiAl thermocouple, connected to Data Acquisition/Switch Unit Agilent 34970A has been used to measure gas temperature. The thermocouple ending is placed at the pipe axis just in front of the ceramic tube outflow, in the place where during experiments the particle is placed (see Fig. 4.3). The rotameter has been calibrated and the volumetric flow rate range was designated to be $100 - 800\ dm^3/h$ for $p = 1.01325\ bar$, $t_{air} = 20$°C. Figure 4.4 displays thermocouple temperature and gas temperature variations with volumetric flow rate for flow of nitrogen and air.

The thermocouple temperature increases initially with increasing volumetric flow rate (Fig. 4.4) for both air and nitrogen. However, exceeding the air flow rate above circa $500\ dm^3/h$ results in a decrease of the thermocouple temperature. The maximum attainable thermocouple temperature is equal to circa 740°C. When corrected for radiation losses this corresponds to circa 800°C. When a nitrogen is used, the gas temperature is around 10°C lower than for air flow. The procedure for recalculation of thermocouple readings to real gas temperature is described in Appendix A. Having a gas temperature, thus knowing density of gas, the gas velocity is estimated to be around to $3.3\ m/s$.

A subsequent step is selection of coal or char particles size. Particle size is determined by trial and error method taking into account the test rig bench restrictions. The particle must be small enough to be placed on the stand, however, it should not touch the inner wall of the steel pipe ($d_{inner} = 21\ mm$), since it could cause the errors during mass recording. On the other hand the particle should not be too small otherwise it may fall down from the particle holder. The

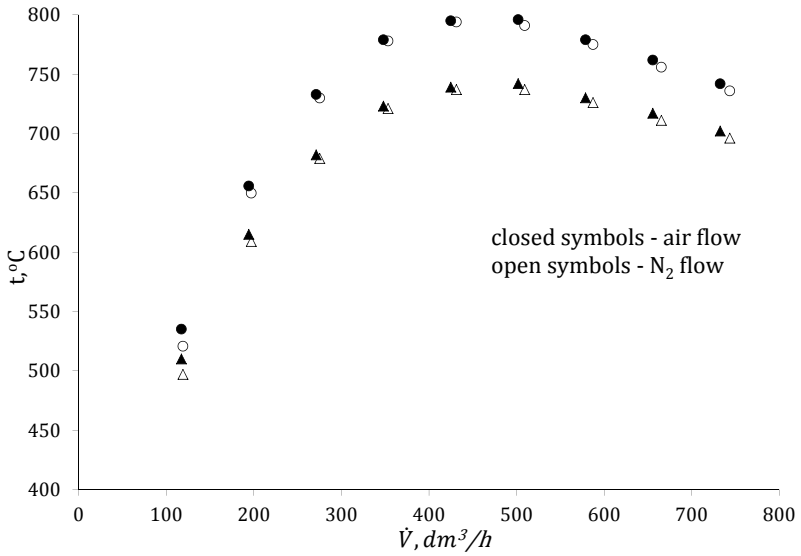

FIGURE 4.4: Thermocouple (triangles) temperature and gas (circles) temperature dependence with gas volumetric flow rate; gas temperature obtained after correcting the thermocouple readings for radiation losses; Electric furnace temperature of 1200°C

proper coal/char particle diameter has been determined to be in the range of $4 - 8$ *mm* which is a typical size class for fluidized bed combustion.

4.3 Coal devolatilization experiments

Excluding a moisture release, devolatilization is the first step in combustion of a solid fuel. Volatiles content in coal can reach 50% (dry ash free basis) in case of lignite [43]. Devolatilization is important, since it influences ignition and determines combustion stability in the boiler [43]. The time which is needed for char oxidation is much longer in comparison to devolatilization and volatiles combustion time scales, therefore, the char oxidation rate determines combustion efficiency.

In the literature, process of single grain devolatilization in non-reactive atmosphere is widely described. Usually, because of the dependence of the process on heat transfer into and inside the particle [44], a temperature of particle center was measured [45–50]. Typically, particle center temperature was measured by a thin thermocouple inserted into it. This technique, restricted to particles larger than 3 *mm* [46], has disadvantages discussed by Heidenreich and Zhang [50]. They concluded, that thermal conductivity of the thermocouple has a substantial impact on the measurements and results in overestimation of the temperature during devolatilization. Typically, coal particles are manually shaped to approximately spherical shape [45–51]. This improves measurements repeatability and facilitates comparison with devolatilization models of single spherical coal particle.

Char particles, needed for char combustion experiments of single char particle in GTB, char combustion and gasification experiments in TGA (Chapter 5) and for char physical properties determination using mercury porosimeter (Chapter 6), have been generated using the GTB test rig. To this end, coal particles have been devolatilized in pure nitrogen at about 790°C. The following section delivers some information regarding devolatilization rate and overall devolatilization time of a single larger coal particle.

4.3.1 Measurement procedures

For devolatilization experiments particles with original shape are used. In order to maintain similar particles mass, the samples are weighted and selected to weight between $0.2 - 0.3\ g$. This particles group is used later for combustion of single char particle in GTB and for measurements using mercury porosimetry. The second group, in the mass range of $0.025 - 0.07\ g$, has been used only for determination of devolatilization rate. To preserve similar experiments conditions during coal particle devolatilization, the following experimental procedure has been undertaken:

- Warming up the electric tube furnace to 1200°C;
- Nitrogen flow initialization in order to warm up the outflow pipe;
- Turning the valve off to terminate nitrogen flow;
- Placing the particle on the particle holder and positioning the stand on the analytical balance;
- Switching on the mass recording system;
- Nitrogen flow initialization;
- Turning off the nitrogen flow and the mass recording system;
- Particle quenching in pure nitrogen;

The particle mass has been recorded every second. The volumetric nitrogen flow rate for each test is kept constant at 510 dm^3/h, which provides the gas temperature about 790°C (Fig. 4.4).

4.3.2 Results and discussion

Figure 4.5 shows the particle mass as function of devolatilization time, while in Figure 4.6 the particle mass is normalized by its initial mass. Here the devolatilization is treated together

with moisture release. The measured data plotted in Figure 4.5 and Figure 4.6 corresponds to ten particles sizes of the same hard coal from "Janina" coal mine. Table 4.1 lists the initial particle masses and shows calculated values of equivalent spherical diameter ($d_{p\,e}$) and of particle surface to volume ratio (S_p/V_p) for the ten experiments performed. The equivalent spherical diameter has been estimated from initial particle masses and from average apparent bituminous coal density (1320 kg/m^3 [52]).

TABLE 4.1: Initial mass, calculated equivalent diameter and surface to volume ratio of coal particles

Particle no.	1	2	3	4	5	6	7	8	9	10
m_p, g	0.214	0.225	0.283	0.272	0.257	0.217	0.279	0.223	0.237	0.267
$d_{p\,e}, mm$	6.8	6.9	7.4	7.3	7.2	6.8	7.4	6.9	7.0	7.3
$S_p/V_p, 1/cm$	8.9	8.7	8.1	8.2	8.3	8.8	8.1	8.7	8.6	8.2

As shown in Figure 4.5 the devolatilization time is rather independent on the initial mass of the particle in the presented initial mass range, what is in contradiction with results of Ross et al. [49], who investigated devolatilization in nitrogen and in air of spherical coal particles in the diameter range of 6.5 – 14.5 *mm*. This means that surface to volume ratio changed between 4.1 – 9.2 $1/cm$ in work of Ross et al. [49]. In the present work this ratio changes only slightly from particle to particle (see Table 4.1). Since such a small difference, the devolatilization time dependence with initial particle mass is overshadowed by nonuniform particles composition, their initial shape and swelling effects, which enhances particle heating rate due to surface increase.

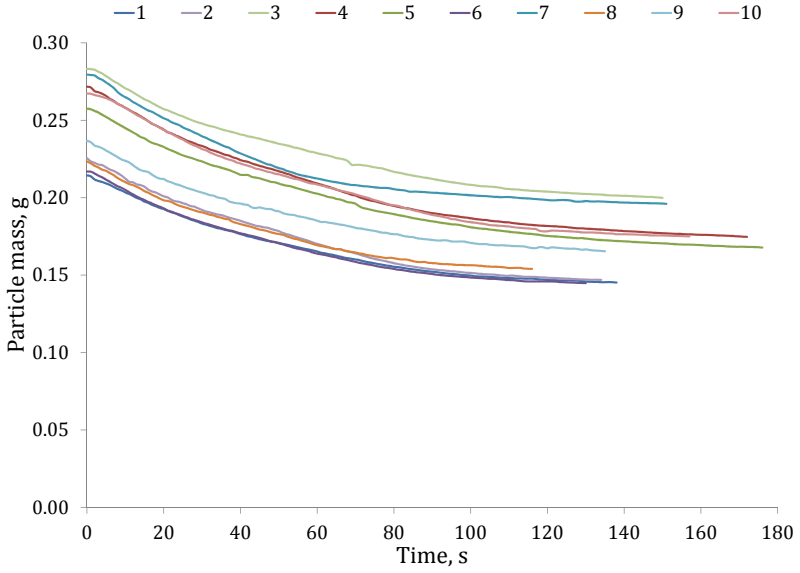

FIGURE 4.5: Mass of coal particles (for identifications of experimental runs see Table 4.1) plotted against devolatilization time

The volatiles and moisture content is in the range of 30 – 35% (Fig. 4.6). A slight dependency between initial particle mass and amounts of volatiles given off could be observed. The

greater initial mass the smaller is volatiles content. In such particles, the volatiles release could be restricted through lack of pore openings in created char. This means that even if part of mass is transformed from solid to gas state, this mass still remains in the particle. This is the reason why content of volatiles and moisture is different from circa 41% measured in the laboratory (see Table 3.1).

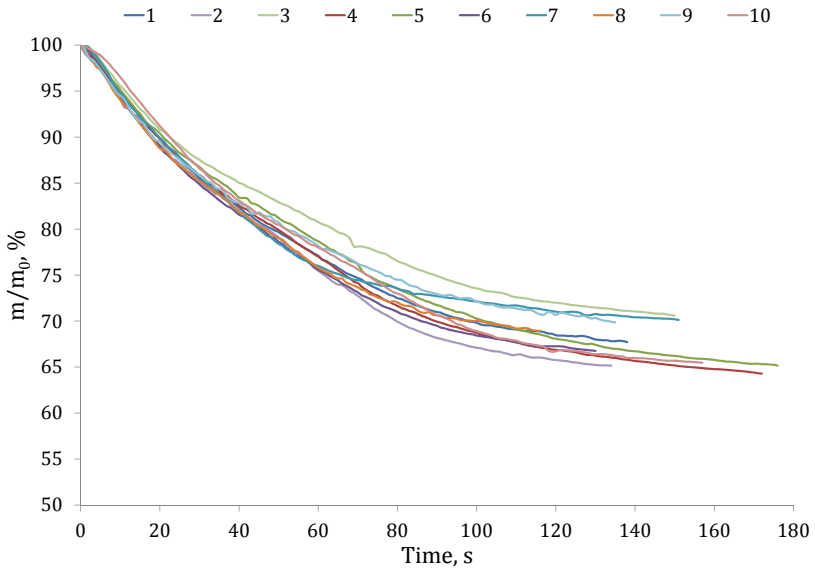

FIGURE 4.6: Normalized mass of coal particles (for identifications of experimental runs see Table 4.1) plotted against devolatilization time

Figure 4.7 shows normalized devolatilization rate (char free basis) plotted against time of the devolatilization process for four coal particles. Initially, the devolatilization rate attains the maximum at circa 10 s, what is caused by both water evaporation and primary transformation of the solid material to gas state. Afterwords, devolatilization rate decreases strongly until $40-50$ s, where a weak peak of volatiles release rate is observed. A two-stage coal devolatilization has been also considered in the literature [53, 54].

On the basis of the ten measurements shown in Figure 4.5 and Figure 4.6 an average devolatilization rate has been calculated. Calculations have been performed using the data in the 10% - 85% volatiles release range. The normalized average devolatilization rate has not been found to be correlated with the initial particle mass, when the particles initial mass is in the range of 0.214 - 0.283. In this initial mass range a foreseen larger average normalized devolatilization rate for smaller particles is overshadowed by coal composition and initial shape, which change from particle to particle. The average devolatilization rate equals to circa $1\%/s$ in the considered initial particle mass range.

In order to examine if devolatilization rate is also not depended on initial mass of smaller particles, the devolatilization experiments have been conducted for particle mass range of $0.028-0.066$ g. In the range, in which particles initial mass varies between 100% and 236% of the

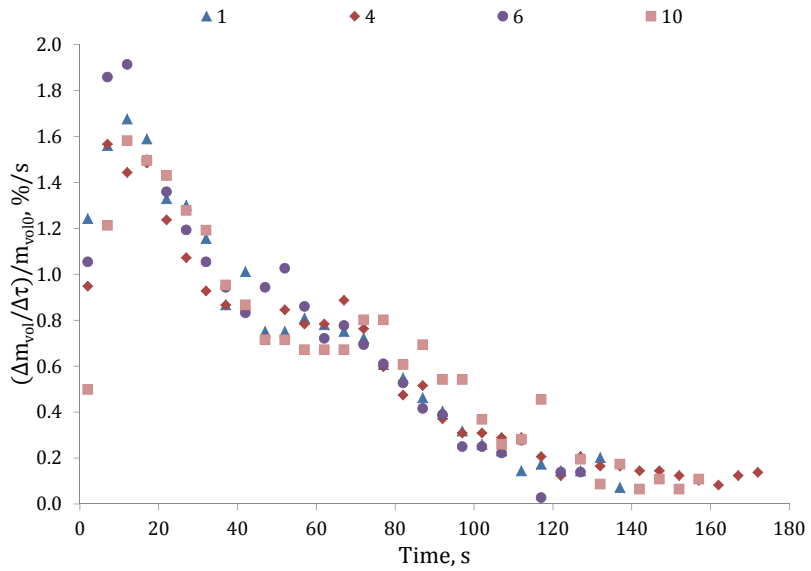

FIGURE 4.7: Normalized weight loss rate of volatiles and moisture (char free basis) plotted against time; Particles initial mass is shown in Table 4.1

smallest particle mass (Table 4.2), a correlation between initial particle mass and normalized devolatilization rate (char free basis) is observed. The larger the initial mass, the more intense is devolatilization. However, also in this initial particle mass range, some exceptions have been found, for instance for particle no. 9. Obviously, the devolatilization for particles in the mass range shown in Table 4.2 progresses much faster than for particles listed in Table 4.1. The normalized particle mass (char free basis) comparison of five particles in the lower mass range and five in the higher mass range is shown in Figure 4.8. For smaller particles (1-5) the mass loss is much more intense at the beginning of devolatilization. Around 80% of humidity and volatiles is released within first 30 *s*, while for larger particles (6-10) this stage of devolatilization is found between 70 and 90 *s*.

TABLE 4.2: Initial mass and average devolatilization rate of coal particles

Particle no.	1	2	3	4	5	6	7	8	9
m_p, g	0.035	0.038	0.028	0.029	0.053	0.066	0.046	0.048	0.047
$d_{p\,e}$, mm	3.7	3.8	3.4	3.5	4.2	4.6	4.1	4.1	4.1
S_p/V_p, $1/cm$	16.2	15.8	17.5	17.3	14.1	13.1	14.8	14.6	14.7
Devolatilization rate, $\%/s$	2.6	2.4	2.9	2.8	1.7	1.4	2.4	2.0	1.5

The performed devolatilization study shows that devolatilization rate is depended on initial particle mass. However, if too narrow initial mass range is taken for investigation, the correlation between devolatilization rate and initial particle mass can be masked by irregularity of initial particle shape (when original shape particles are studied) and probably by composition differences between various particles.

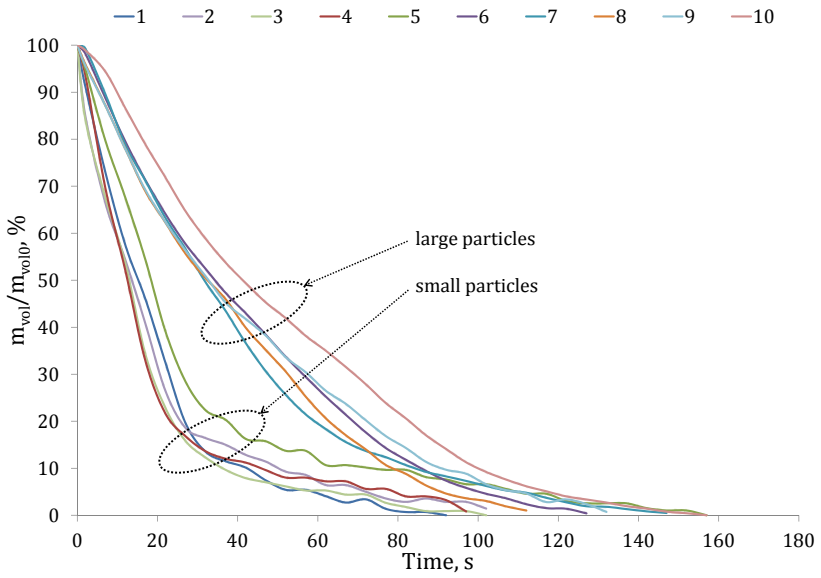

FIGURE 4.8: Normalized particles weight (char free basis) plotted against devolatilization time; Initial mass of particles 1-5 is shown in Table 4.2, while of particles 6-10 in Table 4.1

4.4 Char combustion experiments

Char combustion is the final step of coal utilization in the boiler. While designing fluidized bed boilers, the entire particle burnout time has to be taken into consideration. Because char conversion time is significantly larger than devolatilization time, thus char combustion has a pronounced effect on boiler performance. Experimental investigations on larger char particle combustion are numerous [55–64]. Usually the center particle temperature [56, 58–61, 63] has been measured; in the work of Remiarova et al. [55] particle surface temperature and a particle center temperature have been measured. The mass loss of the particle is also considered in some works, however, only in a few publications this quantity is measured directly [55, 57, 58, 62, 64]. Char mass loss rate is sometimes calculated from the CO and CO_2 concentrations in flue gases [59–61]. The above mentioned studies have been carried out in pure gas flow or in presence of inert material (sand). In this thesis the particle mass is determined by direct measurement using analytical balance and particle surface temperature using non intrusive method.

4.4.1 Measurement procedures

In the char combustion tests, presented in this thesis, both spherical and original shape char particles have been used. Particles spherical shape is attained by manual treating of char, which has been obtained during coal devolatilization performed in the GTB test rig (see Section 4.3). The initial mass of char particles is in the range of $0.06-0.2\ g$. The experimental procedure for char combustion is as follows:

- Warming the electric furnace to 1200°C;
- Air flow initialization in order to warm the outflow pipe up;
- Turning the air valve off to terminate the air flow;
- Placing the particle on the particle holder and placing the stand on the analytical balance;
- Switching on the mass recording system;
- Switching on the infrared camera recording system;
- Air flow initialization;
- Continuous mass and particle surface temperature recording;
- Turning off the air flow;
- Particle holder cleaning for the next test;

The particle mass is recorded every second, while surface temperature every three seconds. The volumetric flow rate and air temperature have been maintained constant during experiments at 500 dm^3/h and 795°C respectively (Fig. 4.4). In the char combustion experiments, besides particle mass also particle surface temperature has been recorded. Measuring surface temperature using infrared camera requires surface emissivity, which in this work is assumed to be 0.8 [53, 65–68].

Before placing the particle on the particle holder, mass of all of the particles have been measured. The diameter of manually rounded char particles has been determined by caliper. Table 4.3 shows the mass and diameter for some char particles. For particles shape comparison see Figure B.1 in Appendix B.

4.4.2 Results and discussion

Examples of spherical char particle mass and maximum surface temperature changes with combustion time are shown in Figure 4.9 and marked with solid lines. The graph corresponds to the first five particle sizes listed in Table 4.3. It can be seen that the smaller the particle, the shorter is the combustion time. This relation is in agreement with many other works [47, 59, 61, 63, 64]. For instance Komatina et al. [63] has investigated the process of combustion in air using two Serbian coals. Particles in the $5 - 10$ *mm* range, which were initially rounded, were used. The temperature of the bed in the laboratory-scale fluidized bed furnace and the center temperature of spherical coal particles were measured. The bed temperature was in the range of $590 - 710$°C. The coal particle was drilled, before the thermocouple was inserted inside the

TABLE 4.3: Mass and diameter of char particles

Particle number	**Mass,** *g*	**Shape**	**Diameter determined by caliper,** *mm*	**Equivalent spherical diameter*,** *mm*
1	0.085	spherical	5.2	5.2
2	0.068	spherical	4.8	4.8
3	0.151	spherical	6.7	6.3
4	0.126	spherical	6.2	5.9
5	0.086	spherical	5.3	5.2
6	0.150	original	-	6.3
7	0.112	original	-	5.7
8	0.129	original	-	6.0
9	0.119	original	-	5.8
10	0.121	original	-	5.8

*Particles diameter estimated from mass and char apparent density of 1163 kg/m^3 (see Table 6.1)

grain, after that the ceramic glue was used to fix the thermocouple. The particle was initially devolatilized in pure nitrogen, which was followed by combustion of the remaining char in air. It was found that the particle center temperature history was influenced by the rank of coal and the initial particle size. The smaller the particle and the lower coal rank the larger was the difference between particle canter temperature and bed temperature. These experiments, using char produced from Kosovo lignite, showed also that the particle diameter increase from 5 *mm* to 7 *mm* doubled the combustion time [63].

In the present work, however, the deviation from relation between particle size and char combustion time has been found for instance for particle no. 1, which the initial mass is identical to particle no. 5 (Table 4.3), but combustion time is about 110 *s* longer. Longer combustion time can be caused by different char physical and chemical properties from particle to particle. Particle no. 1 is clearly characterized by a higher ash content (for examples of ash remains see Fig. B.3) comparing to other shown particles (Fig. 4.9). The average combustion time for particle size circa 6 *mm* is about 3 minutes.

Figure 4.9 presents also the maximum particle surface temperature as function of time (dotted lines). The maximum particle surface temperature is the highest temperature registered by IR camera assuming 0.8 particle surface emissivity. Initially the particle is heated up from room temperature to the gas temperature. During this time moisture is released. Subsequently char combustion is initialized, what is visualized by quick temperature increase. From the temperature roughly 1400 – 1500 *K* steady char combustion proceeds, what is usually characterized by a slight increase of the maximum recorded surface temperature. Probably this phenomena has been caused by increased combustion rate and possible partial particle thermal isolation through ash layer, which remained on the unburned particle core, what also was observed by Zajdlik et al [62]. The temperature measurements of particle surface is, however, not accurate,

because the emissivity changes with temperature [18] and with char structure alterations during combustion. The surface temperature of 1400 K obtained for 0.8 emissivity will change to 1521 K and 1304 K if the particle surface emissivity is changed to 0.7 and 0.9 respectively.

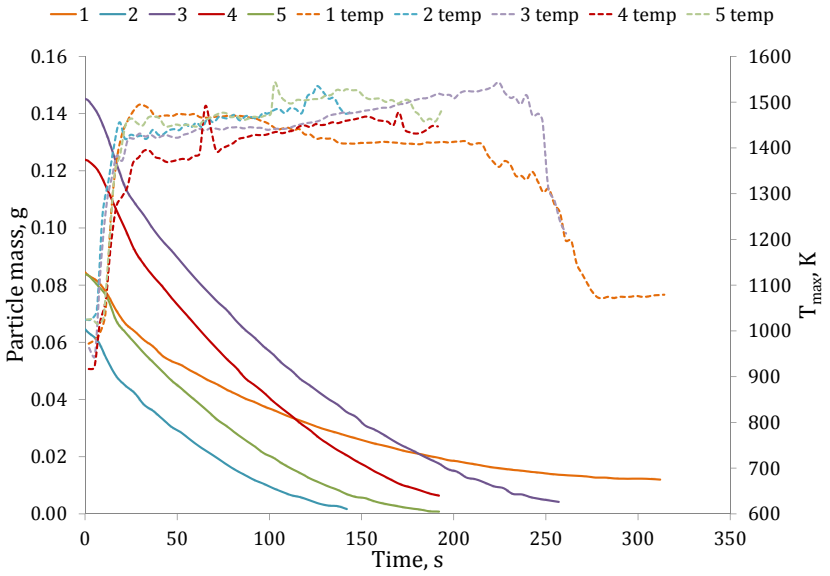

FIGURE 4.9: Char mass (solid lines) and maximum temperature of particle surface (dotted lines) plotted against time of combustion; Numbers 1-5 indicate particles listed in Table 4.3

The combustion rate normalized to ash free char is shown in Figure 4.10. The initial intensive mass loss rate is due to moisture evaporation and release of remaining volatiles. This high rate is correlated with maximum temperature increase rate (see Fig. 4.9). From circa 25 s onwards, the continuous decrease of the normalized combustion rate is observed, which is caused by steady decrease of unreacted char core diameter. The unburned particle core decrease could be observed during experiments with both the naked eye (sample image shown in Fig. B.2) and using IR camera (Fig. 4.11). Figure 4.11 shows stages of char particle combustion (particle no. 4 in Table 4.3). The first image (a) indicates the temperature just before the air flow has been switched on. On image (b) char particle is shown after entire surface ignition, which occurs at 36 s. The temperature, which has been indicated there (yellow color) is in the order of 1400 K. Images (c) and (d) show subsequent stages of char combustion, which can be characterized by shrinking, yellow, high temperature region.

Comparison of combustion times, for nearly-spherical and non-spherical char particles, shows that initial shape of the char particle has negligible effect on the combustion time of particles with initial mass of $0.06 - 0.2$ g (Fig. 4.12). For instance, combustion times of particles no. 4, 9 and 10, having similar initial mass (Table 4.3), despite different shape (see Appedix B), vary only by circa 15 s or less, when taking 85% char burnout as a reference. When comparing particles no. 3 and 6, which have similar initial mass (see Table 4.3), a significant difference in combustion time is found. However, this difference is not a result of shape differences between particles, but rather of the high ash content and its compact structure, which has been

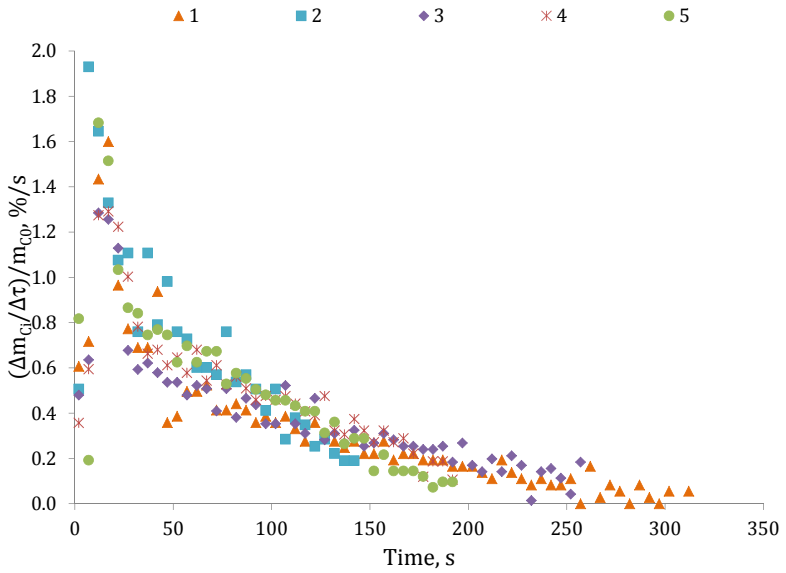

FIGURE 4.10: Normalized char combustion rate (ash free basis) for spherical particles (shown in Table 4.3) plotted against time of combustion

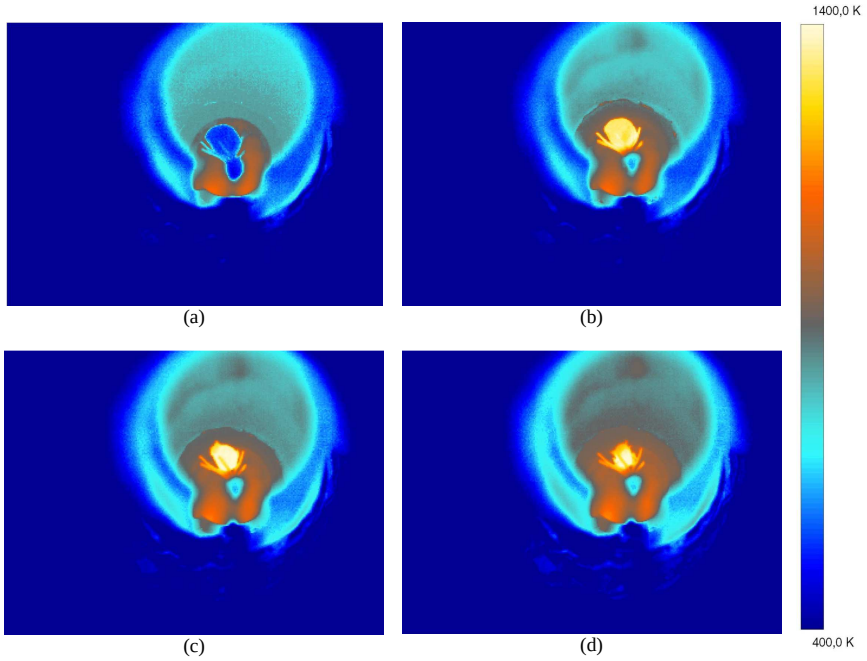

FIGURE 4.11: Infrared images of burning char particle no. 4 (Table 4.3) taken at: (a) 0 *s*, (b) 36 *s*, (c) 118 *s*, (d) 178 *s*

found for particle no. 6 (ash content circa 12%). Generally speaking, the combustion time for larger original shape char particles is greater than for smaller particles (see Fig. 4.12), what is in consistency with results obtained for spherical particles.

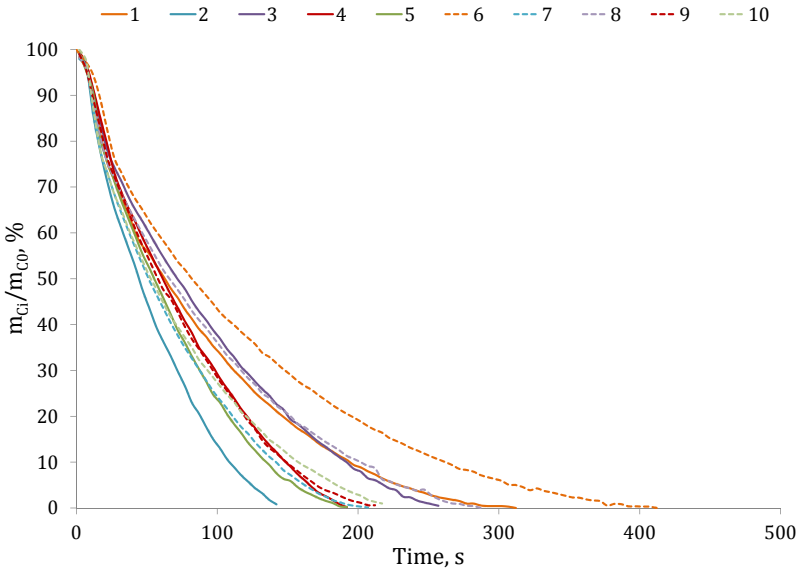

FIGURE 4.12: Comparison of normalized char mass (ash free basis) during combustion for spherical (solid lines) and non-spherical (dotted lines) char particles; For identification of experimental runs see Table 4.3

4.5 Coal combustion experiments

Single coal combustion experiments have been performed to examine the combustion process in conditions prevailing in fluidized bed boilers. In the literature, the temperature [47, 48, 63, 69–71] and mass loss [47, 48, 70–72] of a single coal particle were usually investigated.

4.5.1 Measurement procedures

The procedure, as well as conditions, in which coal combustion tests have been carried out are similar to those applied in the char combustion (Section 4.4). In order to indicate the difference in combustion behavior of spherical and original shape particles, some nearly spherical particles have been prepared (see Fig. B.1). Table 4.4 lists the masses and diameters of the samples studied.

4.5.2 Results and discussion

Figure 4.13 displays mass loss (solid lines) and maximum particle surface temperature (dotted lines) as function of combustion time for spherical coal particles. Particle heating up,

TABLE 4.4: Mass and diameter of coal particles

Particle number	**Mass** *g*	**Shape**	**Diameter determined,** *mm* **by caliper,** *mm*	**Equivalent spherical diameter*,** *mm*
1	0.186	spherical	6.5	6.5
2	0.118	spherical	5.7	5.5
3	0.175	spherical	6.0	6.3
4	0.133	spherical	6.0	5.8
5	0.082	spherical	5.3	4.9
6	0.090	original	-	5.1
7	0.109	original	-	5.4
8	0.210	original	-	6.7
9	0.116	original	-	5.5
10	0.099	original	-	5.2

*Particles diameter estimated from mass and coal apparent density of 1320 kg/m^3 [52]

devolatilization, volatiles ignition and char combustion are easy to identify. Particle warm up is followed by moisture evaporation. Subsequently the devolatilization process begins. Till this time (approximately $10 - 15$ *s*), the mass loss and temperature increase are relatively small. However, at some point the ignition of volatiles occurs, which accelerates the devolatilization, resulting in a rapid decrease of particle mass. Also the maximum surface temperature increases rapidly during this process. From the temperature-time history the devolatilization time can be calculated. For a 6 *mm* particle devolatilization time is in the range of $20 - 30$ *s*, which is in agreement with the study [48] involving sub-bituminous coal form India. During the quick devolatilization a long, yellow, sooty flame surrounding the particle has been observed (see Fig. B.2 in Appendix B). As shown in Figure 4.13, the char combustion is characterized by almost constant maximum recorded surface temperature (constant maximum temperature of particle center also observed by Winter et al. [47]) and by an exponential decrease of particle mass. This process takes place, when most of volatiles are already released [48, 64, 73]. Volatiles ignition moment, however, takes place at different instances. Figure 4.13 shows, that particle no. 1 ignites much latter in comparison with other particles. This is attributed to the largest initial mass of the particle and the biggest diameter (Table 4.4). For volatiles ignition to occur, the surface temperature has to exceed the ignition temperature, thus smaller particles ignite quicker [47, 48].

The relative coal combustion rate (ash free basis) for spherical particles is presented in Figure 4.14. The largest combustion rate has been obtained in the period, when volatiles are combusted. Char combustion has been found to be about ten times slower than devolatilization. The same relationship was found also by Pełka [71, 72], who investigated combustion of 10 *mm* particles for variety of Polish coals. Pełka [71, 72] carried out experiments at $650 - 850$°C temperature and in the flow of air or air with sand. He found a rapid mass loss after initialization of combustion at 850°C. Dependent on coal type, the combustion time was in the range of 700 –

1100 *s* [71, 72]. In some tests also the surface temperature was measured using a thermocouple. Similar temperature dependencies to the ones shown in Figure 4.13 were obtained in Pełka's study [72].

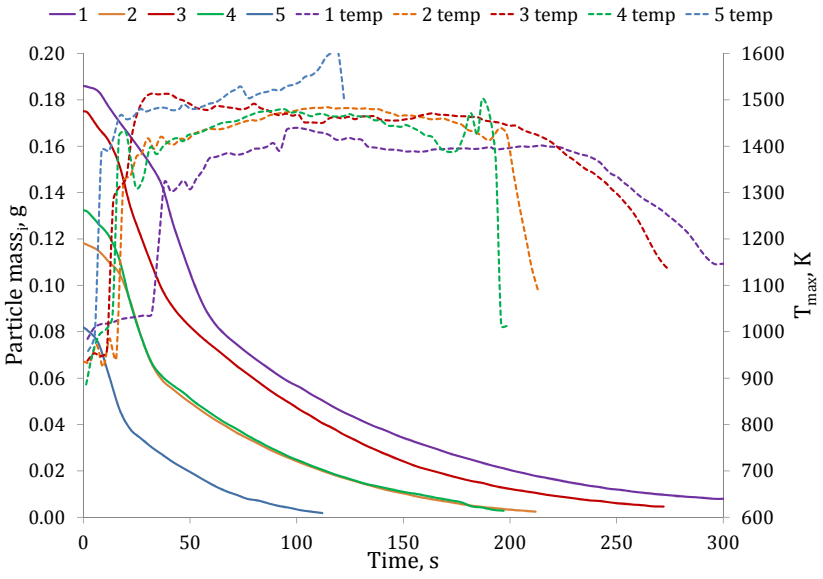

FIGURE 4.13: Coal mass (solid lines) and maximum particle surface temperature (dotted lines) plotted against time of combustion; Particles initial mass shown in Table 4.4

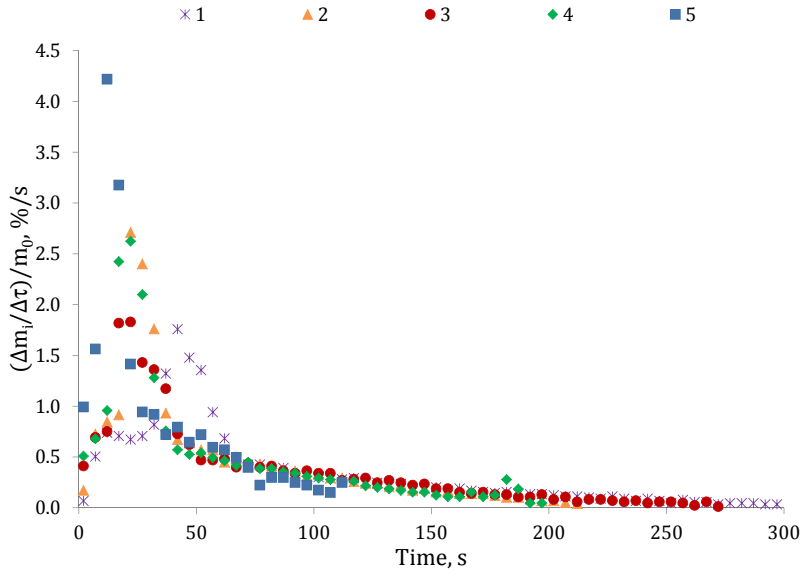

FIGURE 4.14: Normalized coal combustion rate (ash free basis) for spherical particles plotted against time of combustion; Particles initial mass shown in Table 4.4

The above identified stages of combustion can also be recognized in the infrared images shown in Figure 4.15. Image (a) shows the coal particle temperature before the air flow is initialized; the surface temperature is lower than 400 *K*. Image (b) shows the coal particle during its highest mass loss rate at 26 *s* instance, which appears during volatiles combustion. Image (c) shows the particle surface temperature during char combustion, which is larger than

1400 K. The last image shows final stages of combustion, which are characterized by shrunken reacting char core surrounded by an ash layer, characterized by a lower surface temperature. The swelling effect occurring between stages (b) and (c) is visible.

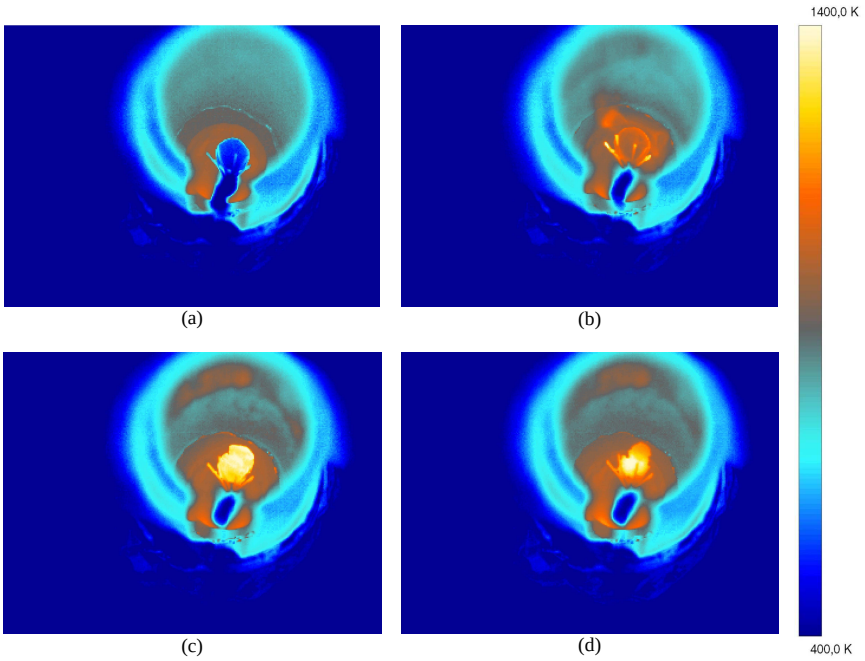

FIGURE 4.15: Infrared images of coal burning particle no. 4 (Table 4.4) taken at: (a) 0 s, (b) 26 s, (c) 39 s, (d) 156 s

Figure 4.16 shows the influence of coal particle shape on its combustion process. The irregular particle shape facilitates the ignition process, even when the particle mass is as large as 0.21 g (Table 4.4). An irregular shape has "ribs" on the surface, which are heated immediately after hot air flow is initialized. Once the volatiles are ignited and a flame embraces entire particle, an almost linear relative mass loss is observed. Similarly to char combustion (Section 4.4), also during coal combustion tests the influence of initial particle mass on total combustion time has been observed; the larger the particle mass the longer is the combustion time [47]. However, when particle initial diameter is taken into account, similar correlation cannot be observed. Also is not possible to state if particles with irregular shape or with regular burn faster. This could be explained by change of the particle shape and size due to swelling and probably by different composition of each particle. These observations were also made by Malik et al. [70].

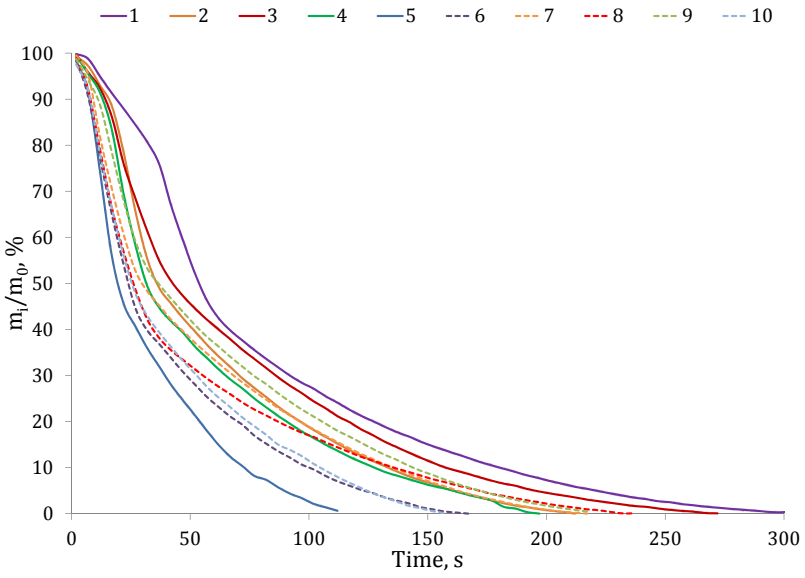

FIGURE 4.16: Decay of normalized coal mass (ash free basis) as function of time for spherical (solid lines) and non-spherical shape (dotted lines) coal particles ; Particles initial mass shown in Table 4.4

Chapter 5

Thermogravimetric analysis

Thermogravimetry (TGA) is the most popular and perhaps the simplest method of fuel characterization. Devolatilization, char combustion and gasification rates can be determined using TGA.

The aim of the TGA investigation presented in this thesis is to verify whether TGA technique can be used to determine kinetic parameters applicable to predicting combustion rates for fluidized bed technology. This question, because of fundamental differences between conditions prevailing in fluidized bed boilers and in the TGA apparatus, has not an obvious answer [74]. In fluidized bed boilers, the particle size is in order of *mm*, while in TGA micronized particles are used. Availability of fresh gas mixture at particles surface is restricted in TGA by construction of sample carrier and device itself, while in FB boilers is unlimited. Particle heating rates are substantially different; in the TGA a typical maximal heating rate is around 50 K/min (depending on the device), while in FB boiler few hundreds K per second. All these issues make applicability of TGA conversion rates to large particles combustion questionable. In order to deal with these issues, the preliminary studies described in Section 5.2 have been performed. On the basis of these preliminary experiments the proper conditions for final tests have been selected. The basic TGA experiments consist of the following investigations:

- Coal devolatilization in nitrogen;
- Coal char combustion in O_2/N_2 atmosphere;
- Coal char gasification in CO_2/N_2 atmosphere;

5.1 Experimental setup

Experiments on devolatilization and char combustion/gasification have been performed using thremogravimetric analyzer Netzsch STA 409 PG shown in Figure 5.1. The main parts are (Fig. 5.2): gas rotameters (1), balance system (2), high temperature electric furnace (3) and sample holder with crucible (4). The high temperature furnace is able to operate in temperatures up to 1500°C with heating rates reaching 50 K/min. Sample weight is restricted to 18 g and mass measurement resolution is 2 μg. Three different gases can be used in the experiments. The gas volumetric flow rate range, for each rotameter is $5 - 190$ ml/min (calibrated using nitrogen) [75]. Figure 5.1 shows the thermogravimetric analyzer with a sample placed in the crucible.

FIGURE 5.1: Photo of the thermogravimetric analyzer
(photo taken by Sławomir Sładek)

5.2 Preliminary studies

In order to determine experimental conditions, for gathering required data, preliminary studies have been performed. Firstly, the choice of crucible has been studied, since mass transfer rates may be affected by crucible. Two crucible types made both out of Al_2O_3 can be used: a platter and a cup-like crucible. Diffusion limitations of char conversion rates during char

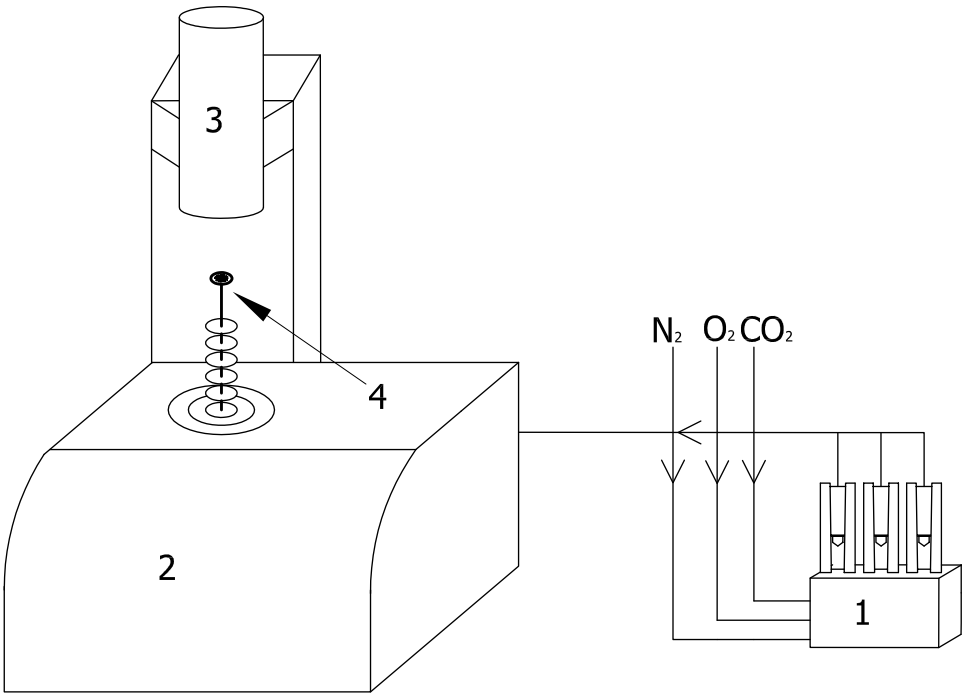

FIGURE 5.2: TGA scheme; 1 - gas rotameters, 2 - balance system, 3 - high temperature electric furnace, 4 - sample holder with crucible

gasification in TGA were studied by A. Gomez-Barea et al. [66]. A gas stagnation region inside the cup-like crucible was blamed for gas diffusion resistance. The platter crucible facilitates the access of gas, flowing from TGA bottom, to the sample surface [66, 76, 77]. Therefore in this work a plate-like crucible have been used. The illustration of gas flow around the sample holder in TGA is shown in Fig. 5.3.

The amount of fuel put into the crucible plays an important role due to two factors. Firstly, the gas diffusion resistance is affected by the amount of fuel [66, 76–80]. This phenomenon was described in details by Nowak et al. [77]. The diffusion resistance through the bed was responsible for a CO_2 concentration decrease in the bed, at higher temperatures (>800°C), which slowed down the gasification rate [77]. The second undesirable phenomenon, which may occur when sample is too large, is sample self-heating [80], which could be followed also by quick consumption of the reactive gas nearby the sample. Two avoid these negative influences, the sample, in this study, is relatively small (8 *mg*) and uniformly distributed on the crucible bottom, as shown in Fig. 5.4, which results in small bed height. This procedure was also applied by Zolin et al. [80]. It is also important, that the gas diffusion resistance inside fuel particles is minimized. An influence of larger particle size on the gasification rate was, for example, reported by Gomez-Barea et al. [79]. The smaller the particle, the larger is the total (external and internal) area

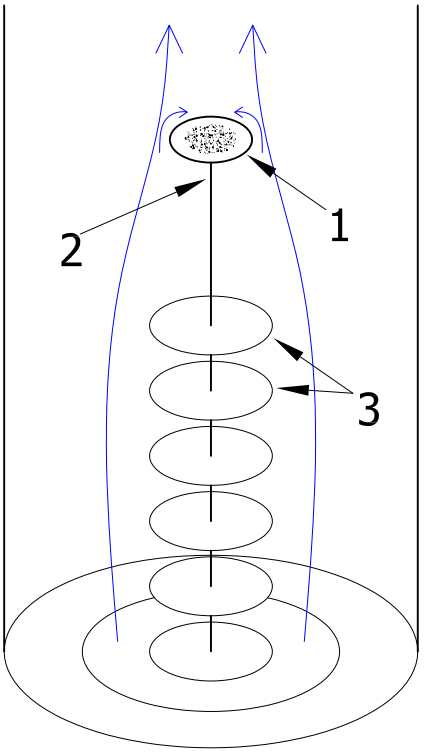

FIGURE 5.3: Gas flow profile in the TGA; 1 - crucible, 2 - sample holder with thermocouple, 3 - radiation shields

exposed to the fresh gas and the oxygen transport inside the particle is enhanced. To facilitate rapid mass transfer rate, the char particles are crushed using mortar to the particles diameter $< 0.25\ mm$. Additionally, small particles also help to maintain equal temperature in entire particle volume, which is crucial, when measurements are used for determination of kinetic parameters.

Another important issue, concerning the TGA experiments, is the gas mixture volumetric flow rate. Since the use of 10 ml/min of protective gas is a necessity, to protect the balance, therefore nitrogen volumetric flow rate has to be grater than this value. Recommended purge gas volumetric flow rates are between $20-30\ ml/min$ [75]. Recalling that extending the temperature region, in which combustion is controlled by kinetics, can be achieved by increasing O_2 or CO_2 partial pressure in the gas mixture [77], the use of 21% of purge gas (both for O_2 and CO_2) has been established. These conditions corresponds to the 79 ml/min flow rate of protective (N_2) gas. The TGA standard heating rate (10 K/min) [75] is chosen for devolatilization experiments, which is a typical rate [81–83]. For char combustion and gasification tests, the 50 K/min heating rate is used. All of above-mentioned settings assured that TGA is capable to maintain adequate conditions during many series of measurements. The last important parameter, the final temperature of combustion or gasification, has to be chosen. Because different temperatures have been used in each of considered processes, the detailed explanation of the choice of temperature is

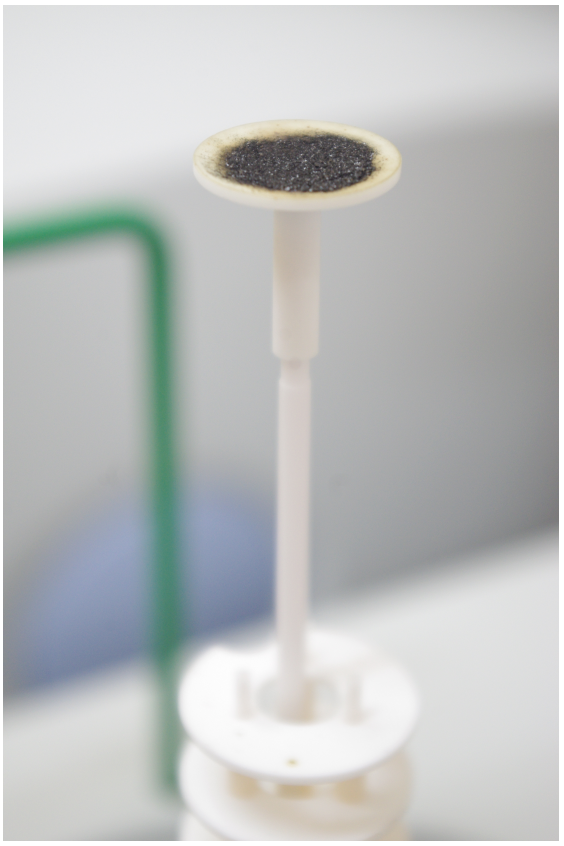

FIGURE 5.4: Magnification of the sample dispersion on the crucible
(photo taken by Sławomir Sładek)

described later in Chapter 5.

Thermogravimetric measurements can be carried out as isothermal or non-isothermal experiments. In isothermal experiments, firstly, the char heating to required temperature is performed in an inert atmosphere. After reaching the required temperature, the reactive gas flow is initialized and mass loss as function of time is recorded. Such experiments are repeated at different temperatures, which remain constant throughout the experiments. The thermogravimeter is able to keep constant temperature of sample by measuring the sample temperature and by regulating its heating power. Since each run requires several hours, the entire measurement is relatively long, what also makes the study more costly comparing to non-isothermal experiments. Non-isothermal experiments rely on continuous mass recording of the sample performed during constant heating rate. Here, the required gas mixture is supplied from the beginning and sample temperature during devolatilization, combustion or gasification process is varying. The single run is enough to attain fuel characterization at different temperature when the study is performed in non-isothermal experiments [74]. In this thesis, because of calculations simplicity of Arrhenius constants (Chapter 6) and due to the fact that in non-isothermal experiments the fuel in each time and temperature step has different composition, the isothermal experiments of

char combustion in O_2/N_2 and gasification in CO_2/N_2 have been performed. The devolatilization tests, however, have been conducted using non-isothermal conditions with standard heating rate.

5.3 Coal devolatilization in TGA

One of the goals is to examine how devolatilization conditions affect char combustion rates. To this end, two char types are produced from the same coal. The first char has been produced in the GTB test rig at high heating rates (Section 4.3), the second char has been produced in the TGA, thus at low heating rates. These two chars are named as GTB-char and TGA-char. Additionally, the TGA-char is required for determination of morphology using mercury porosimetry (Section 6.3).

5.3.1 Procedures for devolatilization studies and char generation

For char generation in the TGA, particles with original shape and mass in the range of $0.15 - 0.3\ g$ have been used. To avoid falling off such big particles from flat crucible, the cup-like crucible has been used. Three or four particles are placed into the cup-like crucible during char generation. The devolatilization tests are performed in pure nitrogen with the volumetric flow rate of 79 ml/min and with 10 K/min heating rate. Because the sample mass is large, the baseline (see Section 5.4) has negligible effect on the results, thus the single run in TGA has been carried out without baseline. The temperature control program is as follows:

- Standby program to achieve an uniform 30°C temperature of the sample;
- Sample heating up to 105°C with 10 K/min;
- Fifteen minutes isotherm at 105°C;
- Sample heating up to 750°C with 10 K/min;
- Thirty minutes isotherm at 750°C;

After cooling down the crucible to the room temperature, the sample is removed and kept in nitrogen, in a container. The procedure is repeated several times until twenty coal particles are devolatilized. Ten particles are used for kinetics study of char combustion and gasification and they are crushed in the mortar to diameter smaller than 0.25 mm. The other ten particles are used to measure their porosity, density and internal surface area.

5.3.2 Devolatilization results and discussion

Figures 5.5 and 5.6 show the relative mass (TG), relative mass loss rate (DTG) and temperature variation during the process of devolatilization in nitrogen for three series of measurements, marked as run-1, run-2 and run-3, which correspond to initial mass of 686 *mg*, 559 *mg* and 633 *mg* respectively. Initially, the particle is heated to 105°C and kept at this temperature for 15 minutes to give off moisture. The intense moisture release begins around 90°C, reaching the maximum at 105°C. During moisture evaporation, when the sample is kept at a constant temperature, the water evaporation rate is gradually decreasing. After the temperature program mode is switched to steady heating, a second stage of moisture evaporation is observed (Figure 5.6). A two-stage moisture evaporation is the result of relatively large initial masses of particles put into crucible, which limit the moisture release from inner layer of the fuel. Additionally, the heat consumption due to moisture evaporation cools down the inner part of particles and thus creates temperature gradient. The subsequent stage of solid fuel transformation begins after 40 *min* of measurements. This time corresponds to circa 280°C, which can be regarded as the initialization temperature of devolatilization. Further temperature increase invokes a rapid increase in mass loss. The local maximum of DTG is found to be at the temperature range 425°C – 440°C (see Fig. 5.6).

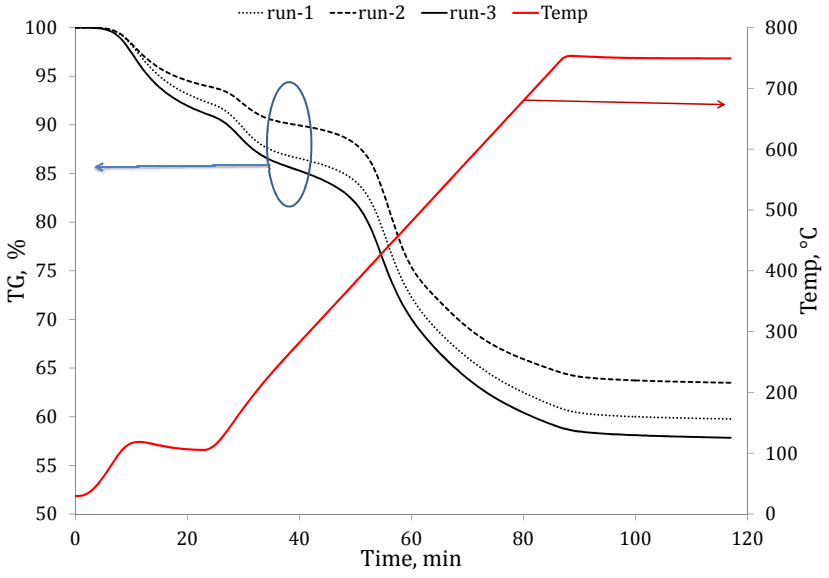

FIGURE 5.5: Relative mass (black lines) and temperature (red line) of the sample during devolatilization in TGA; atmosphere - nitrogen

In Figure 5.7 the devolatilization results, shown in Figure 5.5, have been replotted and TG_{vol} is the volatiles yield normalized to the maximum yield measured at the end of each run. The maximum yield have been measured to be 26.8%, 26.4%, 26.2% (see Fig. 5.5), for run-1, run-2 and run-3 respectively. The mass loss rate ceases, when sample temperature reaches 750°C (Fig. 5.7). At this point the devolatilization is almost completed reaching 97.6% conversion

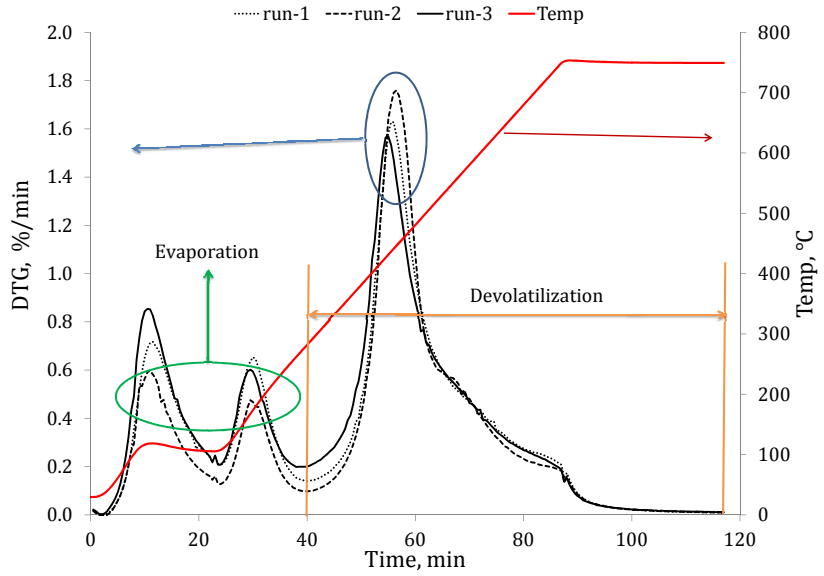

FIGURE 5.6: Relative mass loss rate (black lines) and temperature (red line) of the sample during devolatilization in TGA; atmosphere - nitrogen

(as shown in Fig. 5.7) taking as a reference state for the end of devolatilization the sample mass at 116 *min*. The average devolatilization rate calculated from the initial devolatilization temperature at 280°C is equal to $0.05\%/s$. The average value has been obtained taking 75% of volatiles release from 10% to 85% as indicated using green lines in Figure 5.7.

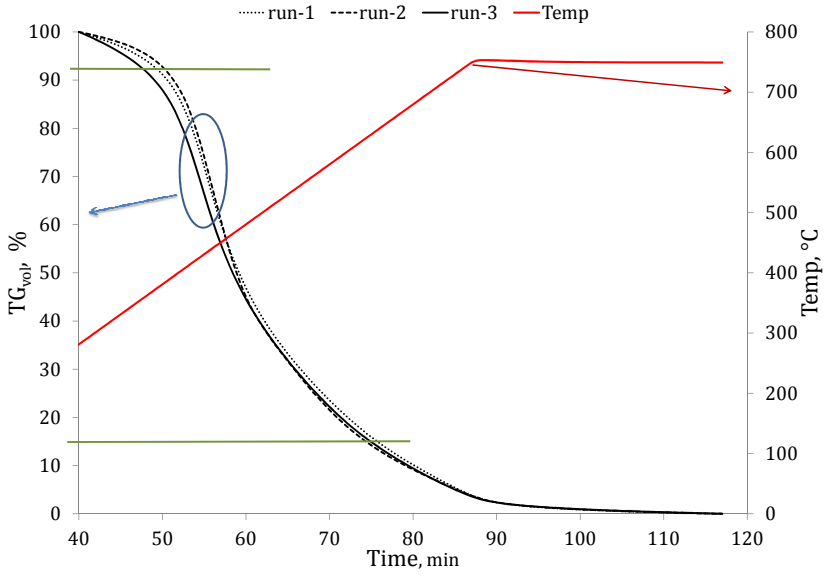

FIGURE 5.7: Relative mass of volatiles (black lines) and temperature (red line) of the sample during devolatilization in TGA; Green lines limit the range of calculations of average devolatilization rate; atmosphere - nitrogen

5.4 Coal char combustion in TGA

The aim is determination of the char combustion rates at various temperatures. Char combustion rates have been determined in TGA operated in isothermal mode.

5.4.1 Measurement procedures

The preliminary studies contributed towards the parameters selection for char combustion experiments. These parameters are presented in Table 5.1. Two types of char have been tested; char generated by coal devolatilization in GTB (GTB-char) described in Section 4.3 and char produced by coal devolatilization in TGA (TGA-char) described in Section 5.3. The following temperature program is used:

- Standby program to achieve 30°C of the sample (in N_2);
- Sample heating up with 50 K/min rate to required temperature (in N_2);
- Ten minutes isotherm at required temperature for stabilization reason of temperature (in N_2);
- Isotherm at required temperature in N_2/O_2 atmosphere ($z_{N2} = 0.79$ and $z_{O2} = 0.21$).

TABLE 5.1: TGA experimental conditions for char combustion

Sample mass, *mg*	**Granulation,** *mm*	**Crucible type**	**Protective gas flow rate,** *ml/min*	**Purge gas flow rate,** *ml/min*
≈ 8	< 0.25	platter	79	22

The duration of the last temperature program step depends on both the final temperature and char reactivity. Firstly, the experiments are carried out in 750°C, 850°C and 950°C temperatures relevant to fluidized bed combustion. Secondly, a temperature range is chosen so that combustion proceeds in the pure kinetic region of char combustion; on the basis of literature survey [80, 82–84], three temperatures 350°C, 400°C and 450°C are initially chosen. An additional experimental run is carried out at 600°C expecting that both diffusion and kinetics are relevant. The above underlined experimental procedure is firstly performed at least two times for each temperature with empty crucible, in order to obtain reliable baselines, which determine the influence of both the gas density and velocity on the balance readings during combustion tests. Figure 5.8 shows an example of baselines applicable for 850°C final temperature. For the considered case, both the blue solid line and rhombus black marks are in very good agreement, therefore both baselines could be taken for further experiments. At this particular case the blue

line is chosen. The significant drop of the mass at 26.5 *min* is caused by oxygen flow initialization, which suddenly invokes the lifting of the crucible by the hot gases flow from the crucible bottom. The red solid line displays the temperature history of the crucible.

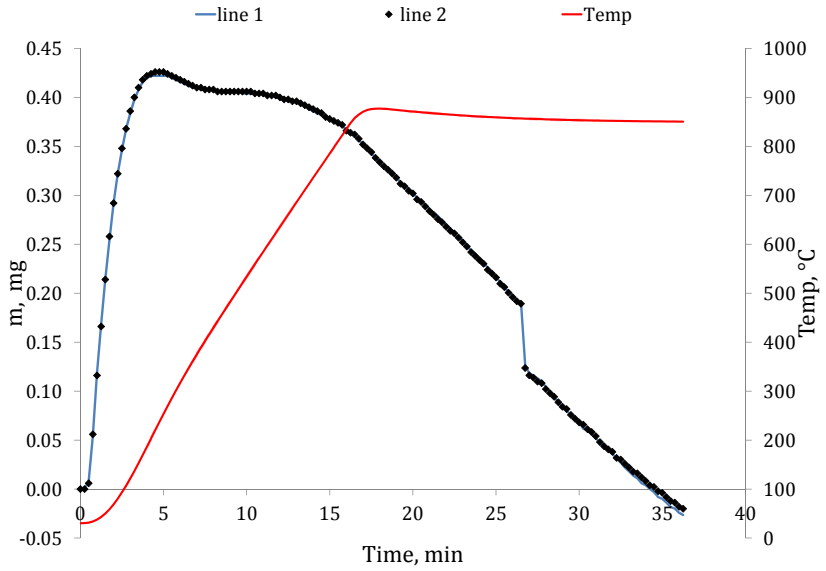

FIGURE 5.8: Baselines; The variation of the crucible mass and temperature (red line) readings during temperature program for combustion at 850°C; $z_{O2} = 0.21$, $z_{N2} = 0.79$

Each of the TGA combustion experiments has been repeated twice. When two overlapping measured data is observed the measurements are regarded as carried out correctly. The repeatability of the experiments is discussed in Section 5.4.

5.4.2 GTB-char combustion in TGA

Figures 5.9 and 5.10 show the basic TGA data. Black lines accompanied by TG symbol indicate the mass of the sample normalized to the initial sample mass, while red lines show the sample temperature. The higher the final temperature the more volatiles are released. Observed devolatilization is associated with volatiles remaining in the GTB-char. At the two lowest temperatures (350°C and 400°C) the devolatilization phase does not occur, as shown in Figure 5.10. At such low temperatures, which are only slightly above the onset temperature of devolatilization (Section 5.3), little volatiles are released. Initiating the flow of oxygen causes formation of gas mixture of 21% of oxygen and 79% of nitrogen and is the beginning of the char reactions. The dependence of the TG with time is almost linear for most of the considered final temperatures. For each final temperatures shown in Figure 5.9 of 600°C, 750°C, 850°C and 950°C, the ignition of char causes the sample to be slightly overheated, approximately 10 *K* above the set temperature. This phenomenon has not been found for temperatures in the 350°C-450°C range (Fig. 5.10), where the reaction kinetics is slow enough for TGA to maintain the set temperature.

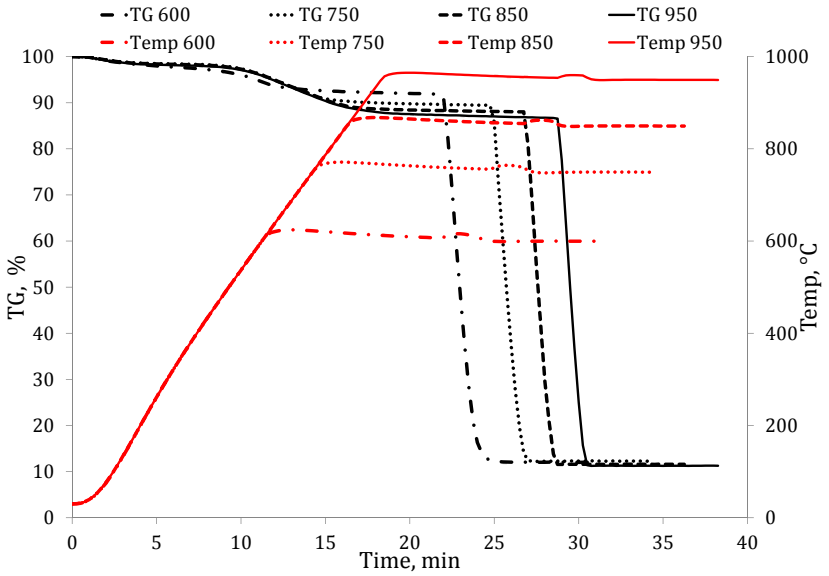

FIGURE 5.9: Relative sample mass (black lines) and temperature (red lines) during GTB-char combustion at temperatures 600°C, 750°C, 850°C and 950°C; $z_{O2} = 0.21$, $z_{N2} = 0.79$

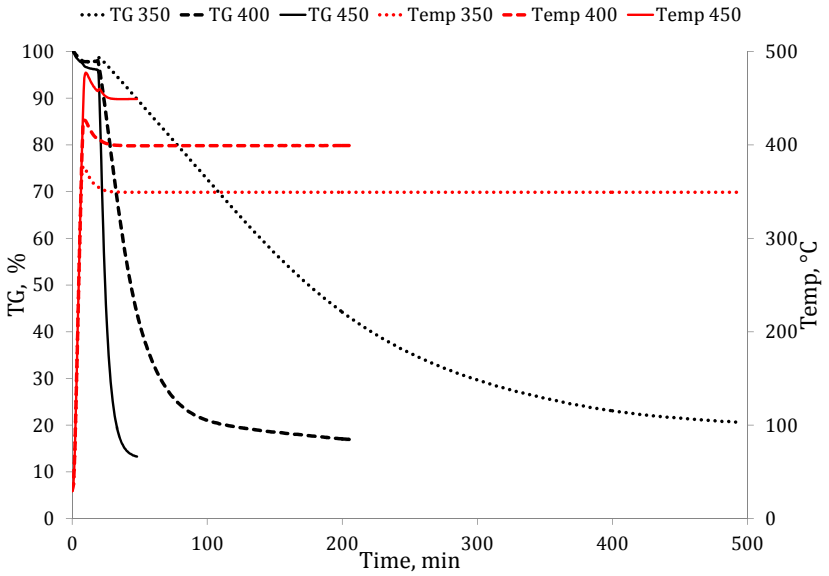

FIGURE 5.10: Relative sample mass (black lines) and temperature (red lines) during GTB-char combustion at temperatures 350°C, 400°C and 450°C; $z_{O2} = 0.21$, $z_{N2} = 0.79$

For each temperature, the experiment has been repeated at least twice. Two runs, in which the mass decay curves are almost identical, are taken for further studies. Examples of experiments repeatability for two chosen temperatures are presented in Figures 5.11 and 5.12. Black lines indicate the relative mass of char normalized to ash free basis (TG_C). Blue lines present the relative combustion rate of char calculated on the ash free basis (DTG_C). Results, for both runs overlap each other, thus a satisfactory repeatability has been achieved.

The zero time in Figures 5.11 and 5.12 corresponds to the initialization of the oxidizer gas flow. The time delay of balance response to the flow initialization is equal to circa 20 s for 850°C. The char conversion rate recalculated to ash free basis DTG_C is initially slightly increasing. After some time, a rapid DTG_C increase is observed.

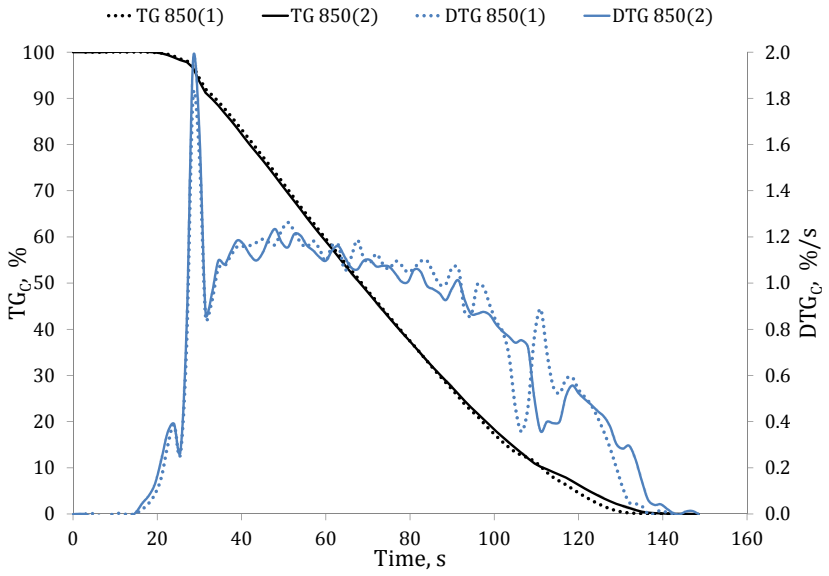

FIGURE 5.11: Relative mass of char combustibles (black lines) and conversion rate of char (blue lines) during GTB-char combustion at 850°C temperature; $z_{O2} = 0.21$, $z_{N2} = 0.79$

Figures 5.13 and 5.14 are produced to summarize the results. Figure 5.13 shows results of TG_C and DTG_C plotted against the combustion time for temperatures, in which the overall combustion rate is (theoretically) controlled by diffusion. The zero time, similarly to Figures 5.11 and 5.12, corresponds to oxygen flow initialization. For each temperature, due to gas transport line length, the delay of combustion is present. The lower the final temperature, the longer is the delay. This behavior can be explained by the lower gas densities at higher temperatures. Due to that the gas mixture flows with higher velocity in furnace column in comparison to lower temperatures. When sufficient oxygen concentration is present at the sample, the ignition of fuel occurs. This is characterized by the strong peak of relative char combustion rate (blue lines). Later, a quick conversion rate decrease has been observed, which presumably can be explained by the significant oxygen concentration drop near the sample surface. After that time

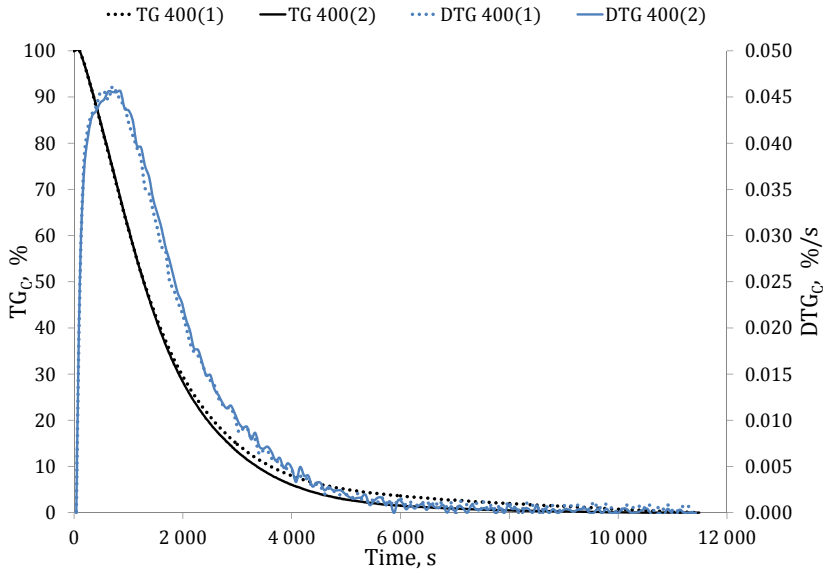

FIGURE 5.12: Relative mass of char combustibles (black lines) and conversion rate of char (blue lines) during GTB-char combustion at 400°C temperature; $z_{O2} = 0.21$, $z_{N2} = 0.79$

a stable combustion is observed. The char conversion rate is, from that instance onwards, gradually decreasing. Only slightly higher conversion rates are found for the higher temperatures. The combustion time for the highest temperature of 950°C is equal to approximately 127 *s*, for 750°C is 159 *s*, while for 600°C is circa 200 *s*.

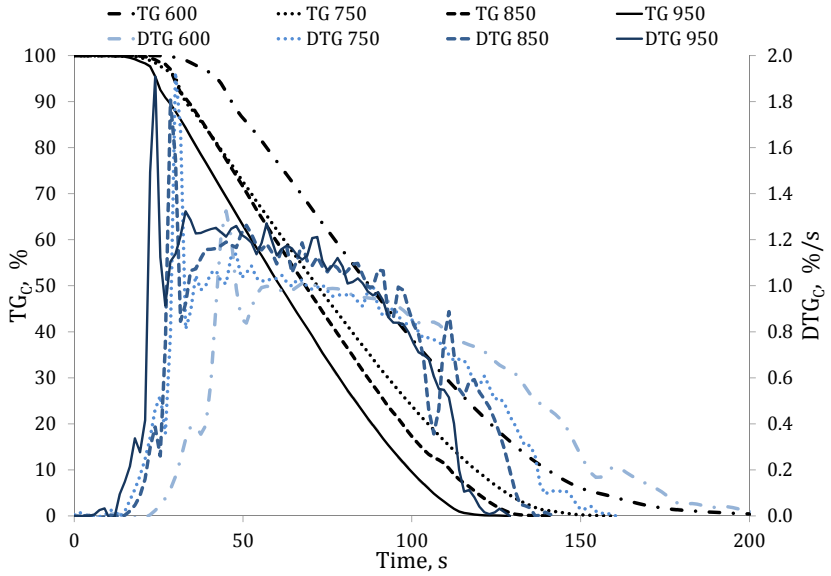

FIGURE 5.13: Relative mass of char combustibles (black lines) and conversion rate of char (blue lines) obtained during GTB-char combustion in 600°C-950° temperature range; $z_{O2} = 0.21$, $z_{N2} = 0.79$

Differences in combustion times and relative char combustion rates have been observed for lower temperatures (350°C-450°C), despite the fact that the temperature difference for each

measurement is only 50 K apart (Fig. 5.14). The maximum obtained DTG_C for the 450°C case is approximately 30 times greater than for 350°C. Such a substantial difference indicates the crucial significance of the temperature in the kinetic controlled region. According to Arrhenius equation (5.1), this dependence should be exponential. The char combustion time observed in the TGA experiments is as long as 427 *min* at 350°C, while for 400°C and 450°C temperatures is around 190 *min* and 29 *min*, respectively.

$$k_{int} = A_{int} \cdot exp(-E_{a\ int}/(R \cdot T)) \tag{5.1}$$

where:

k_{int}	- intrinsic kinetics constant,	m/s
A_{int}	- pre-exponential factor for intrinsic kinetics,	m/s
$E_{a\ int}$	- activation energy,	$kJ/kmol$
R	- universal gas constant,	$kJ/(kmol \cdot K)$
T	- particles temperature,	K

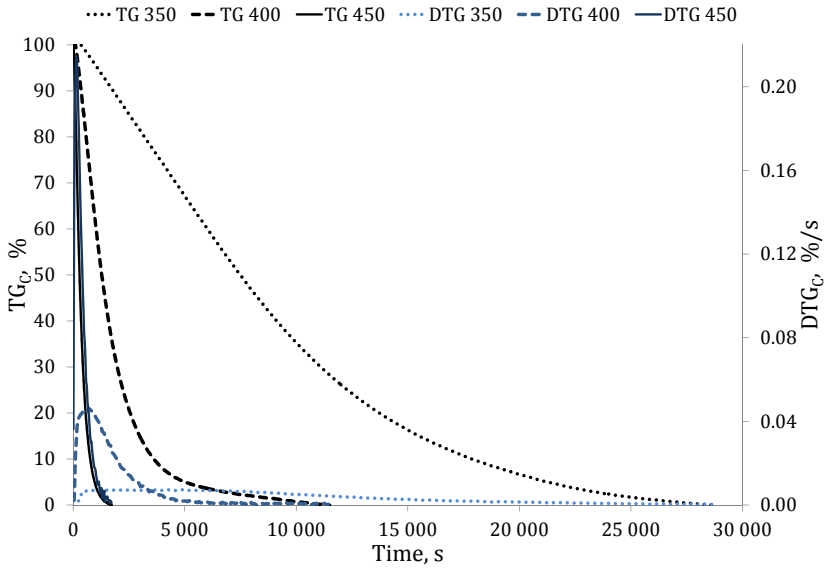

FIGURE 5.14: Relative mass of char combustibles (black lines) and conversion rate of char (blue lines) obtained during GTB-char combustion in 350°C-450°C temperature range; $z_{O2} = 0.21$, $z_{N2} = 0.79$

5.4.3 TGA-char combustion in TGA

Figures 5.15 and 5.16 show relative mass and temperature of a TGA-char sample, plotted against time of combustion. Almost no volatiles have been found in samples during the steady heating, what is in contrary with the observations made in previous experiments with GTB-char (Figures 5.9 and 5.10). Even if the final temperature is 950°C the change of mass due to moisture and volatiles release is not larger than 6.5%. The combustion is initialized, when

the oxygen reaches the sample dispersed on the crucible bottom. Similarly to GTB-char combustion, the linear trend of TG with time is observed for TGA-char, for the temperature range 600°C-950°C. The lower temperature range does not include the lowest studied for GTB-char 350°C temperature. Since very long combustion times at such a low temperature (more than 12 hours) have been observed, it has not been possible to maintain steady oxygen flow over such a long period. It has been decided to preform additional experiments at 500°C, in order to get three measurements points in the kinetic regime. The char ignition has been observed for TGA-char combustion in higher temperature range (600°C-950°C) similarly to GTB-char combustion. Due to that the temperature increase of the sample has been observed (Fig. 5.15).

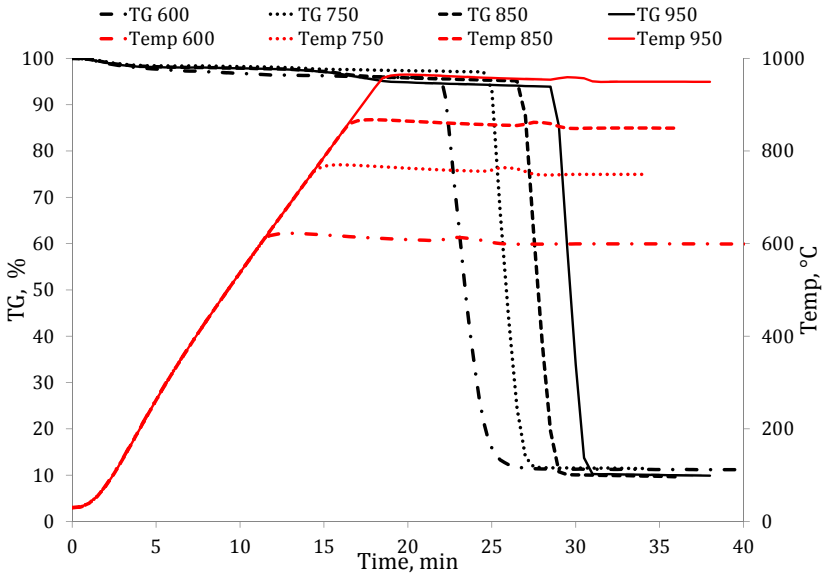

FIGURE 5.15: Relative sample mass (black lines) and temperature (red lines) during TGA-char combustion at temperatures of 600°C, 750°C, 850°C and 950°C; $z_{O2} = 0.21$, $z_{N2} = 0.79$

For each of the investigated temperatures the TGA run has been carried out twice to ensure reliability. An example of repeatability for 400°C is presented in Figure 5.17. The curves, which represent relative char mass (ash free basis) and relative char conversion rate recalculated to ash free basis, are in good agreement.

Similarly to the GTB-char experiments, zero time in Figures 5.18 and 5.19 corresponds to oxygen flow initialization. Thus, the delay of combustion initialization, due to gas line is apparent. No substantial differences between the relative conversion rates are found for the 750°C-950°C temperature range (Fig. 5.18). However, at 600°C the DTG_C decreases and thus the combustion time lengthening is observed in comparison to rates observed in the 750°C-950°C range. At 600°C the TGA char is combusted probably in transition regime, where kinetics and diffusion are important. Thus, char conversion rate is a convolution of both processes, because none of them is significantly quicker than the other at this temperature. The combustion time for the highest temperature is equal to approximately 150 *s* while for 600°C circa 310 *s*. Meaningful differences in combustion times have been obtained for lower temperature range of

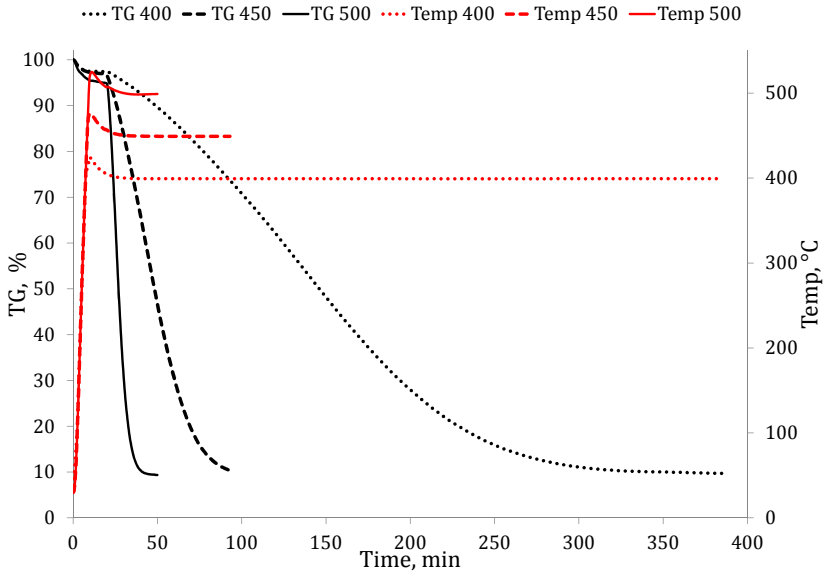

FIGURE 5.16: Relative sample mass (black lines) and temperature (red lines) during TGA-char combustion at temperatures of 400°C, 450°C and 500°C; $z_{O2} = 0.21$, $z_{N2} = 0.79$

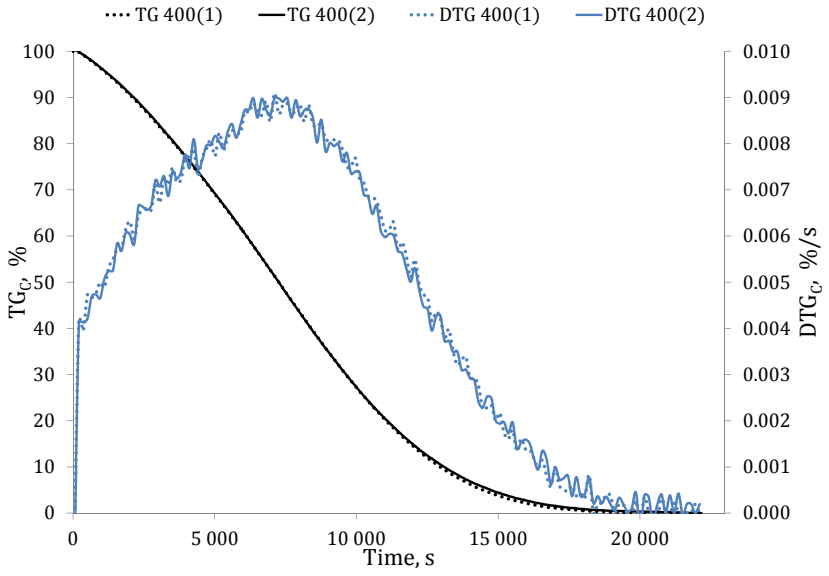

FIGURE 5.17: Relative mass of char combustibles (black lines) and char relative conversion rate recalculated to ash free basis (blue lines) during TGA-char combustion at 400°C temperature; $z_{O2} = 0.21$, $z_{N2} = 0.79$

400°C-500°C (Fig. 5.19). Differences are related to the kinetic regime of combustion, where the reaction of oxygen with carbon is much slower than the species transport. The char combustion time in TGA is even longer than 330 *min* at 400°C.

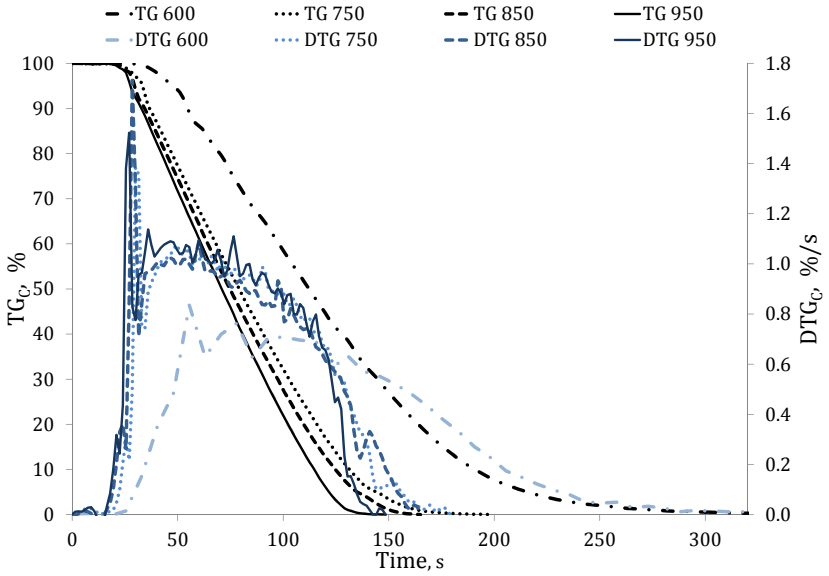

FIGURE 5.18: Relative mass of char combustibles (black lines) and conversion rate of relative mass of char combustibles (blue lines) obtained during TGA-char combustion in 600°C-950°C temperature range; $z_{O2} = 0.21$, $z_{N2} = 0.79$

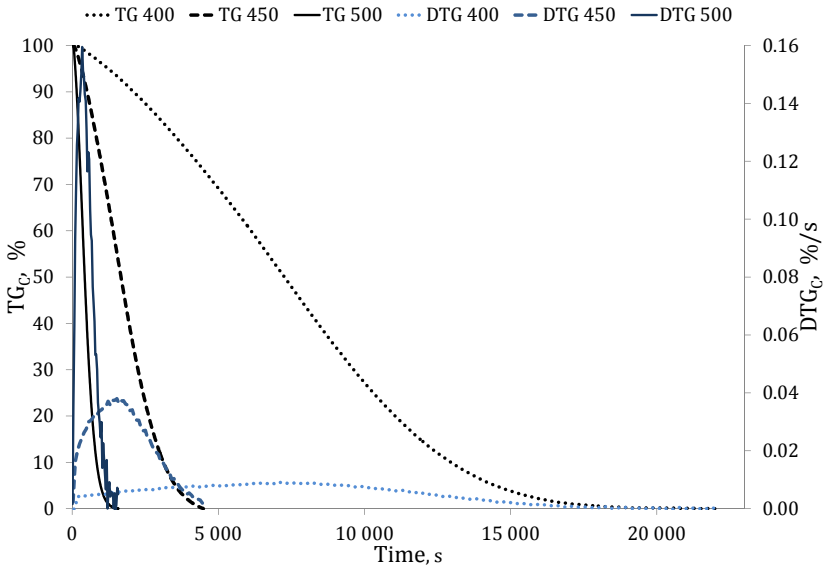

FIGURE 5.19: Relative mass of char combustibles (black lines) and conversion rate of relative mass of char combustibles (blue lines) obtained during TGA-char combustion in 400°C-500°C temperature range; $z_{O2} = 0.21$, $z_{N2} = 0.79$

5.4.4 Comparison of GTB-char and TGA-char combustion in TGA

In this paragraph a comparison of the GTB-char and TGA-char combustion experiments is being made. The TGA-char, which has been produced at low heating rates, has been found to have lower relative combustion rates (ash free basis) for each of considered temperatures, as shown in Figure 5.20. On the left axis the average conversion rate of char combustibles (DTG_C^{av}) is plotted. The DTG_C^{av} is calculated as an arithmetic average of char conversion rates (ash free basis) for the char 10% to 85% conversion, taking two runs into consideration (as shown for example in Figure 5.17) for each temperature. The GTB-char oxidation rates are marked with black triangles, while TGA-char with empty circles. At lower temperatures, each increase of temperature causes the DTG_C^{av} to increase significantly, until around 600°C temperature (Fig. 5.20). From this temperature onwards the conversion rate increases but with a lower rate. The combustion rate slow down is due to the oxygen diffusion limitation to the sample surface and in the sample itself. However, the diffusion effect does not explain the differences in average relative conversion rates of GTB-char and TGA-char. It has been found that for lower temperatures (400°C and 450°C) the GTB-char burns four times faster than the TGA-char in the kinetic controlled region (blue squares). This difference is visible when relative char conversion rates are plotted against time of combustion (Fig. 5.21). Solid lines indicate here the GTB-char conversion, while dotted lines TGA-char conversion. The TGA-char combustion time is about three times longer. According to literature [80, 85, 86], the char thermal annealing, may appear when the coal is hold longer in high temperatures. The thermal annealing is the process when char losses some hydrogen and oxygen, which causes coalescence of the aromatic rings that are comprised in the char material, and which increases of structural order in the fuel [80]. Several papers reported a decrease in char reactivity when char was produced in higher temperatures [80, 86, 87], had longer residence time in higher temperatures [80, 83, 85, 86, 88] and its devolatilization was performed at low heating rate [80], what is also associated with longer residence time at high temperatures. The low heating rate, in combination with half an hour of residence time at 750°C during devolatilization (Section 5.3), has caused the thermal annealing of the TGA-char. Moreover, the relatively young coal from "Janina" mine, can be influenced by this process more intensively in comparison with higher rank coals or anthracites, because its original structure is less organized and thus has higher potential for its rearrangement [86]. To examine the impact of devolatilization process on the char structure the mercury porosimetry analysis has been performed (see Section 6.3).

At high temperatures (750°C-950°C) the combustion rates of two considered chars, do not differ significantly (Fig. 5.20). The GTB-char to TGA-char conversion rates ratio of 1.1 has been attained, which indicates that oxygen diffusion to the sample surface is a rate controlling mechanism. Figure 5.22 shows small differences in TG_C and DTG_C during entire TGA-char and GTB-char combustion process at 750°C. In contrary to these results, the data obtained at 600°C

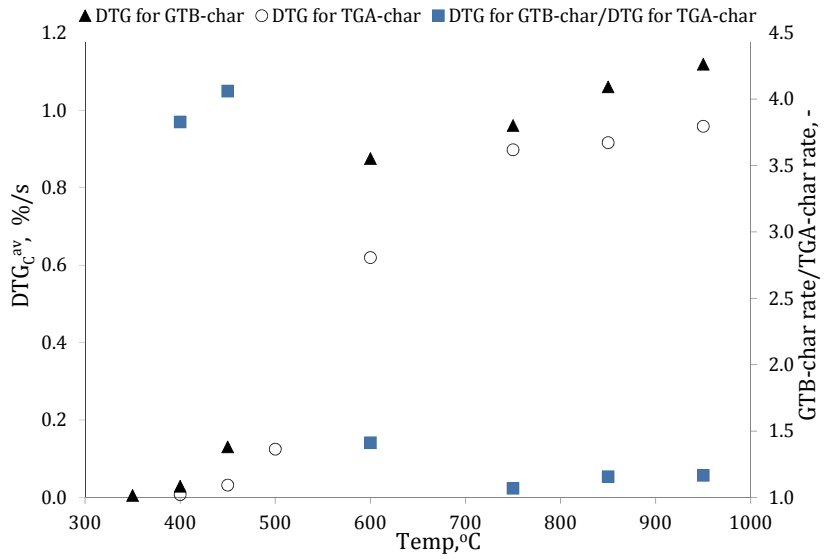

FIGURE 5.20: Average relative conversion rate of char combustibles and the relative conversion rate ratio of GTB-char and TGA-char plotted against temperature; $z_{O2} = 0.21$, $z_{N2} = 0.79$

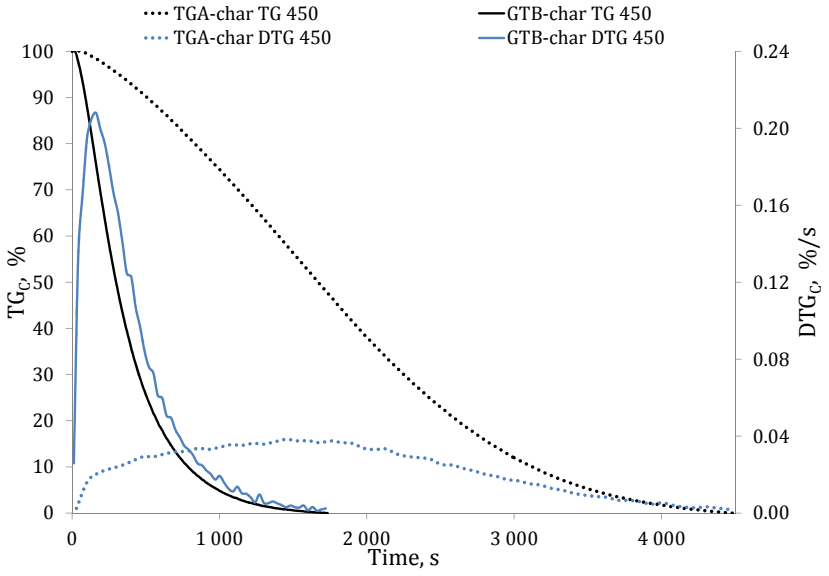

FIGURE 5.21: The comparison of TGA-char and GTB-char combustion in TGA at 450°C; Black lines indicate relative mass of char combustibles and blue lines show the relative conversion rates of GTB-char and TGA-char; $z_{O2} = 0.21$, $z_{N2} = 0.79$

is shown in Figure 5.23. The difference in the relative mass loss is easily noticeable and the combustion time difference for TGA-char and GTB-char is around 100 *s*. The ratio of the char conversion rates is around 1.4, which indicates that probably these experiments are not any more purely controlled by gas diffusion to the sample surface. The combustion, at least for TGA-char, takes place in the transition regime, which is controlled by both kinetics and pore diffusion.

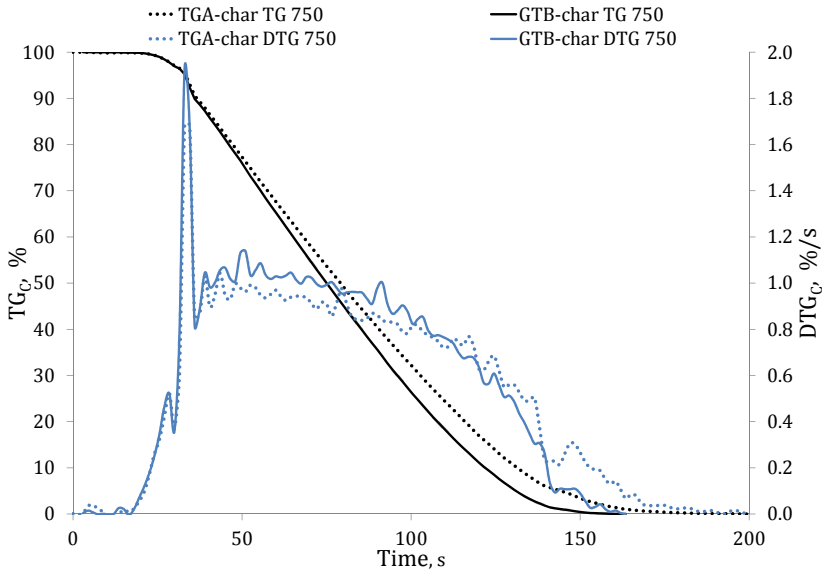

FIGURE 5.22: The comparison of TGA-char and GTB-char combustion in TGA at 750°C; Black lines indicate relative mass of char combustibles and blue lines present the relative conversion rate of GTB-char and TGA-char; $z_{O2} = 0.21$, $z_{N2} = 0.79$

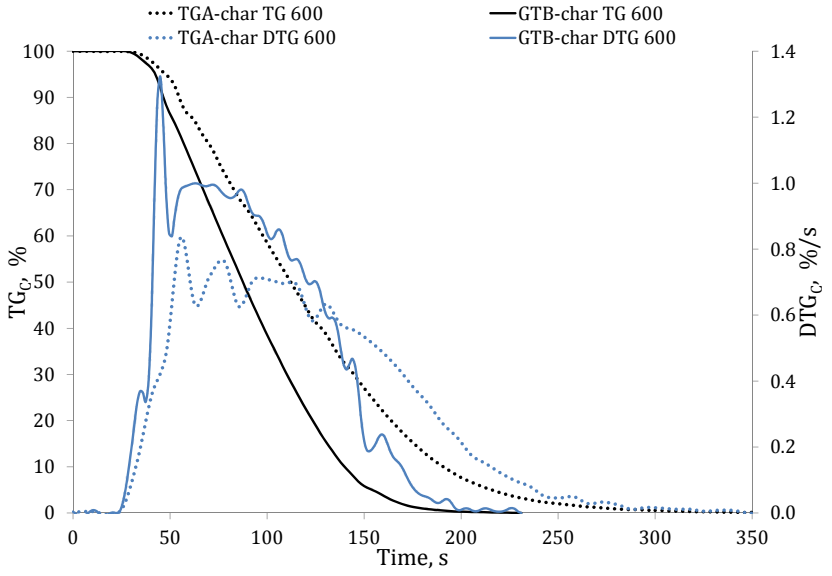

FIGURE 5.23: The comparison of TGA-char and GTB-char combustion in TGA at 600°C; Black lines indicate relative mass of char combustibles and blue lines present the relative conversion rate of GTB-char and TGA-char; $z_{O2} = 0.21$, $z_{N2} = 0.79$

The differences in combustion rates between TGA-char and GTB-char, in kinetic controlled regime, show clearly that the thermal history of char is one of the most important parameters influencing combustion rates. Therefore, attention is needed during the char preparation procedure. The devolatilization conditions should be as much as possible similar to the conditions found in a real boiler, thus very high heating rates and not too long residence times are recommended. It would be interesting to perform coal devolatilization in a fluidized bed boiler and to redo TGA combustion experiments with such a char, which probably would have different reactivity to GTB-char that has been produced in the test rig, where such a fast heating rate cannot be attained.

5.5 Char gasification in TGA

The aim of the char gasification study in N_2/CO_2 atmosphere is determination of the gasification rates at various temperatures.

5.5.1 Measurement procedures

The preliminary TGA studies and the literature study allow for the choice of the temperature of basic gasification experiments in N_2/CO_2 atmosphere. It has been found that 750°C temperature is too low for keeping a steady gas flow for more than eighteen hours. According to the literature, the rate transition regime between kinetically controlled and diffusion/kinetic controlled is in the range of 900°C to 1100°C [73, 77, 83, 89]. However, the regime is depended also on the partial pressure of CO_2 and particle size. Thus, using <0.25 mm particles, the kinetic controlled gasification region is supposed to occur at temperature below 950°C. Three temperature points have been chosen for gasification rates determination; those are: 800°C, 850°C and 950°C. The partial pressure of carbon dioxide, similarly to the char combustion case, is set to be 0.21 *bar*, therefore, 26.3 ml/min volumetric flow rate has been used. The fuel, which has been used in the gasification experiments is the GTB-char. The following temperature program has been applied:

- Standby program to achieve 30°C temperature of the sample (in N_2);
- Sample heating up with 50 K/min heating rate to required temperature (in N_2);
- Ten minutes isotheral operation at required temperature for temperature stabilization (in N_2);
- Isothermal operation in N_2/CO_2 atmosphere.

The experimental procedure is firstly performed at least two times for each temperature to obtain reliable calibration lines. In case if two calibration lines are similar, the one line has been chosen for test with char sample. For each gasification experiments the sample of about 8 *mg* is used. Gasification tests have been performed at lest two times for each temperature.

5.5.2 GTB-char gasification in TGA

The raw data obtained for each of the considered temperature is shown in Figure 5.24. Red lines indicate the sample temperature, while black lines the sample mass normalized to the initial sample mass. A char gasification has been found to be very sensitive to the gasification temperature, which is apparent in the change of gasification time.

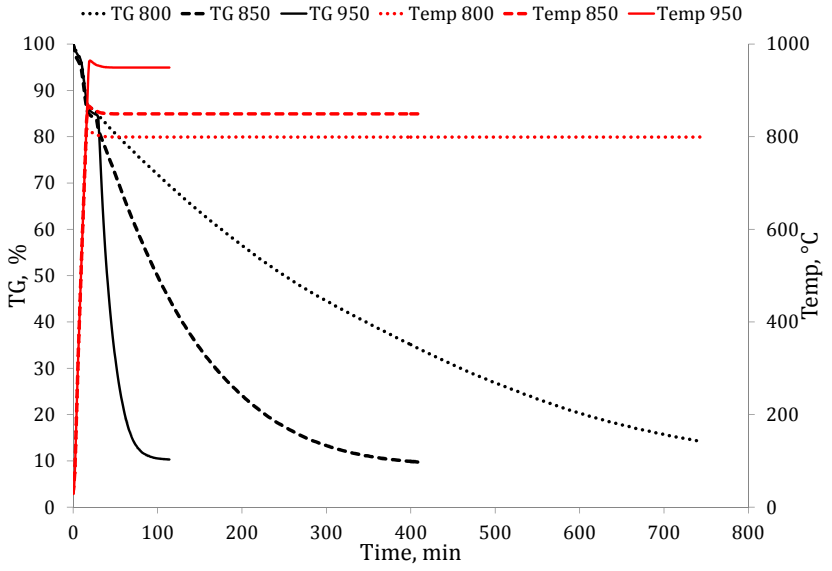

FIGURE 5.24: Relative sample mass (black lines) and temperature (red lines) during GTB-char gasification at 800°C, 850°C and 950°C temperatures; $z_{CO2} = 0.21$, $z_{N2} = 0.79$

An example of measurements repeatability is shown in Figure 5.25 for 850°C. Blue lines, which indicate conversion rate of char combustibles (DTG_C) for the two measurements, are almost overlapping each other. Similar repeatability has been obtained for the other two temperatures considered.

Figure 5.26 shows the observed gasification rates for three temperatures considered. For each temperature the CO_2-gasification progresses much faster at the beginning of the process and later decreases asymptotically. The gasification time is roughly equal to 6.5 hours for 8 *mg* char sample at 850°C temperature and 85 minutes at 950°C temperature. In fluidized bed boilers, because of the high heat transfer rates, the char particle temperature do not exceeds substantially the bed temperature [48, 56]. Therefore, comparing gasification times with combustion times

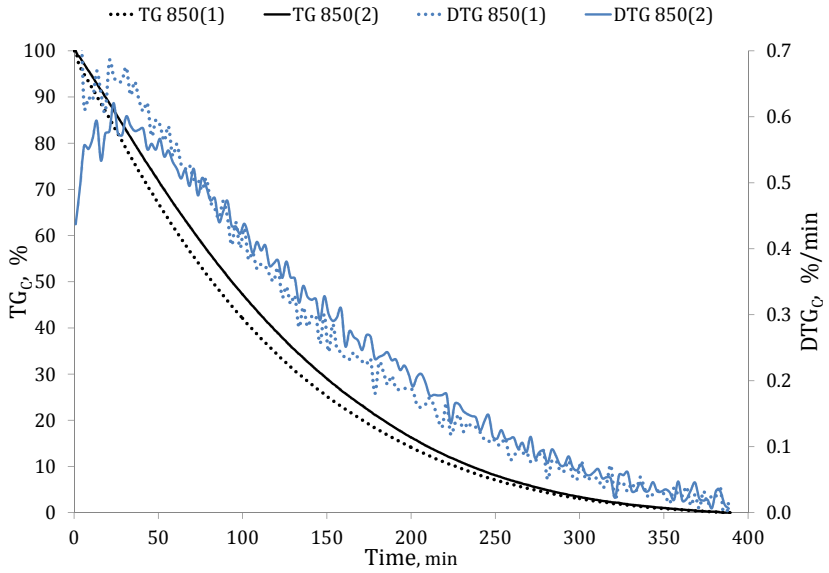

FIGURE 5.25: Relative mass of char combustibles (black lines) and conversion rate of relative mass of char combustibles (blue lines) during GTB-char gasification at 850°C temperature; $z_{CO2} = 0.21$, $z_{N2} = 0.79$

(see Section 5.4) at 850°C and 950°C temperatures, it can be seen that the CO_2-char reactions proceeds much slower than oxygen-char reactions.

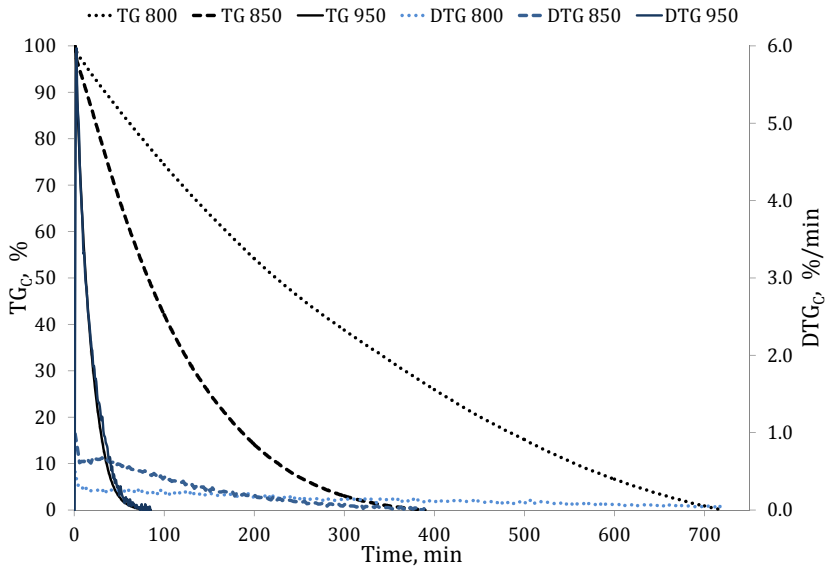

FIGURE 5.26: Relative mass of char combustibles (black lines) and conversion rate of char relative mass of combustibles (blue lines) obtained during GTB-char gasification in 800°C-950°C temperature range; $z_{CO2} = 0.21$, $z_{N2} = 0.79$

The average gasification rate (recalculated to ash free basis) has been evaluated for char burnout between 10% and 85%. Figure 5.27 shows the arithmetic average of these values calculated from the two measurements for each temperatures and are marked with black triangles.

It has been found that the dependency of the average gasification rate (DTG_C^{av}) with the temperature is exponential, what confirms, the assumption for the kinetic regime at this temperature range. Empty circles (Fig. 5.27) show the relative deviation of gasification rate results from the their average value. This quantity is the largest at the highest 950°C temperature and is 5.2%.

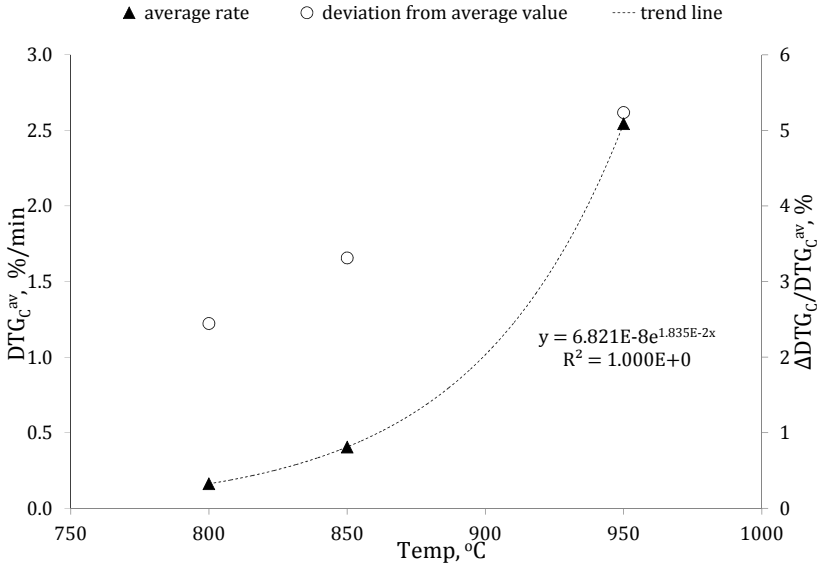

FIGURE 5.27: The average char gasification rate and rate deviation from average values plotted for 800°C, 850°C and 950°C temperatures; $z_{CO2} = 0.21$, $z_{N2} = 0.79$

Chapter 6

Arrhenius constants determination

The following chapter presents the procedure for determination of intrinsic rates of char combustion with O_2 and gasification with CO_2 using the isothermal experiments carried out in the TGA, presented in Chapter 5. In addition, the results obtained by the mercury porosimeter are presented here. At the end of this chapter, the kinetics results are presented and compared with values found in the literature.

6.1 Procedure

In order to determine intrinsic rates from TGA data, an appropriate off-set of oxidation has to be chosen. Two factors have to be taken into consideration. The first factor is a time needed for the reacting mixture to reach crucible after initialization of the flow. This time varies with the experiment temperature, which is varied in the range of 350°C - 950°C. Because the mass flow rate of gas has been kept constant, independently of the temperature, the time delay between oxygen (or carbon dioxide) flow initialization and the begin of heterogeneous reaction of fuel with oxidizer is much longer at 350°C than at 950°C. This is associated with different gas densities at different temperatures. The second factor, which has to be taken into account is the possibility of improper oxygen or carbon dioxide content in the mixture at the beginning of char oxidation. This situation can occur due to instabilities in the oxygen/carbon dioxide flow rate just after the initialization of gas flow. This can cause that the initial gas mixture does not have the required composition. Taking both factors into consideration, the char oxidation rates have been determined considering the 10% - 85% char conversion interval (see Fig. 6.1). Typically only a part of the mass loss curve is used for determination of the oxidation/gasification rates. For instance in some works [76, 79, 90] 50% of char burnout was used, while Karlstrom et al. [91] used 75% of char burnout. The sample mass at time, when the oxygen or carbon dioxide flow is initialized, indicates the initial sample mass taken for rates calculations. Char burnout is

calculated as:

$$X = 1 - m_C/m_{C0} \tag{6.1}$$

where:

X	- char burnout,	–
m_C	- current mass of the sample (ash free basis),	mg
m_{C0}	- initial mass of the sample (ash free basis)	mg

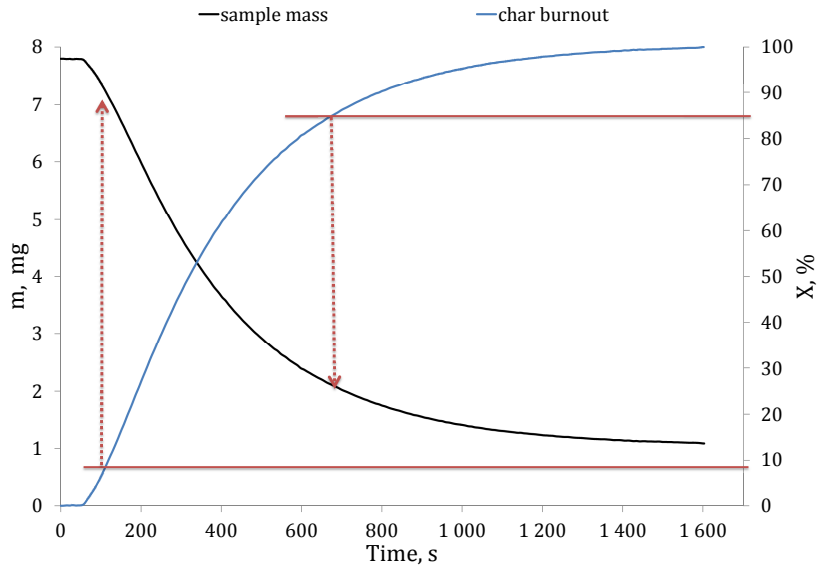

FIGURE 6.1: An example of a raw TGA data used for kinetic constants calculation obtained during GTB-char combustion at 450°C; Red arrows limit the mass range, which was used for Arrhenius constants determination

6.2 Equations

6.2.1 Char oxidation with oxygen

Assuming that char consists of only ash and carbon, char oxidation can be described by the following stoichiometric equation:

$$C + \gamma O_2 \Rightarrow (2\gamma - 1)CO_2 + (2 - 2\gamma)CO \tag{6.2}$$

where, carbon is oxidized to both carbon dioxide and carbon monoxide, see Arthur [92]. The CO/CO_2 ratio depends on the temperature and oxygen concentration; for oxygen mole fractions not larger than around 21%, the CO/CO_2 ratio is [92]:

$$CO/CO_2 = 2512 \cdot exp(-6244/T_p) \tag{6.3}$$

To calculate stoichiometric coefficient of global reaction (γ) for a specific temperature, the following dependence is used:

$$\gamma = (1 + 0.5 \cdot (CO/CO_2))/(1 + (CO/CO_2)) \tag{6.4}$$

Figure 6.2 shows CO/CO_2 ratio and γ dependence with temperature. More CO_2 is produced at temperatures lower than 800 K. At temperatures approximately 1100 K the CO/CO_2 ratio is circa 8.5, which means that around eight times more carbon monoxide is produced than carbon dioxide. At temperatures around 1400 K, which have been observed during GTB combustion experiments (see Section 4.4), the reaction 6.2 proceeds to form almost only CO. Stoichiometric coefficient of char oxidation reaction with O_2 changes between one, when only carbon dioxide is produced and 0.5 at sufficiently high temperatures.

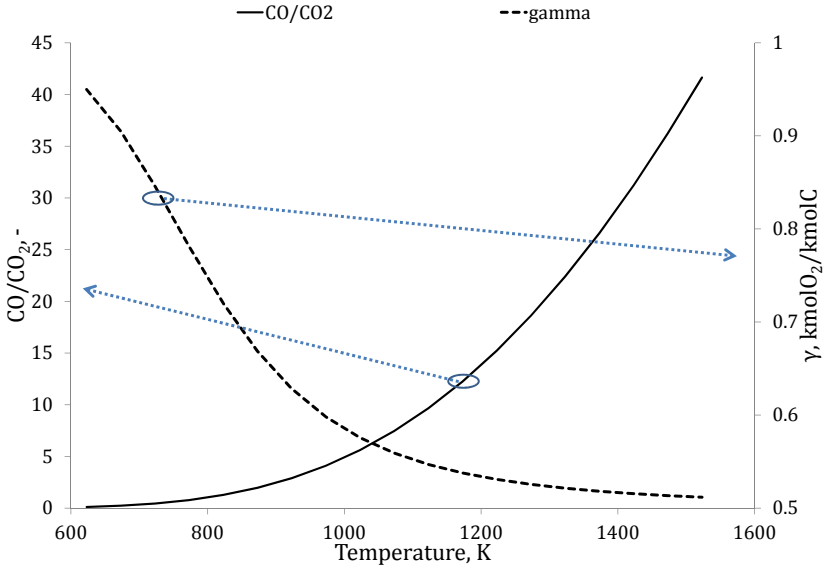

FIGURE 6.2: CO/CO_2 ratio (black solid line) and stoichiometric coefficient (black dashed line) for char oxidation with O_2 plotted against temperature

However, in the literature, the char is sometimes assumed to be burned globally to CO_2 in the particle or within its boundary layer [17, 31, 60, 67, 82, 93]. Smith [31], Basu [17] and Chen and Kojima [93] made this assumption for larger particles. The explanation was that even if CO is formed due to reaction with carbon, carbon monoxide oxidation to CO_2 takes place mainly inside the particle and on the surface of the particle, thus the energy gain is similar to that found for carbon oxidation to CO_2. Consequently, the char oxidation product, which leaves the particle boundary layer, can be assumed to be CO_2 if combustion of larger particles (with diameter > 1 *mm*) is performed at temperatures found in FB boilers. Therefore, the Arrhenius constants calculation, in the present work, has been also performed according to the global reaction:

$$C + O_2 \Rightarrow CO_2 \tag{6.5}$$

Nevertheless, the major primary product of char oxidation with O_2 at temperatures, which are found in GTB experiments or in pulverized coal boilers, is CO (see Figure 6.2), thus, kinetic constants have also been evaluated according to reaction:

$$C + 0.5O_2 \Rightarrow CO \tag{6.6}$$

According to the literature [82, 91, 93–95] the reaction of char with oxygen can be assumed to be first order. Due to the requirement of Ansys Fluent software to express the carbon source term in $kg/(m^3 s)$ (see Chapter 8), Equation 6.7 has been formulated, which combines the intrinsic reactivity, internal surface area development and oxygen concentration.

$$dm/d\tau = -V_{sample} \cdot \epsilon \cdot 1/\gamma \cdot M_C \cdot k_{int} \cdot S_V \cdot C_{O2} \tag{6.7}$$

where:

m	- char mass,	kg
τ	- time of combustion,	s
V_{sample}	- volume of the sample,	m^3
ϵ	- char porosity at time τ,	m_g^3/m^3
γ	- stoichiometric coefficient of global reaction of carbon oxidation with O_2,	$kmolO_2/kmolC$
M_C	- molar mass of carbon,	$kgC/kmolC$
k_{int}	- intrinsic reaction rate constant (see Eq. 5.1),	m/s
S_V	- char volumetric internal surface area at time τ,	m^2/m^3
C_{O2}	- molar concentration of oxygen,	$kmolO_2/m_g^3$

Sample volume (V_{sample}) can be calculated having char apparent density and its mass according to Equation 6.8, while char porosity change can be described as a function of apparent density, taking the assumption, that the particles volume remain constant (Equation 6.9).

$$V_{sample} = m_0/\rho_{app0} \tag{6.8}$$

where:

ρ_{app0}	- initial apparent density of char at $\tau = 0s$,	kg/m^3

$$\epsilon = 1 - \rho_{app}/\rho_{true} \tag{6.9}$$

where:

ρ_{app}	- apparent density of char at τ,	kg/m^3
ρ_{true}	- true char density,	kg/m^3_{solid}

The true solid density is calculated taking the initial char porosity and initial apparent density of char according to Equation 6.10.

$$\rho_{true} = \rho_{app0}/(1 - \epsilon_0) \tag{6.10}$$

Char specific (volumetric) internal surface area is changing during oxidation. One of the most popular model, which presents the variation of an internal surface area is the Random Pore Model, developed by Bhatia and Perlmutter [96]. According to this model the internal surface development is a function of char burnout and is depended on pore structural parameter (ψ). The internal surface area is then described using Equation 6.11 [97].

$$S_V = S_{V0} \cdot (1 - X) \cdot (1 - \psi \cdot ln(1 - X))^{0.5} \tag{6.11}$$

where:

S_{V0}	- initial char volumetric internal surface area at $\tau = 0$,	m^2/m^3
ψ	- pore structural parameter,	–

The pore structural parameter can be calculated according to [96] using Equation 6.12.

$$\psi = 4 \cdot \pi \cdot L_V \cdot (1 - \epsilon_0)/S_{V0}^2 \tag{6.12}$$

where:

L_V	- volumetric pore length,	m/m^3
ϵ_0	- initial char porosity,	m_g^3/m^3

Volumetric pore length, assuming the cylindrical pore shape, can be calculated from the total intrusion volume of mercury per gram of char (V_{pore}) and from initial average pore diameter ($d_{pore\ av0}$) according to Equation 6.13 [98].

$$L_V = 4 \cdot V_{pore} \cdot \rho_{app0}/(d_{pore\ av0}^2 \cdot \pi) \tag{6.13}$$

6.2.2 Char gasification with carbon dioxide

The Boudouard reaction is assumed for char gasification:

$$C + CO_2 \Rightarrow 2CO \tag{6.14}$$

According to Batchelder et al. [94], this reaction can be assumed to be first order, when the temperature is in the range of $900 - 1060°C$. Thus, the equation for volumetric conversion rate

of char (Equation 6.7) has to be only slightly modified to yield:

$$dm/d\tau = -V_{sample} \cdot \epsilon \cdot 1/\gamma_{CO2} \cdot M_C \cdot k_{int} \cdot S_V \cdot C_{CO2} \tag{6.15}$$

where:

γ_{CO2}	- stoichiometric coefficient of Boudouard reaction of carbon oxidation with CO_2,	$kmolCO_2/kmolC$
C_{CO2}	- molar concentration of carbon dioxide,	$kmolCO_2/m_g^3$

Other parameters, which are required for intrinsic kinetics of char-CO_2 reaction, were calculated from equations 6.8 to 6.13.

6.3 Determination of char physical parameters

In order to obtain initial apparent char density (ρ_{app0}), initial char porosity (ϵ_0), initial internal surface area (S_{V0}), total mercury intrusion volume of pores (V_{pore}) and initial average pore diameter ($d_{pore\ av0}$), which are necessary in calculations of intrinsic kinetics, the experiments have been performed using the mercury porosimeter. Two char types GTB-char and TGA-char have been examined.

6.3.1 Mercury porosimetry

The mercury porosimetry is a technique often used for determination of porosity and a pore size distribution in a porous material. The technique allows also for determination of apparent and skeletal density as well as specific internal surface area, when a pore model is considered. The basic information, which is obtained during the porosimetry, is the volume of the mercury intruded into or extruded from the material pores with indication of the absolute pressure of the system [99]. Mercury as a non-wetting liquid has a bigger surface energy in comparison to solid energy, which results in a contact angle between solid and liquid that is greater than 90° [98]. For mercury, the angle is in the range of $130° - 150°$ for most of the solid materials [100]. According to Washburn [98], pores diameter, in which the mercury can intrude, is inversely proportional to the pressure (Equation 6.16). Therefore, increasing the pressure results in greater use of mercury volume, which penetrates smaller pores.

$$d_{pore} = -4 \cdot \gamma_{surf} \cdot cos\Phi/p \tag{6.16}$$

where:

d_{pore}	- pore diameter,	m
γ_{surf}	- surface tension of the liquid,	N/m

Φ	- angle of liquid contact with solid,	deg
p	- absolute pressure,	Pa

However, the mercury porosimetry does not allow for the smallest pores (micropores) penetration of < 3 nm in diameter. For determination of parameters for such small pores, a gas adsorption technique has to be used. Usually, the nitrogen [44, 83, 85, 101, 102] or carbon dioxide [83, 102, 103] are used. Generally, the gas adsorption is usually used for specific surface area determination, since gas penetrates also micropores. Typically, the porosity and density of porous material are determined by mercury porosimetry [44, 101–103], since the direct measurement of sample and pores volume is inherent in that technique. In this work only the mercury porosimetry has been used. The author is aware of the possible inaccuracies in determined specific surface area using the mercury porosimetry. The probable underestimation of this parameter is somehow hidden in the pre-exponential factor.

6.3.2 Measurement procedure and equipment

Measurements have been performed by Anna Pajdak at the Institute of Advanced Energy Technologies using AutoPore IV 9500 porosimeter produced by Micromeritics Instrument Corporation. This type of device allows for pore volume determination up to 3 nm, which covers all macropores and most mesopores ($2 - 50$ nm). Mercury to be intruded to such a small pores has to be pressurized significantly. The highest possible pressure, which could be obtained by this device is 414 MPa [104]. The resolution of this instrument is 0.1 μL of mercury.

Samples for porosity measurements have been prepared in two ways. Coal particles have been devolatilized in GTB as described in Section 4.3 or in TGA as described in Section 5.3. From both char types, five to eight particles are inserted into the porosimeter sample cup. Each char type has its own measurement series. The cup is subsequently inserted into the low-pressure port of porosimeter. After the program is switched on, the sample is evacuated. When a sufficiently low absolute pressure is achieved, the mercury valve opens and the cup is filled up. The pressure for delivering mercury is applied hydraulically. At each pressure step, the program waits for equilibrium and the volume of mercury used is recorded. Pressure increase causes that smaller pores are gradually filled by mercury. Since the pressure, in low-pressure port, attains the maximal value, the sample is inserted into high-pressure port, where the pressure is stepwise increased up to 414 MPa.

Since a substantial pressure is applied, deformation of the material may occur. Nevertheless, the structural deformation is likely to be caused by collapsing of the closed pores, which are not accessible at the beginning for mercury [99]. On one side this could improve the accuracy for total porosity and density determination, but on the other hand could increase the pores

volume at higher pressures and thus could influence the specific internal surface area, which is mainly depended on the smallest pores, thus the highest pressures.

6.3.3 Results and discussion

Porosimeter program determines the following parameters: total specific intrusion volume, total specific pore area, median pore diameter, apparent and skeletal densities, average pore diameter calculated as $4 \cdot V_{pore0}/S_{m0}$ and total porosity. These parameters, according to equations 6.10, 6.12, 6.13, 6.17 and 6.18 allow for calculation of char true density, volumetric pore length, pore structural parameter, initial volumetric internal surface area and pore tortuosity. Initial volumetric internal surface area can be calculated as follows:

$$S_{V0} = S_{m0} \cdot \rho_{app0} \tag{6.17}$$

where:

S_{m0} - total specific pore area, m^2/g

Pore tortuosity, which could be defined as the ratio of the real path length of gas diffusion to the straight path from hypothetical points A to B [64], can be calculated as [31]:

$$\tau_{pore} = (d_{pore\ av0} \cdot S_{V0}/4 \cdot \epsilon_0)^2 \tag{6.18}$$

Table 6.1 shows properties obtained directly from the porosimeter software, while Table 6.2 shows the calculated parameters for both GTB-char and TGA-char.

Table 6.1: Parameters obtained directly from porosimeter software

Parameter	**GTB-char**	**TGA-char**
V_{pore0}, cm^3/g	0.270	0.166
S_{m0}, m^2/g	26.8	15.8
$d_{pore\ av0}$, nm	40.2	41.9
ρ_{app0} at $\approx 1\ bar$, kg/m^3	1163	1257
ϵ_0, m_g^3/m^3	0.286	0.191
m_{sample}, g	0.459	0.762

Both the porosity as well as the internal volumetric surface area for the GTB-char are larger than for the TGA-char. The ratio of S_{V0} for GTB-char and TGA-char reaches 1.64 and it explains the difference in observed combustion rate in TGA (see Section 5.4.4). Since the apparent density and porosity of the char depend mainly on the amounts of large pores ($> 50\ nm$) and determined internal volumetric surface area depends on char mesoporosity, thus the GTB-char is characterized by larger quantities of each pore size. The results show that it is possible

Table 6.2: The calculated parameters for GTB-char and TGA-char

Parameter	GTB-char	TGA-char
$\rho_{true}, kg/m^3$	1628	1554
$L_V, m/m^3$	$2.47E+14$	$1.51E+14$
$\psi, -$	2.28	3.88
$S_{V0}, m^2/m^3$	$3.11E+7$	$1.99E+7$
$\tau_{pore}, -$	1.20	1.19

to significantly influence the char reactivity by changing coal devolatilization rate. The reactivity change between the two char types is due to modification of the specific surface area and porosity. The first parameter is responsible for surface available for reaction and the second for facilitation of gas diffusion inside a char particle.

6.4 Calculation results

On the basis of data obtained using both TGA and the mercury porosimetry, the intrinsic kinetics constant could be calculated from Equation 6.7 in case of char combustion with O_2 and Equation 6.15 if char gasification process is considered. These equations are recast so to calculate k_{int}, as:

$$k_{int} = -dm/d\tau \cdot (V_{sample} \cdot \epsilon \cdot 1/\gamma \cdot M_C \cdot S_V \cdot C_{O2})^{-1} \tag{6.19}$$

$$k_{int} = -dm/d\tau \cdot (V_{sample} \cdot \epsilon \cdot 1/\gamma_{CO2} \cdot M_C \cdot S_V \cdot C_{CO2})^{-1} \tag{6.20}$$

At each time step the left hand side of Equations 6.19 and 6.20 has been calculated, since all parameters on the right hand side are known. The subsequent step is to sum the values obtained at each time step, for char burnout between 10% and 85%. The time step size is depended on the temperature of the process; the higher the temperature, the shorter is the time step. This procedure has been performed for each measurement. Since at least two measurements have been performed for each temperature and each char, the average values for each temperature have been used in determination of Arrhenius constants. To obtain values of the pre-exponential factor and the activation energy (or activation temperature = $E_{a\ int}/R$) the Equation 5.1 is linearized:

$$ln(A_{int}) - (E_{a\ int}/R) \cdot (1/T) = ln(k_{int}) \tag{6.21}$$

Plots of $ln(k_{int})$ as function of reciprocal of sample temperature, for two temperatures regions (the first from 350 to 500°C and the second from 750 to 950°C), have been made. On the basis of three temperature points (three points are necessary for this type of calculations [105]), which lay in the intrinsic and in the diffusion region, the linear function constants have been estimated using the least square method. The slope coefficient is equal to $-Ea_{int}/R$, while $ln(A_{int})$ is the intercept with vertical axis. Figure 6.3 shows the calculated values of averaged $ln(k_{int})$ as function

of reciprocal temperature for reaction 6.5. The points connections by lines indicate four sets of results used for Arrhenius constant determination. Table 6.3 shows these values together with determination factor for char-O_2 reaction to form CO_2. The conversion rate increases strongly with the temperature, in the low temperature region. If the experiments give a straight line, the assumption for constant reaction order in considered temperature range is correct [74]. Therefore, the experimental points, which are positioned on a line, confirm the correctness of the order assumption. In the higher temperature region ($750 - 950°C$), however, the conversion rate of both char types is not depended so much on temperature (Fig. 6.3). This means that combustion is not any more controlled by the reaction rate, but by diffusion of gas. Similar trend was observed in work of Jess and Andresen [95], who found out that at lower temperatures, the influence of temperature on conversion rates was much more pronounced. Activation energies for two temperature regions were estimated in work [95]. The activation energy for higher temperature region was five times smaller in comparison to high temperature region [95]. As shown in Table 6.3, for both chars, the activation temperature for higher temperature region has much smaller values. The ratio between activation temperatures calculated for the lower temperature region and the higher temperature region reaches 8.0 and 9.8 for the GTB-char and the TGA-char, respectively. Because of the diffusion influence in high temperature region, the activation temperature is not any more the intrinsic. The pre-exponential factor has decreased as well, when turning from kinetic to diffusion region (Table 6.3). The ratio between pre-exponential factor for low temperature region and the high temperature region is as high as 5.3E+07 for GTB-char. Such a big difference is probably due to the fact, that in the high temperature region only external surface of the char particles participates in combustion, while for lower temperature region, the internal surface area, which is significantly bigger than external surface area, plays a role. The determination factor for each char and temperature region is larger than 0.98. This indicates the good accuracy of the TGA experiments performed.

Table 6.3: Arrhenius constants for GTB-char and TGA-char oxidation using $C + O_2 \Rightarrow CO_2$ reaction

Temperature range and char type	**Pre-exponential factor, m/s**	**Activation temperature, K**	**Determination factor, R^2**
$350 - 450°C$ (GTB-char)	$9.76E+03$	15970	0.9998
$400 - 500°C$ (TGA-char)	$1.64E+03$	15320	0.9991
$750 - 950°C$ (GTB-char)	$1.84E-04$	2000	0.9984
$750 - 950°C$ (TGA-char)	$1.81E-04$	1570	0.9838

Arrhenius constants have also been determined for reactions 6.2 and 6.6 for intrinsic temperature region. Table 6.4 lists these values calculated for both GTB-char and TGA-char. The activation temperature for both TGA-char and GTB-char for $C + 0.5\ O_2 \Rightarrow CO$ (see Table 6.4) and $C + O_2 \Rightarrow CO_2$ (see Table 6.3) reactions remains constant, however the pre-exponential factor is two times lower for the first reaction, which is a result of $\gamma = 0.5$. For the char

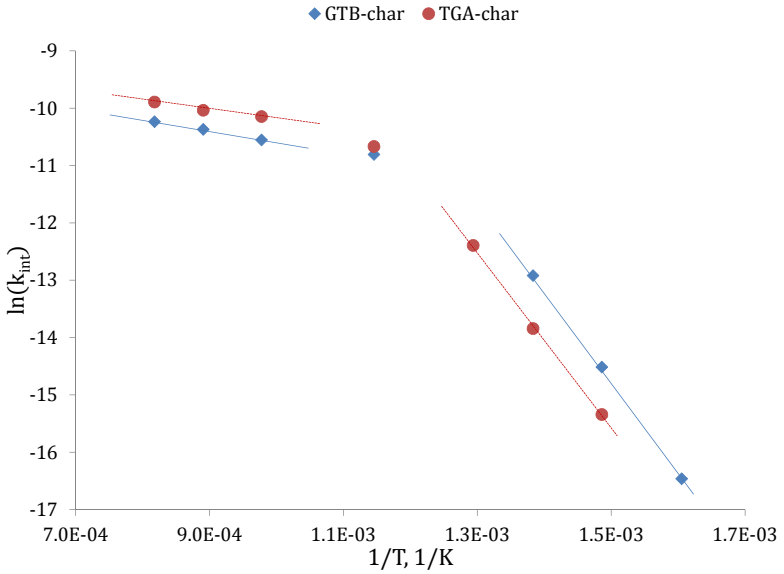

FIGURE 6.3: Arrhenius constants determination for C + O_2 ⇒ CO_2 reaction using graphical method

oxidation reaction 6.2, both the activation temperature and the pre-exponential factor are reduced in comparison to the results shown in Table 6.3.

TABLE 6.4: Arrhenius constants for GTB-char and TGA-char oxidation

Reaction	**Temperature range and char type**	**Pre-exponential factor, m/s**	**Activation temperature, K**	**Determination factor, R^2**
C + 0.5 O_2 ⇒ CO	350 – 450°C (GTB-char)	4.88E + 03	15970	0.9998
C + 0.5 O_2 ⇒ CO	400 – 500°C (TGA-char)	8.21E + 02	15320	0.9991
C + γ O_2 ⇒ (2 γ-1) CO_2 + (2-2 γ) CO	350 – 450°C (GTB-char)	4.04E + 03	15450	0.9996
C + γ O_2 ⇒ (2 γ-1) CO_2 + (2-2 γ) CO	400 – 500°C (TGA-char)	4.79E + 02	14560	0.9993

The same calculation procedure has been used for char gasification data obtained using the TGA. In this case Equation 6.15 is linearized and the average value of $ln(k_{int})$ from the two experimental runs, performed at the same temperature, is calculated. Figure 6.4 shows results plotted against reciprocal temperature. The three points are almost perfectly positioned on the line, therefore, the attained determination coefficient is almost one. The linear function constants allowed for calculation of Arrhenius parameters. The activation temperature is 26177 K, while the pre-exponential factor is equal to circa 2775 m/s.

In order to make sure that the Arrhenius constants are determined correctly, the mass loss rate of the sample is recalculated using Equation 6.7 or 6.15 and the obtained intrinsic kinetics parameters. Figures 6.5 and 6.6 show the comparison of sample mass obtained by measurements and by calculations. The calculated time of char conversion is similar to the measured, however,

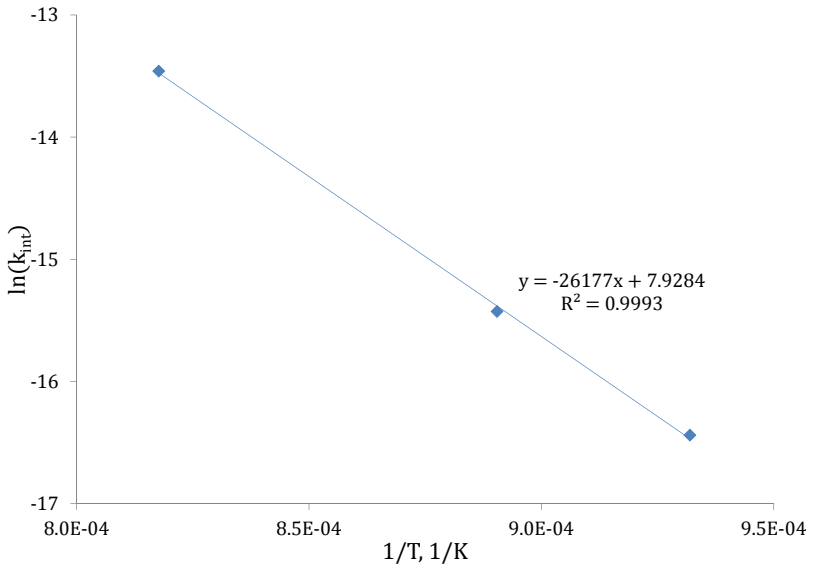

FIGURE 6.4: Arrhenius constants determination for char gasification reaction (C + CO_2 ⇒ 2 CO) using graphical method

calculated mass loss curve character, is not entirely consistent with the experimental data. The difference could be caused by underestimation of internal volumetric surface area by mercury porosimeter.

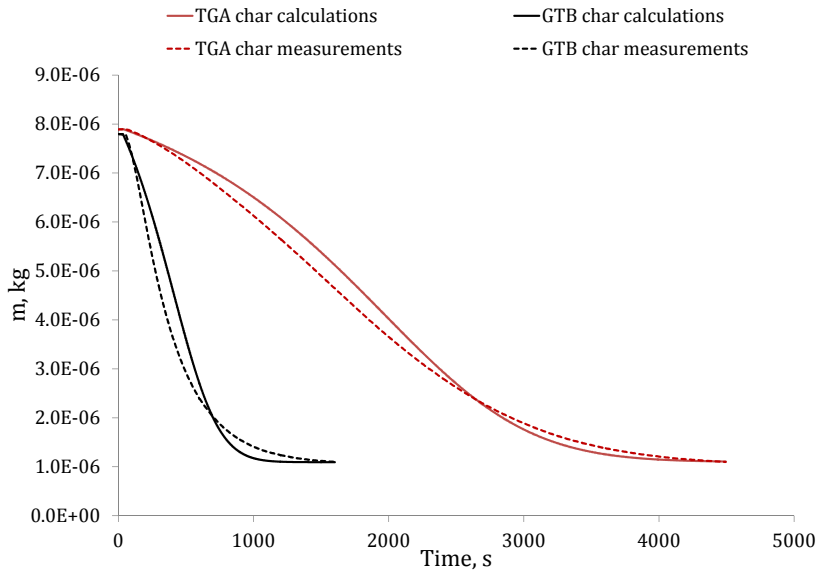

FIGURE 6.5: Validation of kinetic constants designation for 450°C; The results relate to the $C + O_2 \Rightarrow CO_2$ reaction

Table 6.5 shows literature values of activation temperature for char reactions with O_2 and CO_2. Values, which are shown in this table, vary significantly. The differences are consequences of the different experimental procedures used. In non-isothermal procedures of obtaining the kinetic constants from TGA experiments, the activation energy is depended on the heating rates

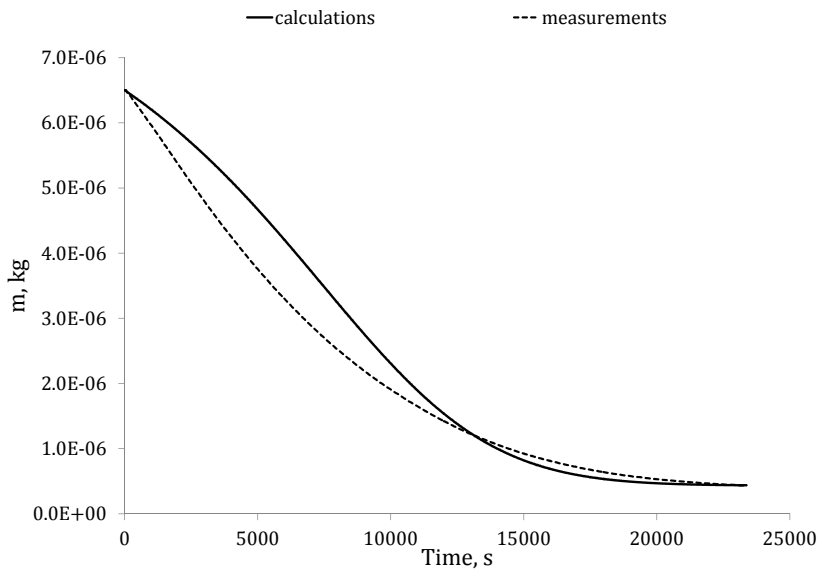

FIGURE 6.6: Validation of kinetic constants designation for char gasification in CO_2 for $850°C$ ($C + CO_2 \Rightarrow 2CO$)

and obtaining the true kinetic parameters require special mathematical procedures seldom used [74]. The proper values are sometimes chosen by comparing non-isothermal experiments with isothermal ones [105]. Mathematical methods of obtaining both the activation energy and pre-exponential factor ale seldom well described in the literature. Often experiments are performed not in intrinsic region and the obtained values of activation energy are substantially lower. The pseudo-kinetic constants are then obtained as it has been done in this work in the high temperature region (Table 6.3).

TABLE 6.5: Literature values of activation temperature

Reference	$E_{a\ int}/R$ **for char oxidation with** O_2**,** K	$E_{a\ int}/R$ **for char oxidation with** CO_2**,** K	**Description**
[67]	8000 – 10000		more reactive coal chars
[81]	4900 – 6400		non-isothermal TGA, lignite
[106]	circa 18600		non-isothermal TGA, semi-anthracite and low-volatile bituminous
[62]	16900		FB reactor, brown coal
[80]	18760 and 15600		non-isothermal TGA, commercial graphite and high volatile bituminous
[64]	15400 – 16840		TGA, bituminous coal chars
[83]	16840 – 18400	25140 – 26800	TGA
[86]	15640		Standard value
[107]	13750	26930	model assumptions
[108]	15640 – 16720		non-isothermal TGA
[105]	15560 and 16720		non-isothermal and isothermal TGA, bituminous char
[73]		16960, 19970 and 27180	Czech coke, Polish coke and graphite, first two values are apparent parameters
[109]		24740 and 12420	small reactor, Polish bituminous and lignite chars
This work	14560 - 15970	26177	isothermal TGA in intrinsic region, char produced from bituminous coal ”Janina”

Chapter 7

Zero-dimensional combustion model of a single char particle

7.1 Introduction

Char combustion rates calculations are carried out in order to deliver information, which is essential when a detailed model of combustion in a FBB is developed. The combustion rates, through Arrhenius constants and other char physical parameters, are stored in the single coal particle combustion model (SCPCM). By introducing the SCPCM into a CFD-based model the heat release/consumption rates, species production/consumption rates and mass loss rate of each particle are obtainable. A single coal particle combustion model can be either simple or complex. The simplest models are usually used in a CFD-based software for combustion in boilers, because significantly shorter time is needed for such calculations in comparison with a detailed SCPCM. This is related to the fact that thousands of particles are present in the boiler and each of them is treated separately. The most popular SCPCMs are zero-dimensional (0D) and one-dimensional (1D) models. The first model describes changes of particle parameters (temperature, char burnout, porosity, etc.) with time only, while in a 1D model, these parameters vary also with particle radius.

Because devolatilization process and volatiles combustion are much faster and have entirely different character in comparison to char combustion, devolatilization and char combustion are usually treated separately. A large number of simple devolatilization models exist in literature [18, 33, 44–47, 64, 73, 110, 111]. The devolatilization process was found to be depended on heat transfer rates inside the particle [44, 46, 73]. This means that during devolatilization a temperature gradient along particle radius exists, which was partially explained by endothermicity of devolatilization reactions and partially by insulating properties of porous char. However, some researchers claimed that the devolatilization process of particles in the range of 1 to 10 *mm*

was controlled by kinetics, because activation energy was found to play the biggest role in the process [18]. They pointed out that mass transfer had no influence on the devolatilization rate. Usually, in such models, the particle was considered to be spherical and its diameter was assumed to remain constant during devolatilization.

Since boiler efficiency is related to char burnout, the char combustion has been a subject of intensive research. Simple single char particle combustion models (SChPCM) are usually one-dimensional [47, 48, 56, 64, 67, 73, 101] and they can be classified into shrinking core models (SCM) [47, 48, 67, 93, 101] and shrinking particle models (SPM) [47, 73]. In shrinking core model, the particle diameter remains constant during char oxidation and the char apparent density decreases gradually starting from the outer layer. The reactions take place at the sharp interface between the unreacted char core and the ash layer. Shrinking core model is often used when it is expected that the ash layer affects the combustion rate through gas diffusion and heat resistance [67, 93], thus when ash content in the coal/char particle is relatively large. Here the unreacted core properties, like porosity and internal surface area do not change with time. When ash does not restrict significantly the reactants diffusion towards the unreacted core, the shrinking particle model can be used. In the SPM, the mass loss of the particle determines the diameter decrease rate. Because the particle shrinks, conditions for mass and heat transfer change considerably with time. In both one-dimensional models, the particle temperature changes with particle radius.

The 0D char combustion models are used less frequently than 1D models. Svoboda et al. [67] created SPM for smaller particles (< 1 *mm*). This model takes into account the radiative and convective heat transfer as well as external diffusion of oxygen to the particle surface. Due to simplicity, 0D models are used in the CFD-based models of fluidized bed combustion.

In this chapter, simple 0D models of single char particle combustion are presented. The purpose of creating SChPCMs is the reproduction of the measured combustion rates in the simplest possible way. Engineering Equation Solver (EES) has been used as the basic software for the SChPCMs developed.

Because the GTB experiments have been performed using different char particles, the amount of ash and its structure in each particle is different. Thus, combustion progresses differently from particle to particle (see Fig. 4.9). Therefore, both the SCM as well as the SPM have been considered in the work. The influence of oxygen diffusion resistance in the ash layer is taken into consideration in the SCM, while in the SPM, ash has been assumed to be removed immediately when the carbon, on the external layer of particle, is burned. Thus, in the SPM the ash has no influence on diffusion of reactants to the reaction surface. The constant temperature in entire particle volume is assumed in both considered models, which in the heat transfer literature is named as Lumped Capacitance Model. This means that the particle has infinitely large thermal conductivity. Reaction $C + \gamma\ O_2 \Rightarrow (2\ \gamma\text{-}1)\ CO_2 + (2\text{-}2\ \gamma)\ CO$ has been used to

describe carbon oxidation and γ is used as a parameter so that if $\gamma = 0.5$ CO is the oxidation product, when $\gamma = 1$ carbon is oxidized to CO_2. The third case, taken into account, is when γ is a function of temperature (see Equations 6.3 and 6.4). The Boudouard reaction has not been considered. However, pore and bulk gas diffusion and convective and radiative heat transfer are included in the models. Adequate Arrhenius constants and values of char physical parameters presented in Sections 6.3 and 6.4 for the GTB-char have been used.

7.2 Mathematical description of the 0D models

The shrinking particle model (SPM) and the shrinking core model (SCM) have some common assumptions, which are as follows:

- Temperature of the gas inside the particle is the same as of the solid matter and is uniform in the entire particle volume;
- Char consists of carbon, ash and gas present in pores;
- Density of carbon and ash is equal;
- All gases are treated as ideal;
- Properties of the gas mixture, which is present inside the char particle, are calculated as for air;
- Particle emissivity is constant;
- Temperature of walls and gases, which surrounds the particle, is constant;
- Oxygen diffusion is calculated without taking into consideration species, which are created during char combustion (CO_2 and/or CO);
- Parameters like: porosity, internal surface area, pore tortuosity and char apparent density are constant inside the unreacted particle core;
- Combustible gases leaving the particle are assumed to burn far away from particle surface;

7.2.1 Shrinking particle model (SPM)

The assumption in the shrinking particle model is that the particle diameter is continuously decreasing during the oxidation process. The energy conservation equation (Eq. 7.1) includes convective and radiative heat transfer and heat generation inside the particle associated

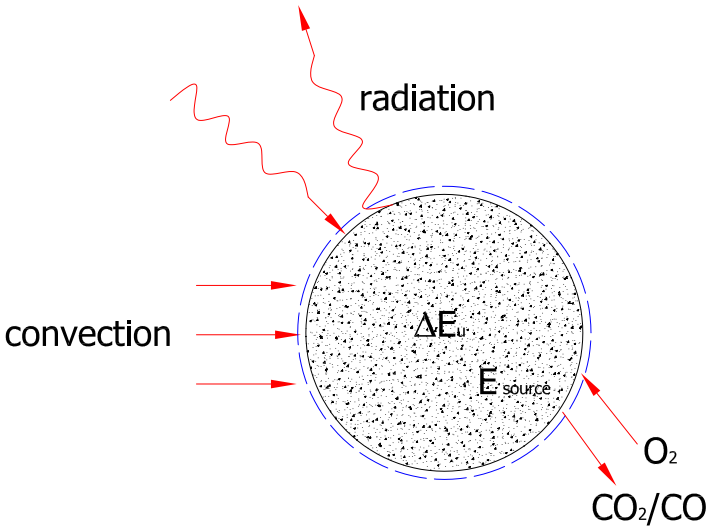

FIGURE 7.1: Diagram of energy balance of the char particle used in the SPM

with heterogeneous char oxidation reactions. Figure 7.1 shows the energy balance diagram for the SPM.

$$\begin{aligned} c_r \cdot \Delta h_r - ((h_{CO2}^{Tp} - h_{CO2}^{298.15}) \cdot (2 \cdot \gamma - 1) \cdot c_r \cdot (M_{CO2}/M_C) \\ +(h_{CO}^{Tp} - h_{CO}^{298.15}) \cdot (2 - 2 \cdot \gamma) \cdot c_r \cdot (M_{CO}/M_C) \\ -(h_{O2}^{Tb} - h_{O2}^{298.15}) \cdot c_r \cdot \gamma \cdot (M_{O2}/M_C) \\ +\alpha \cdot S_{ext} \cdot (T_p - T_b) + \epsilon_{p-pw} \cdot \sigma \cdot S_{ext} \cdot (T_p^4 - T_{wall}^4)) \\ = \frac{dT_p}{d\tau} \cdot (V_p \cdot (1 - \epsilon_0) \cdot c_{char} \cdot \rho_{true} + V_p \cdot \epsilon_0 \cdot c_{p\,air}(T_p) \cdot \rho_{air}(T_p, p)) \end{aligned} \tag{7.1}$$

where:

c_r	- char conversion rate,	kg/s
Δh_r	- specific reaction enthalpy of carbon oxidation,	kJ/kg
h_{CO2}^{Tp}	- specific enthalpy of carbon dioxide at T_p,	kJ/kg
$h_{CO2}^{298.15}$	- specific enthalpy of carbon dioxide at 298.15 K,	kJ/kg
h_{CO}^{Tp}	- specific enthalpy of carbon monoxide at T_p,	kJ/kg
$h_{CO}^{298.15}$	- specific enthalpy of carbon monoxide at 298.15 K,	kJ/kg
h_{O2}^{Tp}	- specific enthalpy of oxygen at T_p,	kJ/kg
$h_{O2}^{298.15}$	- specific enthalpy of oxygen at 298.15 K,	kJ/kg
$c_{p\,air}(T_p)$	- air specific heat capacity at constant pressure, at T_p,	$(kJ/kg \cdot K)$
M_{CO2}	- molar mass of carbon dioxide,	$kgCO_2/kmolCO_2$
M_{CO}	- molar mass of carbon monoxide,	$kgCO/kmolCO$
M_{O2}	- molar mass of oxygen,	$kgO_2/kmolO_2$
T_p	- particle temperature,	K
T_{wall}	- pipe internal surface temperature,	K
T_b	- gas temperature at bulk conditions,	K

S_{ext}	- external particle surface,	m^2
V_p	- particle volume,	m^3
α	- convective heat transfer coefficient,	$kW/(m^2 \cdot K)$
ϵ_{p-pw}	- mutual emissivity of the char particle-wall arrangement,	$-$
σ	- Stefan-Boltzmann constant,	$kW/(m^2 \cdot K^4)$
c_{char}	- specific heat capacity of solid material in char,	$kJ/(kg \cdot K)$
$\rho_{air}(T_p, p)$	- density of air calculated at $p = 1\ bar$ and T_p,	kg/m^3

Specific heat capacity of char solid material is estimated according to:

$$c_{char} = g_{ash} \cdot c_{ash} + g_C \cdot c_C \tag{7.2}$$

where:

g_{ash}	- ash mass fraction,	$kg\ ash/kg\ char$
g_C	- carbon mass fraction,	$kg\ C/kg\ char$
c_{ash}	- ash specific heat capacity,	$kJ/(kg \cdot K)$
c_C	- carbon specific heat capacity,	$kJ/(kg \cdot K)$

Specific heat capacity of carbon has been calculated using JANAF tables [112], while c_{ash} has been estimated from the following equation [113, 114]:

$$c_{ash} = (594 + 0.586 \cdot T_p)/1000 \tag{7.3}$$

Taking external and pore diffusion as well as heterogeneous reaction into consideration, the char conversion rate can be calculated as:

$$c_r = V_p \cdot M_C \cdot (1/\gamma) \cdot \eta \cdot k_{int} \cdot S_{V0} \cdot \beta_{eff} \cdot S_{ext} \cdot C_{O2} \cdot (\beta_{eff} \cdot S_{ext} + \eta \cdot k_{int} \cdot S_{V0} \cdot V_p)^{-1} \tag{7.4}$$

where:

β_{eff}	- effective mass transfer coefficient of O_2,	m/s
η	- effectiveness factor,	$-$

The effectiveness factor can be defined as the ratio of internal surface area, which participates in the heterogeneous reaction, to the internal surface area available for reaction in entire particle volume. This parameter is the indicator of pore diffusion limitation on the conversion rate [83] and is calculated from Thiele modulus (ϕ) according to equation [85, 115]:

$$\eta = (3/\phi^2) \cdot (\phi/tanh(\phi) - 1) \tag{7.5}$$

Thiele modulus can be calculated from equation [116]:

$$\phi = (d_p/2) \cdot (S_{V0} \cdot k_{int}/D_{eff})^{0.5} \tag{7.6}$$

where:

d_p	- particle diameter,	m
D_{eff}	- effective diffusivity,	m^2/s

The effective diffusivity coefficient can be calculated as [64, 67]:

$$D_{eff} = (\epsilon_0/\tau_{pore}) \cdot (1/D_g + 1/D_k)^{-1} \tag{7.7}$$

where:

D_g	- gas diffusivity,	m^2/s
D_k	- Knudsen diffusivity,	m^2/s

Gas diffusivity is calculated as binary O_2-air system diffusion for particle temperature from external routines available in the EES software. Knudsen diffusivity describes the diffusion rates inside pores. Knudsen diffusivity can be calculated as [67]:

$$D_k = (2/3) \cdot d_{pore\ av}/2 \cdot ((8 \cdot R \cdot T_p)/(\pi \cdot M_{O2}))^{0.5} \tag{7.8}$$

The effective mass transfer coefficient (β_{eff}), used in Equation 7.4, can be calculated as [82]:

$$\beta_{eff} = \mathtt{Sh} \cdot D_{g\ b}/d_p \tag{7.9}$$

where:

$\mathtt{Sh}$	- Sherwood number,	–
$D_{g\ b}$	- gas diffusivity at bulk temperature,	m^2/s

The Sherwood number represents the relation between convective and diffusive mass transfer. This dimensionless number has been calculated from the following equation [64, 117]:

$$\mathtt{Sh} = 2 + 0.6 \cdot \mathtt{Re}_b^{0.5} \cdot \mathtt{Sc}^{1/3} \tag{7.10}$$

where:

$\mathtt{Sc}$	- Schmidt number,	–

The Schmidt number is evaluated for the bulk temperature according to equation [64, 118]:

$$\mathtt{Sc} = \mu_b/D_{g\ b} \cdot \rho_b \tag{7.11}$$

The Reynolds number is calculated for bulk conditions from:

$$\mathtt{Re}_b = w \cdot d_p \cdot \rho_b/\mu_b \tag{7.12}$$

where:

w	- gas average velocity,	m/s
d_p	- char particle diameter,	m
ρ_b	- gas density at bulk temperature and standard pressure,	kg/m^3
μ_b	- gas dynamic viscosity at bulk temperature,	$Pa \cdot s$

In this model it is assumed that the particle shrinks immediately when the portion of carbon is consumed. Assuming constant density in unreacted core, the actual particle diameter can be calculated as [31]:

$$d_p = d_{p0} \cdot (1 - X)^{1/3} \tag{7.13}$$

where the d_{p0} is the initial particle diameter. Thus, the ash layer is removed as particle diameter decreases.

Coming back to Equation 7.1, the general equation for reaction enthalpy of carbon oxidation is:

$$\Delta h_r = \Delta h_r(CO) \cdot (2 - 2 \cdot \gamma) + \Delta h_r(CO_2) \cdot (2 \cdot \gamma - 1) \tag{7.14}$$

where:

$\Delta h_r(CO)$	- specific reaction enthalpy of reaction 6.6,	kJ/kg
$\Delta h_r(CO_2)$	- specific reaction enthalpy of reaction 6.5,	kJ/kg

Negligible small surface area of particle in comparison to surrounding walls allows for assumption that mutual emissivity is equal to emissivity of particle surface (ϵ_{p-pw}=ϵ_p).

The convection heat transfer coefficient is estimated as:

$$\alpha = \mathtt{Nu} \cdot \lambda_b / (d_p \cdot 1000) \tag{7.15}$$

where:

λ_b	- gas thermal conductivity at bulk temperature,	$W/(m \cdot K)$

The Nusselt number can be calculated as [64, 117]:

$$\mathtt{Nu} = 2 + 0.6 \cdot \mathtt{Re}_b{}^{0.5} \cdot \mathtt{Pr}_b{}^{0.33} \tag{7.16}$$

where:

$\mathtt{Pr}_b$	- Prandtl number estimated for bulk temperature of air,	–

In order to calculate the actual average temperature (Eq. 7.17) and mass (Eq. 7.18) of the particle, the $dT/d\tau$ and c_r from Equations 7.1 and 7.4 have been integrated using 0.5 s time step.

$$T_p = T_{p0} + \int_0^{\tau} \frac{dT_p}{d\tau} d\tau \tag{7.17}$$

$$m_p = m_{C0} - \int_0^{\tau} c_r d\tau + m_{ash} \tag{7.18}$$

where:

m_{C0}	- initial mass of carbon in char,	kg
m_{ash}	- mass of ash at time τ,	kg
T_{p0}	- initial particle temperature,	K

7.2.2 Shrinking core model (SCM)

The shrinking core model assumes constant particle diameter, while its inner unreacted core shrinks gradually with conversion. Therefore, the energy balance is considerably different to the one formulated for the SPM (Eq. 7.1). Figure 7.2 shows a pictorial representation of the terms appearing in the energy balance (7.19). Since a constant area of heat exchange with particle conversion is applied in the SCM, the heat exchange due to radiation and convection is larger in comparison to the SPM. Another difference is associated with energy storage in the particle at each time step.

$$\begin{aligned} c_r \cdot \Delta h_r - ((h_{CO2}^{Tp} - h_{CO2}^{298.15}) \cdot (2 \cdot \gamma - 1) \cdot c_r \cdot (M_{CO2}/M_C) \\ +(h_{CO}^{Tp} - h_{CO}^{298.15}) \cdot (2 - 2 \cdot \gamma) \cdot c_r \cdot (M_{CO}/M_C) \\ -(h_{O2}^{Tb} - h_{O2}^{298.15}) \cdot c_r \cdot \gamma \cdot (M_{O2}/M_C) \\ +\alpha \cdot S_{ext} \cdot (T_p - T_b) + \epsilon_{p-pw} \cdot \sigma \cdot S_{ext} \cdot (T_p^4 - T_{wall}^4)) \\ = \frac{dT_p}{d\tau} \cdot (V_{core} \cdot (1 - \epsilon_0) \cdot c_{char} \cdot \rho_{true} + V_{core} \cdot \epsilon_0 \cdot c_{p\ air}(T_p) \cdot \rho_{air}(T_p, p) \\ +(V_p - V_{core}) \cdot (1 - \epsilon_{ash}) \cdot c_{ash} \cdot \rho_{true} + (V_p - V_{core}) \cdot \epsilon_{ash} \cdot c_{p\ air}(T_p) \cdot \rho_{air}(T_p, p)) \end{aligned} \tag{7.19}$$

where:

V_{core}	- unreacted core volume of char particle,	m^3
ϵ_{ash}	- final porosity of external ash layer,	$m^3\ gas/m^3$

Final ash porosity is estimated from:

$$\epsilon_{ash} = 1 - (m_{ash}/V_p)/\rho_{true} \tag{7.20}$$

The conversion rate of char can be calculated from:

$$c_r = V_{core} \cdot M_C \cdot (1/\gamma) \cdot \eta \cdot k_{int} \cdot S_{V0} \cdot \beta_{eff2} \cdot S_{ext} \cdot C_{O2} \cdot (\beta_{eff2} \cdot S_{ext} + \eta \cdot k_{int} \cdot S_{V0} \cdot V_{core})^{-1} \tag{7.21}$$

where:

β_{eff2}	- effective mass transfer coefficient of O_2 used in SCM,	m/s

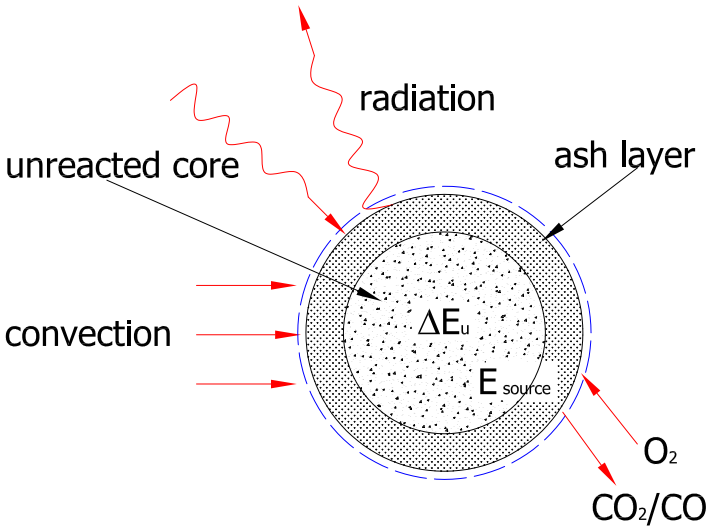

FIGURE 7.2: Diagram of energy balance of char particle used in 0D SCM

Oxygen effective mass transfer coefficient (β_{eff2}), in contrary to the SPM, has an additional term, which deals with oxygen diffusion through the ash layer. It is assumed here that ash layer has sufficiency large pores to allow free oxygen diffusion, thus no Knudsen diffusion is taken into consideration. The effective mass transfer coefficient is calculated from the following equation [93]:

$$\beta_{eff2} = (1/\beta_{eff} + d_p \cdot (d_p - d_{core})/(2 \cdot d_{core} \cdot D_g))^{-1} \tag{7.22}$$

where:

d_{core} - diameter of unreacted particle core, m

The core diameter is assumed to shrink according to Equation 7.13. The Thiele modulus (Eq. 7.6) is adjusted to have d_{core} instead of d_p. Other variables are calculated from appropriate equations presented in Section 7.2.1.

7.3 Simulation results and validation

Table 7.1 shows input variables used in both the SPM and the SCM. The models have been run to simulate the experiments performed for spherical char particles listed in Table 4.3. The initial particle diameters in the 0D model are: 1 - 5.15 *mm*, 2 - 4.75 *mm*, 3 - 6.20 *mm*, 4 - 5.90 *mm* and 5 - 5.15 *mm*. The integration time step, which has been used in the model, is 0.5 *s*.

TABLE 7.1: Input variables for 0D char combustion models

Parameter	Unit	Value
g_{ash}	$kg\ ash/kg\ char$	0.14
g_C	$kg\ C/kg\ char$	0.86
$\Delta h_r(CO)$	$kJ/kg\ C$	$9.212E+3$ [119]
$\Delta h_r(CO_2)$	$kJ/kg\ C$	$32.796E+3$ [119]
M_C	$kg\ C/kmol\ C$	12
M_{CO2}	$kg\ CO_2/kmol\ CO_2$	44
M_{CO}	$kg\ CO/kmol\ CO$	28
M_{O2}	$kg\ O_2/kmol\ O_2$	32
p	bar	1
S_{V0}	m^2/m^3	$3.11E+7$
T_b	K	1069
T_{p0}	K	300
T_{wall}	K	600
w	m/s	3.3
ϵ_0	m^3 gas / m^3	0.286
ϵ_p	–	0.8
ψ	–	2.28
ρ_{app0}	kg/m^3	1163
ρ_{true}	$kg/m^3\ solid$	1628
τ_{pore}	–	1.2

7.3.1 Shrinking particle model

The mass loss of three different particles are shown in Figure 7.3. With blue squares the experimental run no. 4 is presented, run no. 5 is shown in black triangles, while run no. 1 is marked with brawn circles (for initial mass and diameters see Table 4.3). Dashed lines show the SPM results, in which carbon combustion progresses to form both CO and CO_2. Changing stoichiometric coefficient (γ) of carbon-O_2 reaction into one and by using adequate Arrhenius constants (see Table 6.3) it is possible to calculate the particle mass loss for Reaction 6.5 (solid lines), where the carbon is oxidized to CO_2 only. Furthermore, by changing γ to 0.5 and Arrhenius constants to $A_{int} = 4.88E+03\ m/s$ and $T_A = 15970\ K$ it is possible to calculate mass loss for Reaction 6.6 (dotted lines), where the carbon is oxidized to CO only.

The time instance, when the first significant mass loss in the model is observed (circa 1% of initial particle mass) has been taken as the beginning of the experiments. Figures 7.3 and 7.4 show that combustion of char progresses faster when combustion of carbon to CO is considered (dotted lines) in comparison to combustion to CO_2 (solid lines). This is associated with the fact that two times less oxygen is consumed per *kmol* of carbon, because it is assumed that carbon monoxide is not consumed on the particle surface. Nevertheless, two times faster char conversion is not observed in that model. This is because the particle temperature is higher in case of combustion to CO_2 (Fig. 7.5), since the reaction enthalpy of carbon oxidation to carbon dioxide

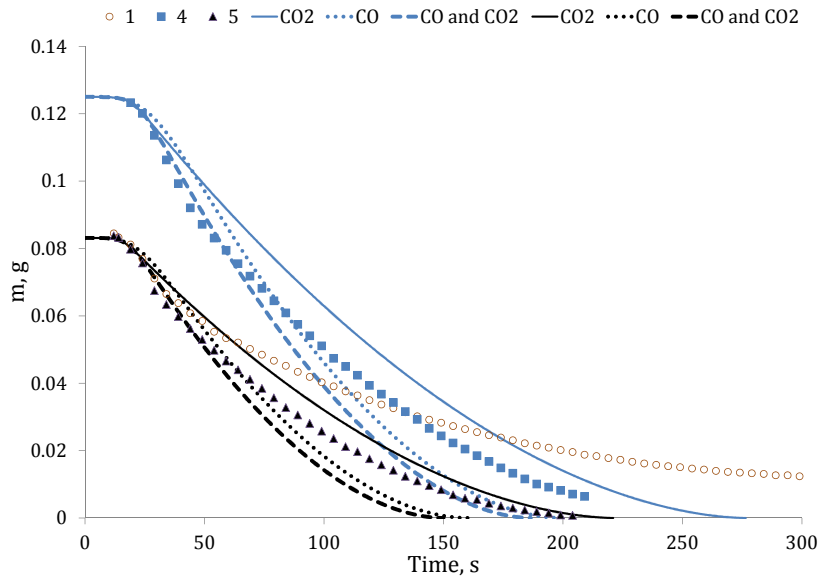

FIGURE 7.3: Measured and the SPM calculated mass loss; Squares (run no. 4), triangles (run no. 5) and circles (run no. 1) indicate measured data (initial mass and diameters shown in Table 4.3), while lines indicate calculation results (legend on the top of chart indicate the final product of carbon oxidation)

is higher (see Table 7.1); higher temperature means that the heterogeneous reaction progresses faster. When CO and CO_2 are the products, the combination of the two above mentioned phenomena cause that the combustion progresses even faster than for the case when only CO is the product of carbon oxidation.

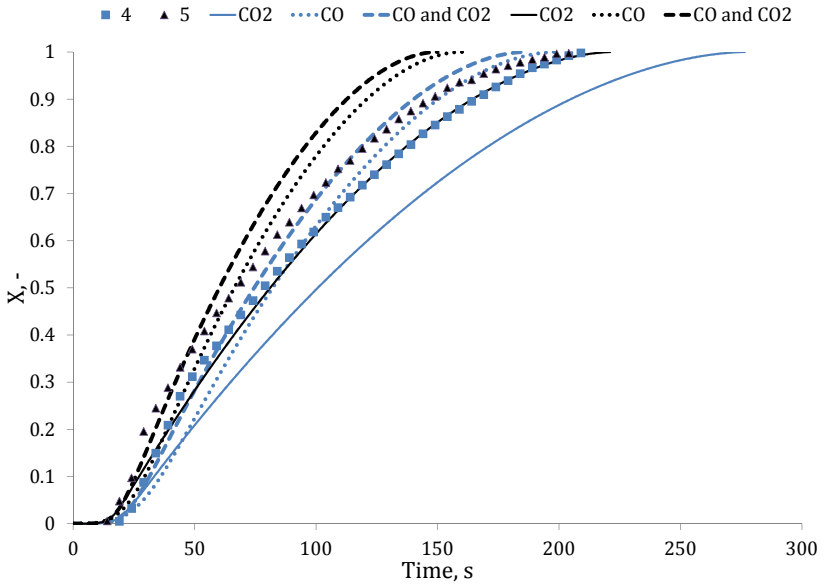

FIGURE 7.4: Measured and the SPM calculated char burnout; Squares (run no. 4) and triangles (run no. 5) indicate measured data (initial mass and diameters shown in Table 4.3), while lines indicate calculation results (legend on the top of chart indicate the product of carbon oxidation)

The particles mass losses for runs no. 4 and 5 (obtained from experiments) fall between

the SPM results obtained for carbon oxidation to CO_2 and to CO alone (Fig. 7.3). Nevertheless, during the initial twenty seconds the experimental mass loss rate is larger than the model predictions. Initial experimental mass loss is not only related to carbon combustion, but also to moisture and residual volatiles release from the particle (see Section 4.4). In addition, at the initial stage of combustion of the GTB-char, the external surface is larger in comparison to assumed surface of the modeled sphere. Larger external surface area is associated with cracks found on the surface of manually-rounded char particles (see Appendix B). The irregularities on particle surface are burned in the first instance, thus particle become more and more spherical when combustion progresses. Furthermore, at the initial stage of combustion, the model assumption that only carbon is the combustible part of char is inaccurate, since residual hydrogen is also present. All these model assumptions and simplifications make the 0D SPM not accurate for the fist stage of char combustion.

If run no. 1 is compared with model outcomes (see Fig. 7.3), a considerable difference in mass loss is found. This is due to the fact that particle no. 1 has relatively large amount of ash (around 14%, see Fig. 4.9), which stays on the unreacted particle core restricting oxygen diffusion to the unreacted carbon. Thus, it can be stated that combustion of particles with higher ash content, when ash stays on their surface, cannot be predicted using the SPM.

Passing through the first stage of char combustion for particles no. 4 and 5, at time around $40 - 50\ s$, the mass loss rate gradually decreases. The rate decrease is comparable with mass loss rate obtained from the model, which assumes carbon combustion to CO_2 only. To quantify the models, the relative difference of average conversion rates (δ_{m-mod}) have been calculated according to Equation 7.23. Average conversion rates ($c_{r\ av} = \Delta m/\Delta\tau$), shown in Table 7.2, are calculated using particle mass at 20% and at 95% of carbon burnout. Table 7.3 shows clearly that the lowest relative difference of average conversion rates is found for the model, where carbon dioxide is the only product of carbon oxidation. The differences in δ_{m-mod} for considered particles within one model could be explained by differences in particle composition. The models, in which carbon oxidizes according to C + γ O_2 $\Rightarrow$ (2 γ-1) CO_2 + (2-2 γ) CO reaction or C + 0.5 O_2 $\rightarrow$ CO reaction, overpredict measured conversion rates almost by 50%.

$$\delta_{m-mod} = \left|(c_{r\ av}^{exp} - c_{r\ av}^{mod})\right| / c_{r\ av}^{exp} \tag{7.23}$$

Figure 7.5 shows the comparison of particle temperature obtained using the SPM with the measurements (run no. 5). Good correlation between maximal registered temperature on the particle surface (red squeres) and modeled particle temperature has been found from around 30 s onwards, when the carbon oxidation to CO_2 is used in the SPM. Not only the curve tendency is preserved, but also the temperature level is similar. This can be explained by oxidation of CO, which occurs at the particle surface and this homogenous reaction (CO + 0.5 O_2 $\leftrightarrow$ CO_2) increases surface temperature to the levels, which are present when carbon oxidation to CO_2 is

TABLE 7.2: Comparison of average conversion rate obtained from measurements and from the SPM; $c_{r\ av}$ in mg/s

Particle number	**Measurements**	**Reaction products of SPM: CO_2 and CO**	**Reaction product of SPM: only CO_2**	**Reaction product of SPM: only CO**
2	0.433	0.615	0.389	0.590
3	0.531	0.883	0.558	0.847
4	0.605	0.825	0.522	0.792
5	0.453	0.687	0.434	0.657

assumed. The same conclusion was formulated by Basu [17]. At the latest stage of combustion, the SPM overpredicts the maximal surface temperature considerably. At this last 10% of the carbon oxidation, the particle diameter is so small that the particle heat loses are minimal.

TABLE 7.3: Relative difference of average conversion rates between model predictions and measurements; δ_{m-mod} in %

Particle number	**Reaction products of SPM: CO_2 and CO**	**Reaction product of SPM: only CO_2**	**Reaction product of SPM: only CO**
2	42.1	10.2	36.2
3	66.2	4.9	59.5
4	36.4	13.7	31.0
5	51.7	4.2	45.1
Average from particles 2-5	49.1	8.3	42.9

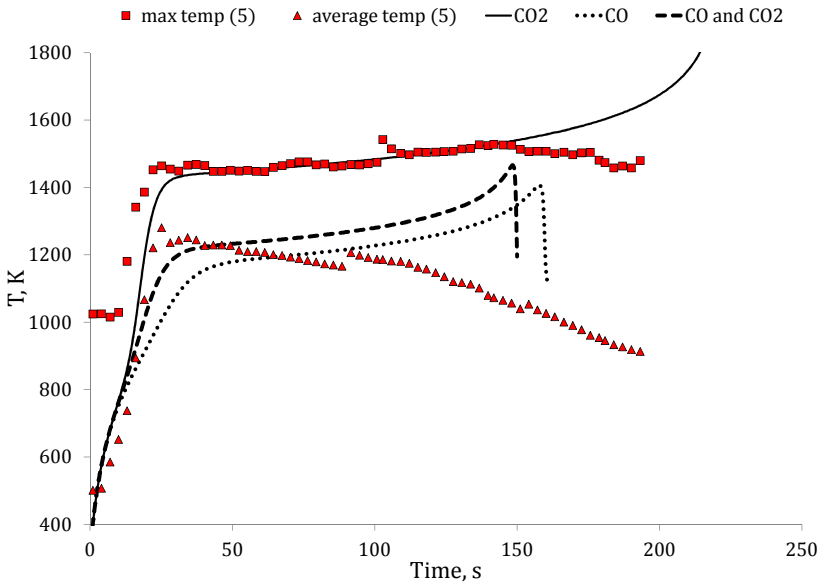

FIGURE 7.5: Measured and SPM calculated particle temperatures; Squares and triangles indicate measured maximal and average surface temperature for run no. 5 (initial mass and diameters shown in Table 4.3), while lines indicate calculation results (legend on the top of chart indicate the product of carbon oxidation)

Additionally, effective mass transfer coefficient is larger, thus char conversion turns from diffusion controlled to reaction/diffusion controlled. Similar conclusion was also drawn by Basu [17], who indicated that the char particle combustion in FBBs burns in diffusion/kinetic regime at the initial stages of combustion, while in later stages, when particle diameter is considerably smaller, the kinetics is the only rate-limited factor of char conversion. Let us consider the SPM predictions, when the carbon oxidation progress to CO and CO_2 (bold dashed line in Fig. 7.5) or to CO only (dotted black line in Fig. 7.5). As shown in Figure 7.5, the maximum measured value of surface particle temperature is around 200 K larger than the model calculated temperatures.

7.3.2 Shrinking core model

In the shrinking core model, the carbon burnout leads to widening of ash layer at the expense of unreacted char. This layer slows down the oxygen diffusion towards the unreacted core and char combustion mode changes from external diffusion controlled towards ash diffusion controlled [93]. The SCM has been used to simulate experimental run no. 1, listed in Table 4.3. The choice of run no. 1 is justified by the substantially different combustion in comparison to particles 2-5 (see Figure 4.9). Ash content of particle no. 1 is higher and the ash remained as "untouched" layer until the end of combustion. Initial particle mass taken as starting point for modeling is around 0.083 g, which corresponds to 5.15 mm particle diameter (assuming $\rho_{app0} = 1163\ kg/m^3$).

Figures 7.6 and 7.7 show measured mass loss and char burnout (triangles) and model calculation results. The measured mass loss at the initial stage of combustion is larger than the SCM predictions. This is associated with moisture and residual volatiles release. After circa 50 s the mass loss tendency is very similar to the model predictions, in which carbon is oxidized to both CO and CO_2, while the other two models slightly underpredict particle mass loss. After 120 s time, the experimental-obtained mass loss is larger than values predicted by each of models considered.

Taking into consideration particle temperatures predicted by the model for different reactions, it can be noticed that they are not correlated to measured maximum surface temperature (see Fig. 7.8). This is due to the fact that external surface of the particle is the same during the entire combustion time, while the surface available for reaction shrinks gradually. The assumption of uniform particle temperature causes that the particle temperature decreases with the char conversion. At a certain conversion, the temperature may be so low (especially if the model with C + 0.5 $O_2 \rightarrow$ CO reaction and the model with the C + γ $O_2 \Rightarrow$ (2 γ-1) CO_2 + (2-2 γ) CO reaction are considered) that the char oxidation rate is comparable with oxygen diffusion. From that point onwards, the char burnout is controlled by kinetics rather than diffusion.

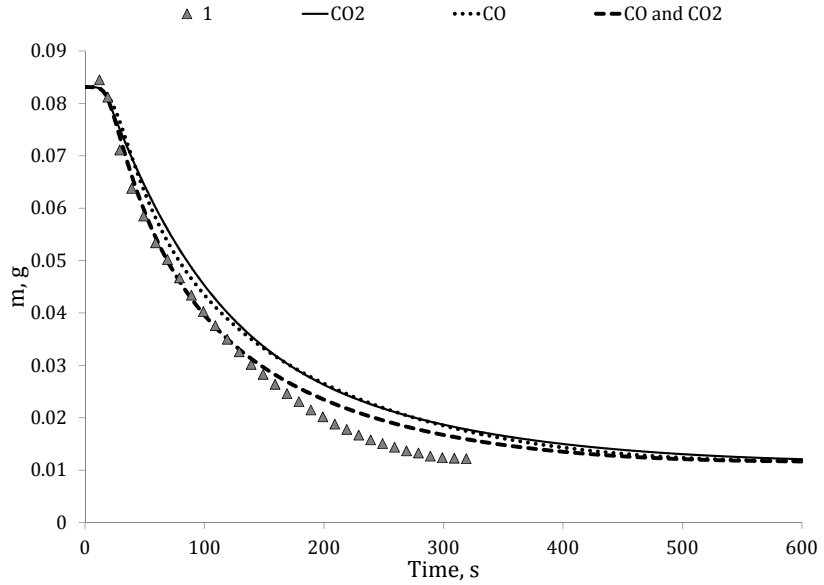

FIGURE 7.6: Comparison of mass loss obtained experimentally and using the SCM calculations; Triangles indicate measured data (run no. 1), while lines calculation results

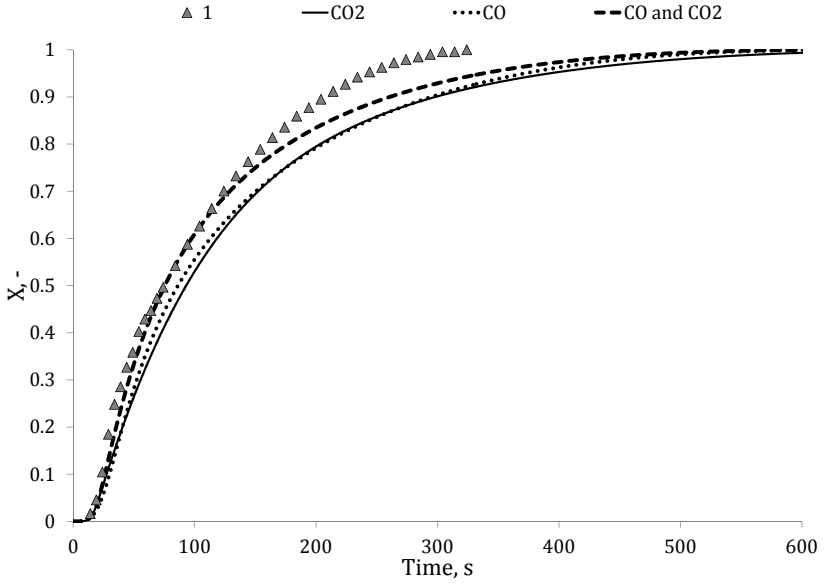

FIGURE 7.7: Comparison of carbon burnout obtained experimentally and using the SCM calculations; Triangles indicate measured data (run no. 1), while lines calculation results

Higher particle temperatures are predicted for the model, in which CO_2 is the only product of char oxidation (black solid line in Fig. 7.8). Higher temperatures, which are the result of larger reaction enthalpy than in case of C + 0.5 O_2 → CO reaction (see Table 7.1), accelerate the C + O_2 → CO_2 reaction. However, the slow oxygen diffusion through the ash layer prevents the faster carbon conversion. Especially because the stoichiometric coefficient of oxygen for C + O_2 → CO_2 reaction is two times larger than for reaction, for which CO is the only product of char oxidation. This means that to convert one gram of carbon two times more oxygen is needed if comparing to the C + 0.5 O_2 → CO reaction. Therefore, in this case diffusion and kinetics influences carbon conversion rate. The modeled particle temperature is well correlated to the average surface temperature measured by IR camera, which represents the external ash temperature layer.

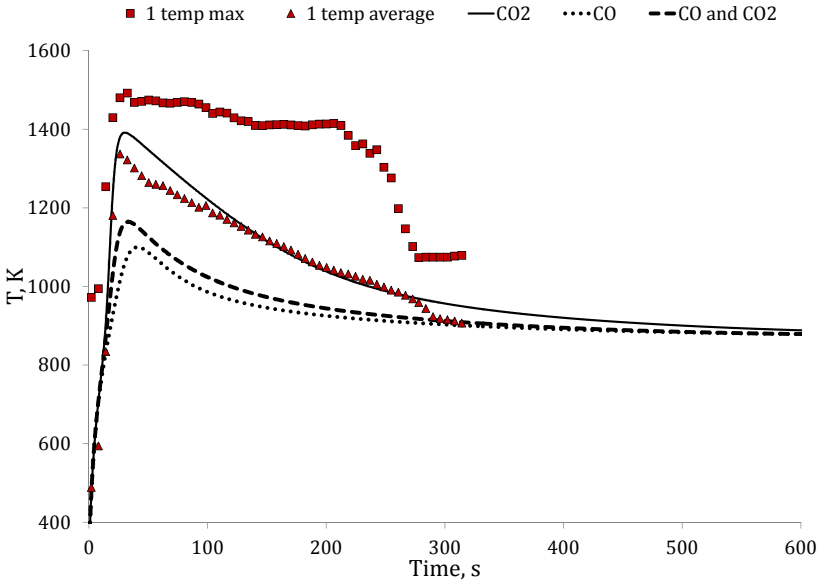

FIGURE 7.8: Comparison of particle temperature obtained experimentally and using the SCM calculations; Triangles and squares indicate measured data (run no. 1), while lines calculation results

The best fit to the mass loss measured data is observed for the model, in which carbon oxidizes to CO and CO_2. Calculated relative differences of average conversion rates with measured data for the SCM are shown in Table 7.4. The estimation procedure of this parameter is the same as for the SPM.

TABLE 7.4: Relative difference of average conversion rates between model predictions and measurements for the SCM; δ_{m-mod} in %

Particle number	**Reaction products of SCM: CO_2 and CO**	**Reaction product of SCM: only CO_2**	**Reaction product of SCM: only CO**
1	30.3	40.0	36.5

In order to demonstrate that ash diffusion is the rate controlling phenomena of high-ash containing particles, the calculations of conversion rate depended only on diffusion have been performed (boundary layer and ash diffusion are taken into account). Instead of Equation 7.21, the following conversion rate equation have been implemented into the model:

$$c_r = S_{ext} \cdot M_C \cdot (1/\gamma) \cdot \beta_{eff2} \cdot C_{O2} \tag{7.24}$$

Figures 7.9 and 7.10 show plots of particle mass and temperature obtained using the SCM and measurements. Elimination of reaction kinetics from the model causes that combustion of modeled particle starts immediately. In comparison to Figure 7.6, significant changes to the mass loss rates are seen, which are considerably larger, when the kinetics is excluded from the model. The kinetics included in the SCM causes that char conversion rate is not any more dependent on diffusion only, and therefore is slower. The particle mass loss obtained from the model, in which carbon oxidizes to CO_2, fits almost perfectly to measured data, while two other models with reactions 6.2 and 6.6 predict almost two times faster carbon burnout. The model, in which carbon monoxide and carbon dioxide are products of carbon oxidation, predicts the mass loss, which lays between two other models results, however much closer to model predictions, when only CO is produced. This means that reaction 6.2 favors CO production at temperatures obtained in this model. In reality, carbon monoxide from the C + γ O_2 $\Rightarrow$ (2 γ-1) CO_2 + (2-2 γ) CO reaction is almost entirely combusted either inside the particle or within its boundary layer. Therefore, the quantity of oxygen, which has to diffuse from surroundings is equal to this which is predicted by the SCM, in which carbon oxidation to CO_2 only is assumed. In addition the heat release rate due to the C + O_2 $\rightarrow$ CO_2 reaction is also similar to reality, which could be observed by comparing surface average temperature of the particle with model predictions.

Relative difference of average conversion rates between model predictions (model with diffusion only) and measurements is 0.7% for the case where CO_2 is considered as the only product of carbon oxidation.

7.3.3 Summary

Zero-dimensional models are capable of predicting in relatively simple way the char conversion rates. These models could bring benefits for CFD simulations of an entire combustion chamber. Nevertheless, it is necessary to choose the best model for specific conditions in a boiler. From performed analysis it can be concluded that the most suitable 0D model for the fluidized bed combustion is the SPM, which assumes char combustion to CO_2 only. The reason for choosing this model is that the particle collisions are likely to remove the ash layer formed during combustion.The best fit to the experimental data has been obtained when carbon oxidation

proceeds as $C + O_2 \rightarrow CO_2$. Therefore, the SPM with this reaction can be used in conjunction with CFB-based model.

The second model (SCM), considered in this chapter, may be useful in CFD-based modeling of grate boilers. However, the particle temperature uniformity, assumed in the present investigation, should be replaced to temperature differentiation with radius. In this case insulation influence of ash layer could be taken into account, which would make the predictions of the particle mass loss more accurate.

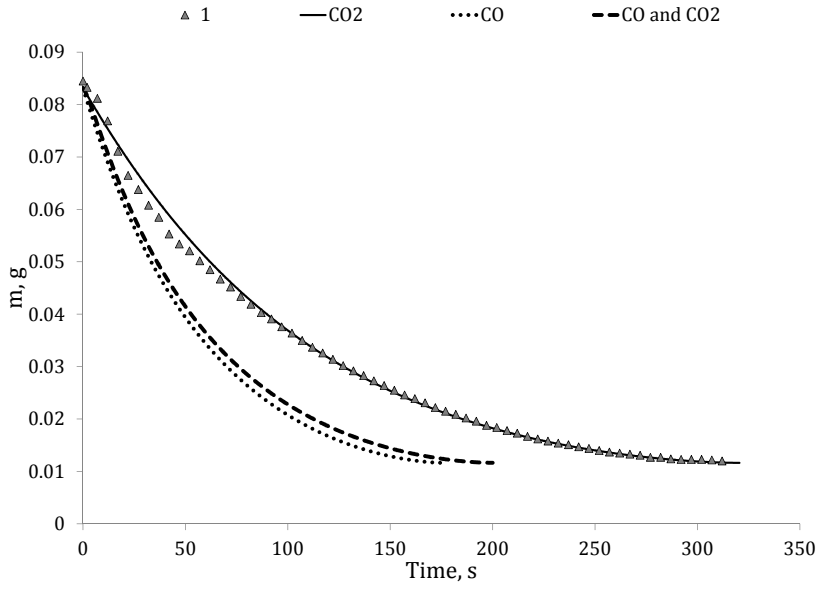

FIGURE 7.9: Comparison of mass loss obtained experimentally and using the SCM calculations; Triangles indicate measured data (run no. 1), while lines calculation results

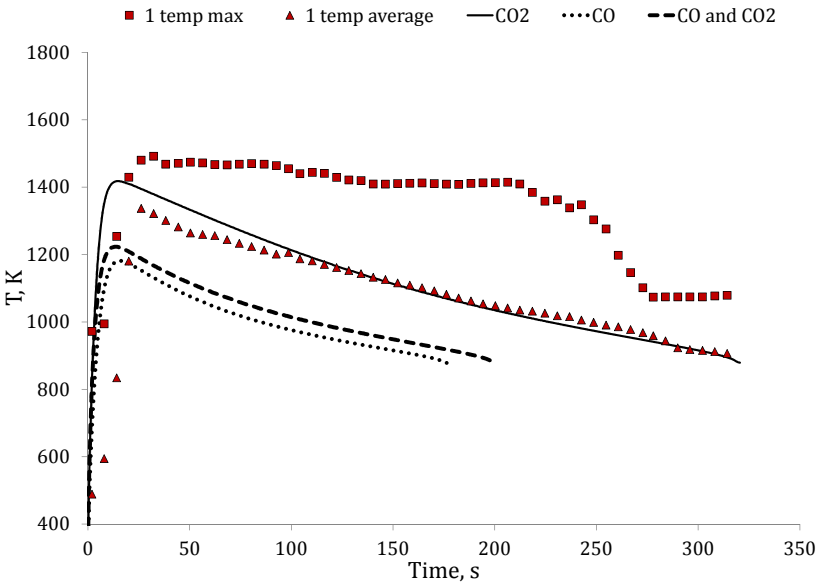

FIGURE 7.10: Comparison of particle temperature obtained experimentally and using the SCM calculations; Triangles and squares indicate measured data (run no. 1), while lines calculation results

Chapter 8

Two-dimensional model of char particle combustion

8.1 Introduction

While developing both the zero-dimensional models (see Chapter 7) and one-dimensional models many simplifications and assumptions have to be made. In the zero-dimensional models the parameters describing the combustion process are time-dependent only, while in one-dimensional models they vary with both the time and the particle radius. In reality these parameters change three-dimensionally and are time dependent. The aim of this part of the thesis is to develop a model, which could simulate the GTB experiments in such a way that the char combustion at any instant is represented by 2-dimensional fields of variables. Numerical studies, described in this chapter, are aimed to provide answers to the following questions:

- How large are temperature and species gradients inside the particle during combustion and how these gradients influence the char conversion rates?
- Is carbon monoxide burned inside the particle, within the particle boundary layer or rather far away from the particle surface?
- To which extend Boudouard reaction is important at conditions found in the GTB test rig?
- What is the influence of flow of air on the particle combustion?

To answer the above questions it is necessary to develop a detailed model, in which parameters like temperature, species concentration, etc. can vary at least in two spatial coordinates. Two- or three-dimensional models of char particle combustion are rarely encountered in the literature.

Yang et al. [32] created the 2D model of moisture evaporation, devolatilization and remaining char combustion of a single cylindrical particle of biomass (size of half to twenty millimeters). The model included the flow of hot gases around the particle, which allowed for its heating up to the point of devolatilization onset, the devolatilization process, which was then followed by char combustion. The laminar flow, radiative heat exchange between particle surface and surrounding walls and direction of the particle volume shrinkage proportional to the propagation direction of a mass-loss front were important assumptions in this model [32]. The authors employed the equation for local porosity variation inside the particle; porosity was related to moisture evaporation, volatile release and fixed-carbon combustion processes. The reaction of carbon with oxygen was the only heterogeneous reaction considered. The model predictions were compared with experimental data. One of the most important conclusions was that biomass particles, which are larger than circa 0.2 *mm*, have to be treated as thermally-thick (Bi$>$ 1) and the temperature gradient cannot be neglected in the calculations [32].

Wendt et al. [33] developed a two-dimensional model of devolatilization and ignition of a single coal particle, which was exposed to radiative heat transfer and to thermal conduction from surrounding atmosphere. The model took into account intrinsic char combustion depending on local temperature and oxygen concentration. The assumption of this model was that the coal particle was ash and moisture free and that devolatilization did not change the particle shape. The particle was assumed to be a gray-body radiator. A non-spherical and axisymmetric particle was investigated. Local equilibrium within gas and solid phase was assumed inside the particle. The simplified char oxidation mechanism was considered in this model ($C+O_2 \rightarrow CO_2$). Molecular and Knudsen diffusivity were included in the model. Particles in the 0.05 *mm* to 1 *mm* diameter range were investigated. The authors concluded that in particles larger than 0.3 *mm* intraparticle temperature gradient exists, which affects fuel ignition [33].

8.2 Model geometry and boundary conditions

The two-dimensional model has been created to simulate the char particles combustion in the GTB test rig (see Chapter 4).

8.2.1 Model geometry

Geometry of the model has been created to represent a part of the test rig, which dimensions are shown in Figure 4.3. The two-dimensional axisymmetric model has been developed and the model geometry is shown in Figure 8.1. For simplicity the particle holder and the ceramic pipe are neglected (see Fig. 4.3).

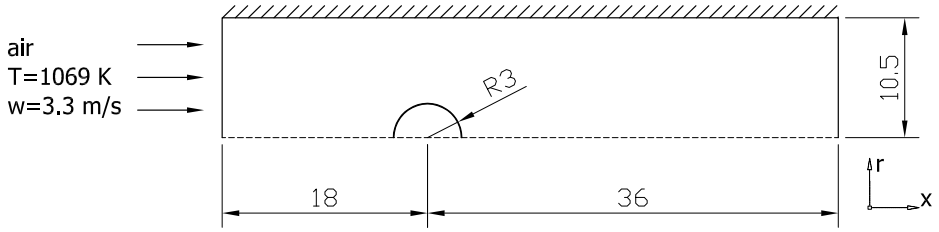

FIGURE 8.1: Model geometry; Dimensions in *mm*

Run no. 6 (see Table 4.3) has been chosen for numerical simulations. Since the ash layer remained on the particle throughout the experiments, it is assumed that the modeled char particle radius does not change during the combustion process. Because the char particle used in the GTB experiments contained some moisture and residual volatiles, therefore a 6 *mm*-size particle has been modeled, which is slightly smaller than the 6.3 *mm* particle of the run no. 6.

8.2.2 Boundary conditions

The computational domain contains three interiors, as shown in Figure 8.2. Interior-1 represents the gas flow, while Interior-2 and -3 is the porous zone representing the particle. Interior-3 is the 0.05 *mm* thick zone, on the outer surface of the particle. The reason for using Interiors -2 and -3 is that in Interior-3 additional energy source has been implemented. Positioning of the boundary conditions is shown in Figure 8.2. The model's initial settings used at each boundary are shown in Table 8.1.

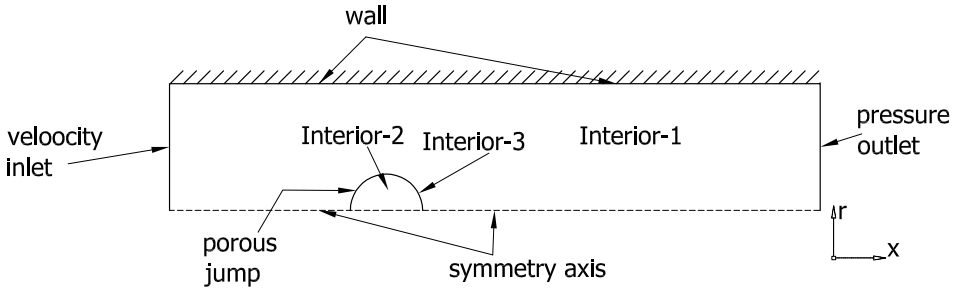

FIGURE 8.2: Position of boundary conditions of the model

The porous media condition, applied in Interiors -2 and -3, allows for setting the resistance of gas flow and for modeling of diffusion of each species inside the entire volume. Porous jump condition is capable of establishing additional pressure drop between gas and porous medium. Here, the zero-thickness membrane has been set (see Table 8.1), thus, the pressure drop is zero.

TABLE 8.1: Chosen values for specific boundary conditions or initial settings

Boundary condition	**Initial settings and boundary conditions**
Axis	Symmetry axis
Velocity inlet	$w = 3.3\ m/s$; $T_b = 1069\ K$; $z_{N2} = 0.79$, $z_{O2} = 0.21$
Pressure outlet	Gauge pressure of $0\ Pa$; $T = 300\ K$
Porous jump	Porous media thickness: $0\ m$
Wall	Constant wall temperature $T_{wall} = 600\ K$
Interior-1	Gas mixture; $T_b = 1069\ K$, $p_b = 101325\ Pa$, $z_{N2} = 0.79$, $z_{O2} = 0.21$
Interior-2	Porous media: solid - gas structure; $T_{p0} = 300\ K$, $p_{p0} = 101325\ Pa$, $z_{N2} = 0.77$, $z_{O2} = 0.21$, $z_{CO2} = 0.01$, $z_{CO} = 0.01$
Interior-3	Porous media: solid - gas structure; $T_{p0} = 300\ K$, $p_{p0} = 101325\ Pa$, $z_{N2} = 0.77$, $z_{O2} = 0.21$, $z_{CO2} = 0.01$, $z_{CO} = 0.01$

8.2.3 Numerical mesh

In each of the three interiors a numerical mesh is created (see Fig. 8.3) for equations discretization. The mesh has to be dense enough to obtain reliable results, nevertheless, number of cells influences computational time, especially when transient calculations are performed. Also denser mesh influences positively the calculations convergence. Taking these factors into account a dense mesh has been generated in locations where large gradients are expected that is within particle boundary layer and inside the particle, as shown in Figure 8.3. Inside the particle (Interiors -2 and -3) "quad/pave" mesh type is used while in gas volume "tri" mesh type is used. In total 50902 cells are used. Minimum orthogonal mesh quality is 0.853, while maximum aspect ratio is 3.440.

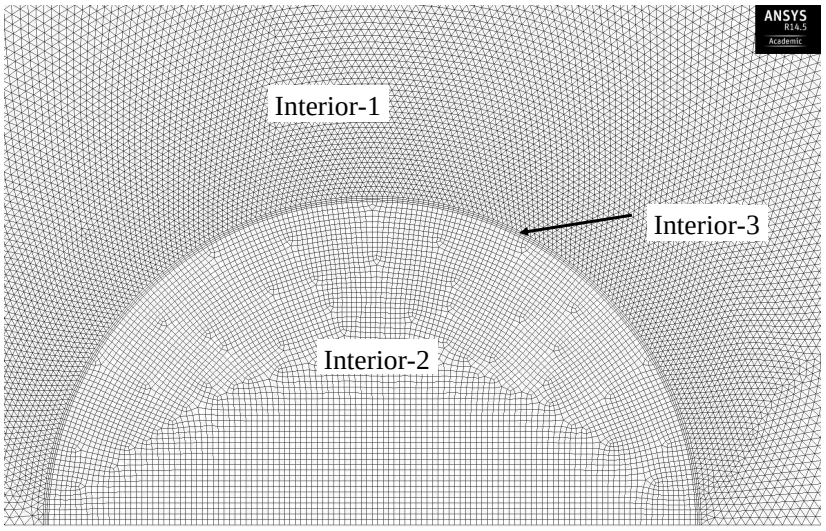

FIGURE 8.3: Numerical mesh in and nearby the particle

8.3 Mathematical description of the 2D model

In this Section, a detailed mathematical description of the char particle combustion model is provided. The following model simplifications are adopted:

- The particle is spherical and its diameter remains constant through the combustion process;
- The char consists of carbon, ash and gas in pores;
- The ash is not removed from the particle surface; it means an ash layer is formed during the combustion process;
- Thermal equilibrium between solid material and gas exists in each cell of Interiors -2 and -3;
- Densities of carbon and ash are equal;
- All gases are treated as ideal;
- The reacting gas flow is laminar in Interior-1;
- Radiation heat exchange exists between the particle external layer and the surrounding pipe wall;
- The particle is a gray-body radiator and its emissivity is constant;
- Both the temperature and emissivity of the pipe wall, which surrounds the particle, are constant;
- Gases do not participate in radiative heat transfer;
- Gravity has been neglected.

In the model, which has been created in Ansys Fluent 14.5 software, four gaseous species are considered: CO_2, O_2, CO and N_2. Two heterogeneous reactions are taken into account in the model: the carbon reaction with oxygen according to $C + \gamma O_2 \Rightarrow (2\gamma - 1)CO_2 + (2 - 2\gamma)CO$ and Boudouard reaction ($C + CO_2 \Rightarrow 2CO$). One homogenous reversible reaction is taken into consideration: ($CO + 0.5O_2 \rightleftharpoons CO_2$). The homogenous reaction can progress both inside the particle pores and in the gas phase and is depended on temperature and species availability. It is assumed, that the diffusion is the only mechanism for transport of reacting gases toward the particle center.

8.3.1 Energy conservation equation for porous medium

For porous media, where the solid material is in thermal equilibrium with gas in pores, the following energy conservation equation is solved:

$$\begin{aligned} &\frac{\partial}{\partial \tau}(\epsilon \cdot \rho_g \cdot h_g + (1-\epsilon) \cdot \rho_{true} \cdot h_s) \\ &= S_e + S_{er} + S_{he} \cdot \epsilon + \nabla \cdot (\lambda_{eff} \cdot \nabla T - \sum_i h_i \cdot m_{i\,S}) \end{aligned} \tag{8.1}$$

where:

ρ_g	- gas density,	$kg\ g/m^3\ g$
h_g	- specific physical enthalpy of gas,	J/kg
h_s	- specific physical enthalpy of solids,	J/kg
h_i	- specific physical enthalpy of the i^{th} species,	$J/kg\ i$
S_e	- heterogeneous reaction enthalpy source term,	W/m^3
S_{er}	- radiation source term,	W/m^3
S_{he}	- homogenous reaction enthalpy source term,	W/m^3
$m_{i\,S}$	- mass flux of the i^{th} species,	$kg\ i/(m^2 \cdot s)$
λ_{eff}	- effective thermal conductivity,	$W/(m \cdot K)$

The effective thermal conductivity of the porous medium is calculated as the volume-weighed average of the fluid and solid conductivity using the following equation [120]:

$$\lambda_{eff} = \epsilon \cdot \lambda_g + (1-\epsilon) \cdot \lambda_s \tag{8.2}$$

where:

λ_g	- thermal conductivity of gas,	$W/(m \cdot K)$
λ_s	- thermal conductivity of solid,	$W/(m \cdot K)$

The thermal conductivity of gas mixture is calculated from ideal-gas-mixing-law, while solid fuel conductivity from dependence formulated by Atkinson and Merrick [121] and used in work of Buczyński [35]:

$$\lambda_s = T^{0.5} \cdot (\rho_{true}/4511)^{3.5} \tag{8.3}$$

This above relationship has been expanded into polynomial function of temperature ($\lambda_s = -1.089E-07 \cdot T^2 + 6.883E-04 \cdot T + 3.115E-01$). Radiation in pores has been omitted, due to the small pores sizes (initial average size of 40.2 *nm*). According to Atkinson and Merrick [121], who describe the contribution of the radiation in total heat transfer in porous material by adding an additional term into thermal conductivity ($\lambda_r = 2.28 \cdot 10^{-7} \cdot \delta x \cdot T^3$; where δx is the mean distance traveled by radiation - in the present work δx=$d_{pore\ av0}$), this additional term amounts to less than 0.1% of the gas conductivity at temperature of 1500 K.

The specific enthalpy of gas and solids is calculated as:

$$h = \int_{T_{ref}}^{T} c_p \cdot dT \tag{8.4}$$

where:

c_p - specific heat capacity at constant pressure, $J/(kg \cdot K)$

The specific heat capacity of solids, used in Equation 8.4, is calculated according to Equation 7.2 ($c_{char} = g_{ash} \cdot c_{ash} + g_C \cdot c_C$). This relationship has been expanded into a polynomial function of the following form: $c_{char} = 7.173E-15 \cdot T^5 - 3.676E-10 \cdot T^4 + 2.075E-06 \cdot T^3 - 4.691E-03 \cdot T^2 + 5.143 \cdot T - 4.574E+02$.

The specific heat capacity for gas mixture is calculated as:

$$c_{p\ mix} = \sum_{i=1}^{N} c_{p\ i} \cdot g_i \tag{8.5}$$

where:

$c_{p\ i}$ - specific heat capacity of the ith species, $J/(kg\ i \cdot K)$

g_i - mass fraction of the ith species, $kg\ i/kg$

The energy source due to exothermic or endothermic heterogeneous reactions (carbon oxidation with O_2 and Boudouard reaction) is calculated in the entire particle volume as:

$$S_e = c_{r\ oxy} \cdot (\Delta h_r(CO_2) \cdot (2 \cdot \gamma - 1) + \Delta h_r(CO) \cdot (2 - 2 \cdot \gamma)) - c_{r\ B} \cdot \gamma_{CO2} \cdot \Delta h_r(B) \tag{8.6}$$

where:

$c_{r\ oxy}$ - carbon conversion rate caused by reaction with O_2, $kg\ C/(m^3 \cdot s)$

$c_{r\ B}$ - carbon conversion rate caused by reaction with CO_2, $kg\ C/(m^3 \cdot s)$

$\Delta h_r(B)$ - specific enthalpy of Boudouard reaction , $kJ/kg\ C$

The carbon conversion rate for C + γ O_2 $\Rightarrow$ (2 γ-1) CO_2 + (2-2 γ) CO reaction ($c_{r\ oxy}$) is calculated as follows (see Eq. 6.7 for comparison):

$$c_{r\ oxy} = \epsilon \cdot 1/\gamma \cdot M_C \cdot k_{int} \cdot S_V \cdot C_{O2} \tag{8.7}$$

The carbon conversion rate associated with Boudouard reaction has been calculated according to (see Eq. 6.15 for comparison):

$$c_{r\ B} = \epsilon \cdot 1/\gamma_{CO2} \cdot M_C \cdot k_{int} \cdot S_V \cdot C_{CO2} \tag{8.8}$$

The radiative heat transfer between the particle outer surface and the inner surface of the pipe has been taken into account. It has been assumed that because of porous structure of char,

a thin outer layers of the char particle participate in the radiative heat transfer (Interior-3 - see Figure 8.3). The radiative source term in the energy balance depends only on the local particle surface temperature and is calculated as:

$$S_{er} = -(T^4 - T^4_{wall}) \cdot \epsilon_{p-pw} \cdot \sigma \cdot S_{ext}/V_{ring} \tag{8.9}$$

where:

V_{ring} - volume of the Interior-3 (see Figures 8.2 and 8.3), m^3

Volume of the Interior-3 is calculated using:

$$V_{ring} = 4/3 \cdot \pi \cdot ((d_p/2)^3 - ((d_p - 2 \cdot 0.00005)/2)^3) \tag{8.10}$$

The homogenous reaction enthalpy source term used in Equation 8.1 is calculated using enthalpy of formation for species participating in $CO + 0.5O_2 \rightleftharpoons CO_2$ reaction:

$$S_{he} = 0.5 \cdot h^0_{ref\ O2} + h^0_{ref\ CO} - h^0_{ref\ CO2} \tag{8.11}$$

where:

$h^0_{ref\ i}$ - the i^{th} species specific enthalpy of formation,
at reference temperature (T_{ref}), $J/kg\ i$

8.3.2 Energy conservation equation for gas phase

The following energy conservation equation is solved for Interior-1 (gas phase):

$$\frac{\partial}{\partial \tau}(\rho_g \cdot h_g) + \nabla \cdot (\vec{w} \cdot (\rho_g \cdot h_g)) = S_{he} + \nabla \cdot (\lambda_{eff} \cdot \nabla T - \sum_i h_i \cdot m_{i\ S}) \tag{8.12}$$

where:

$\vec{w}$ - velocity vector, m/s

In the above equation the accumulation and convection terms appear on the left hand side and heat conduction, diffusion and heat generation term due to the homogenous reaction on the right hand side.

8.3.3 Mass conservation equation for porous medium

For the porous zone (Interiors-2 and -3) the continuity equation can be written separately for gas:

$$\frac{\partial(\rho_g \cdot \epsilon)}{\partial \tau} = S_g \tag{8.13}$$

and solids:

$$\frac{\partial(\rho_{true} \cdot (1-\epsilon))}{\partial \tau} = S_C \tag{8.14}$$

where:

S_g	- gas phase mass source term,	$kg/(m^3 \cdot s)$
S_C	- solid phase mass source term,	$kg\ C/(m^3 \cdot s)$

The gas phase mass source is calculated as:

$$S_g = c_{r\ oxy} + c_{r\ B} \tag{8.15}$$

while the solid phase source as:

$$S_C = -c_{r\ oxy} - c_{r\ B} \tag{8.16}$$

The mass balance for individual species, in the porous medium, is calculated according to Equation 8.17 for CO_2, O_2 and CO; the nitrogen mass fraction is calculated as: $g_{N2} = 1 - g_{O2} - g_{CO2} - g_{CO}$.

$$\frac{\partial(\rho_g \cdot \epsilon \cdot g_i)}{\partial \tau} = \nabla \cdot (\rho_g \cdot \epsilon \cdot D_{eff\ i} \cdot \nabla g_i) + S_{g\ i} + R_i \cdot \epsilon \tag{8.17}$$

where:

$S_{g\ i}$	- mass source term of the ith species,	$kg\ i/(m^3 \cdot s)$
R_i	- net source of the ith species due to homogenous reactions,	$kg\ i/(m_g^3 \cdot s)$
$D_{eff\ i}$	- effective diffusivity of the ith species,	m^2/s

The effective diffusivity of each species has been calculated as [64, 67]:

$$D_{eff\ i} = (\epsilon/\tau_{pore}) \cdot (1/D_{g\ i-mix} + 1/D_{k\ i})^{-1} \tag{8.18}$$

Knudsen diffusivity of the ith species is calculated as [67]:

$$D_{k\ i} = (2/3) \cdot d_{pore\ av}/2 \cdot ((8 \cdot R \cdot T_p)/(\pi \cdot M_i))^{0.5} \tag{8.19}$$

The diffusion coefficients of each components in the mixture is calculated by Equation 8.20 derived by Wilke [122] and described by Welty et al. [123].

$$D_{g\ i-mix} = \frac{1}{\sum_{j \neq i}^{n-1} z'_j / D_{i-j}} \tag{8.20}$$

where:

z'_j	- mole fraction of the jth species in the gas mixture evaluated on the ith species free basis,	–

D_{i-j} - binary pair mass diffusion coefficient of the ith species in the jth species, m^2/s

The mole fraction of the jth species in the gas mixture evaluated on the ith species free basis is calculated from:

$$z'_j = \frac{z_j}{1 - z_i} \tag{8.21}$$

The diffusion coefficient of the ith species in the jth species is estimated from the following relationship [67]:

$$D_{i-j} = D^0_{i-j} \cdot (T/298.15)^{1.64} \cdot (101325/p) \tag{8.22}$$

where:

D^0_{i-j} - Mass diffusion coefficient of the ith species in the jth species calculated at $T = 298.15\ K$ and $p = 101325\ Pa$, m^2/s

The net source of the ith species due to homogenous reactions is calculated in the model for the entire calculation domain (Interiors -1, -2 and -3). The following equation is applied:

$$R_i = \sum_{l=1}^{N_l} M_i \cdot r_{i,l} \tag{8.23}$$

where:

$r_{i,l}$ - Arrhenius molar rate of creation of the ith species in the l^{th} reaction, $kmol\ i/(m^3 \cdot s)$

For the reversible reaction considered in the model ($CO + 0.5O_2 \rightleftharpoons CO_2$) the following Arrhenius molar rate of the ith species creation can be written [124]:

$$r_i = (\nu''_i - \nu'_i) \cdot (k_f \cdot \prod_{j=1}^{N_j} (C_j)^{\eta'_j} - k_b \cdot \prod_{j=1}^{N_j} (C_j)^{\nu''_j}) \tag{8.24}$$

where:

ν''_i and ν'_i - the ith species stoichiometric coefficient for product and substrate, –

ν''_j - the jth species stoichiometric coefficient for product, –

η'_j - the jth species rate exponent for reactant, –

C_j - the jth species molar concentration, $kmol\ j/m^3$

k_f - forward reaction rate constants, $\frac{kmol\ i \cdot m^{0.75}}{kmol\ CO \cdot kmol\ O_2^{0.25} \cdot s}$

k_b - backward reaction rate constants, $kmol\ i/(kmol\ CO_2 \cdot s)$

The reaction rate constants are calculated as $k_f = A_f \cdot exp(-E_a/(R \cdot T))$ and $k_b = A_b \cdot exp(-E_a/(R \cdot T))$, where A_f and A_b are pre-exponential factors for forward and backward reactions.

The mass sources ($S_{g\,i}$) in Equation 8.17, which are due to heterogeneous reactions are calculated for CO_2, O_2 and CO using the following equations:

$$S_{g\,CO2} = M_{CO2}/M_C \cdot ((2 \cdot \gamma - 1) \cdot c_{r\,oxy} - c_{r\,B}) \tag{8.25}$$

$$S_{g\,O2} = -M_{O2}/M_C \cdot \gamma \cdot c_{r\,oxy} \tag{8.26}$$

$$S_{g\,CO} = M_{CO}/M_C \cdot ((2 - 2 \cdot \gamma) \cdot c_{r\,oxy} + 2 \cdot c_{r\,B}) \tag{8.27}$$

8.3.4 Mass conservation equation for gas phase

For the gas phase in Interior-1 (see Fig.8.2) the following mass conservation equation is used:

$$\frac{\partial(\rho_g)}{\partial\tau} + \nabla \cdot (\vec{w} \cdot \rho_g) = 0 \tag{8.28}$$

In case of mass balance of individual species in Interior-1 the following equation is solved for each species excluding nitrogen:

$$\frac{\partial(\rho_g \cdot g_i)}{\partial\tau} + \nabla \cdot (\vec{w} \cdot \rho_g \cdot g_i) = \nabla \cdot (\rho_g \cdot D_{g\,i-mix} \cdot \nabla g_i) + R_i \tag{8.29}$$

8.3.5 Momentum conservation equation for porous medium

For porous medium (Interiors -2 and -3) the momentum equation is not needed since there is no gas flow inside the particle.

8.3.6 Momentum conservation equation for gas phase

Momentum conservation equation for Interior-1 (gas volume) reads:

$$\frac{\partial(\rho_g \cdot \vec{w})}{\partial t} + \nabla \cdot (\vec{w} \cdot \vec{w} \cdot \rho_g) = -\nabla \cdot p + \nabla \cdot \bar{\bar{\tau}} + \vec{F} \tag{8.30}$$

where:

$\bar{\bar{\tau}}$	- stress tensor,	N/m^2
$\vec{F}$	- vector of external body forces,	N/m^3

In the above equation the time-dependent acceleration and convective acceleration of momentum appear on the left hand side and pressure gradient term, stress term associated with viscous forces and other forces on the right hand side.

8.3.7 Other dependencies used in the model

The variation of the porosity with time and space has also been implemented into the model; porosity (ϵ) is calculated as $\epsilon = 1 - \rho_{app}/\rho_{true}$. The only one parameter in this equation, which varies with burnout is the apparent density of char (ρ_{app}), which is calculated using the following relationship:

$$\rho_{app} = m_c/V_c \tag{8.31}$$

where:

m_c	- solids mass of individual cell	kg
V_c	- volume of individual cell	m^3

Mass of individual cell as a function of time is computed using:

$$m_c = \rho_{app}(\tau - \Delta\tau) \cdot V_c - (c_{r\ oxy} + c_{r\ B}) \cdot V_c \cdot \Delta\tau \tag{8.32}$$

where:

$\Delta\tau$	- time step	s

In order to monitor parameters like char burnout, porosity, apparent density, average pore radius and char conversion rates, the User Define Memory of these parameters have been included into the software. The char burnout has been defined according to $X = m_C/m_{C0}$. Average pore radius at any stage of combustion is calculated as [31]:

$$d_{pore\ av} = 4 \cdot \epsilon \cdot \tau_{pore}^{0.5}/S_V \tag{8.33}$$

Assuming that the pore tortuosity does not vary during combustion, the increase in average pore radius is mainly caused by the change of internal surface area, described by Random Pore Model (see Equation 6.11).

8.3.8 Summary of the input variables and parameters used in the model

Table 8.2 shows all values of parameters, which have been implemented into the mathematical model.

TABLE 8.2: Input variables for the 2D char combustion model

Symbol	Unit	Value
A_b	$kmol\ i/(kmol\ CO_2 \cdot s)$	$5.000E+08$*
A_f	$\frac{kmol\ i \cdot m^{0.75}}{kmol\ CO \cdot kmol\ O_2^{0.25} \cdot s}$	$2.239E+12$*
A_{int}	m/s	$4.04E+03$
$A_{int}(B)$	m/s	$2.77E+03$
D^0_{CO-CO2}	m^2/s	$1.552E-05$
D^0_{CO2-O2}	m^2/s	$1.532E-05$
D^0_{O2-CO}	m^2/s	$2.058E-05$
D^0_{O2-N2}	m^2/s	$2.056E-05$
D^0_{N2-CO}	m^2/s	$2.044E-05$
D^0_{N2-CO2}	m^2/s	$1.547E-05$
E_a/R	K	20447*
$E_{a\ int}/R$	K	15450
$E_{a\ int}(B)/R$	K	26177
g_{ash}	$kg\ ash/kg\ char$	0.14
g_C	$kg\ C/kg\ char$	0.86
$\Delta h_r(B)$	$kJ/kg\ C$	$14.225E+3$ [125]
$\Delta h_r(CO)$	$kJ/kg\ C$	$9.212E+3$ [119]
$\Delta h_r(CO_2)$	$kJ/kg\ C$	$32.796E+3$ [119]
M_C	$kg\ C/kmol\ C$	12
M_{CO}	$kg\ CO/kmol\ CO$	28
M_{CO2}	$kg\ CO_2/kmol\ CO_2$	44
M_{N2}	$kg\ N_2/kmol\ N_2$	28
M_{O2}	$kg\ O_2/kmol\ O_2$	32
S_{V0}	m^2/m^3	$3.11E+7$
ϵ_0	m^3 gas / m^3	0.286
ϵ_{p-pw}	–	0.8
ψ	–	2.28
ρ_{true}	$kg/m^3\ solid$	1628
τ_{pore}	–	1.2

*Original Fluent value for the $CO + 0.5O_2 \rightleftharpoons CO_2$ reaction

8.4 Simulation results

For the selected numerical grid consisting of circa 50 000 cells, the transient calculations have been found to be very time consuming. At the beginning of the calculations as short time step as 10^{-6} s has been used. The maximum possible time step, which allowed for stable calculations has been found to be $4 \cdot 10^{-5}$ s. The calculations for one second last in reality between one day and dozen days. This is the reason, why the results for the first 120 s are only shown in this Section. Nevertheless, the particle burnout at 120 s has exceeded 50%, thus changes of many parameters are already visible and can be compared to data obtained though measurements.

8.4.1 Velocity profiles

Few seconds after initialization of the calculations the flow field has been formed, which remains almost unchanged during the combustion process. The Reynolds number at 1069 K gas temperature is around 150, thus the laminar flow field is expected. Figure 8.4 shows the axial velocity profiles (top image) and velocity streamlines (bottom image) at instant of 120 s. The velocity inside the particle is zero (visible as half of the sphere marked by light blue color - top image). Because the flow is directed from left to right, on the right hand side of the particle the stagnation and recirculation regions are observed and marked as dark blue region in the top image and empty region in the bottom image. The influence of the flow on combustion progress is shown later in this section.

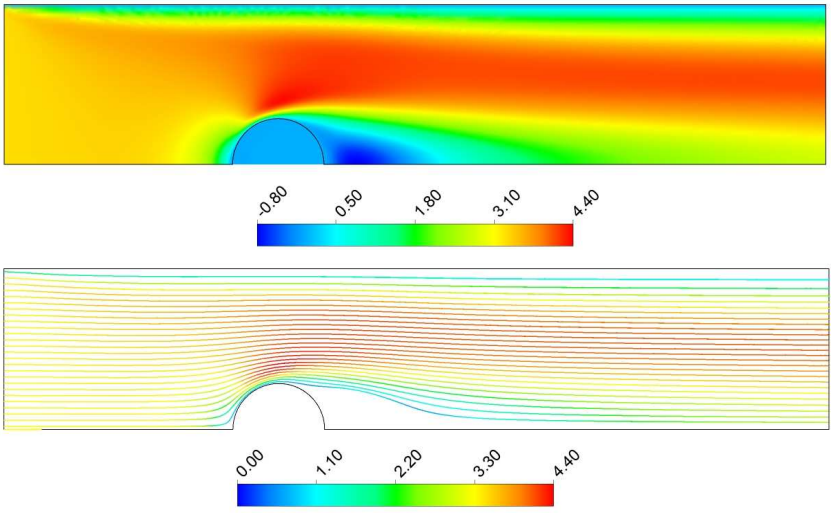

FIGURE 8.4: Axial velocity profiles (top figure) and velocity streamlines (bottom figure) at 120 s; scale in m/s

8.4.2 Temperature profiles

The temperature profiles and isotherms at 30 s, 60 s, 90 s and 120 s after initialization of the calculations are shown in Fig. 8.5 and in Fig. 8.6 respectively. The highest temperature at 30 s time has been found on the windward side of the particle (the particle left side). This is caused by the high reactions rates of carbon oxidation with O_2 and carbon monoxide oxidation. The occurrence of these reactions especially at this side of the particle is a result of quicker particle heating up caused by convection from 300 K initial temperature to the ignition temperature. At this time, however, the leeward part of the particle is still relatively cold (around 1150 K), therefore a steep temperature gradient in the particle is found at 30 s instant (see Fig. 8.6). At 60 s and 90 s the reactions rates increase causes that temperature reaches around 1550 K at the

left hand side of the particle. The heat is then transferred to the center and the right hand side of the particle. As it is shown in Fig. 8.5, at 120 *s* instant the high temperature area has developed toward the upper part of the particle (see dark orange ring in Fig. 8.5). As it can be noticed in Fig. 8.6 the temperature gradient inside the particle is large at any instant. Nevertheless, temperature gradient in the particle unreacted core is decreasing with combustion progress (circa 300 *K* at 30 *s* instant and around 200 *K* at 120 *s* instant).

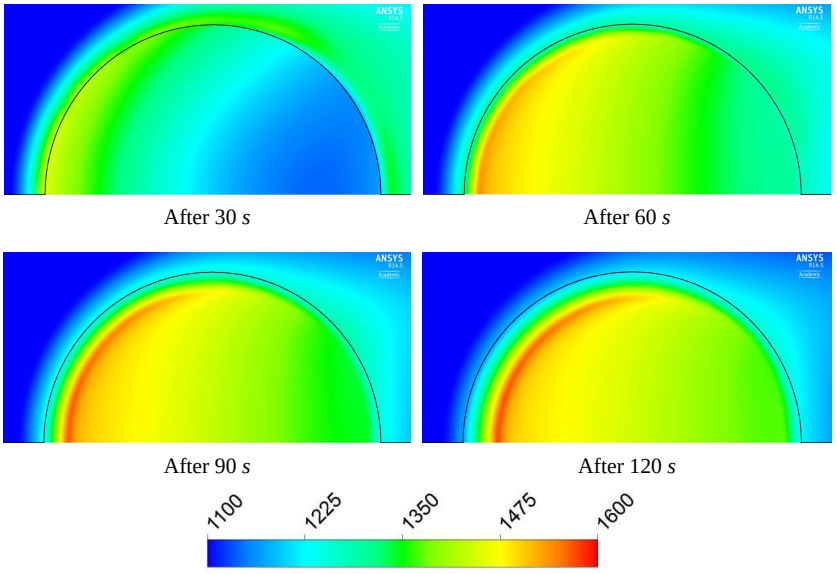

FIGURE 8.5: Temperature profiles of the particle and its neighborhood at 30 *s*, 60 *s*, 90 *s* and 120 *s*; scale in *K*

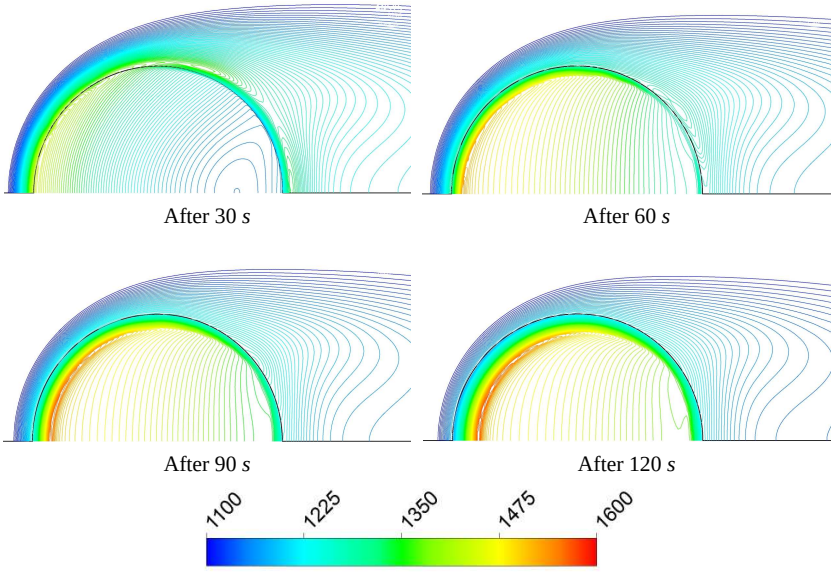

FIGURE 8.6: Temperature isotherms in the particle and in its neighborhood at 30 *s*, 60 *s*, 90 *s* and 120 *s*; scale in *K*

8.4.3 Species profiles

The temperature profiles are associated with species production and destruction rates, which in turn influence species profiles at each considered instant. Figures 8.7, 8.8 and 8.9 show mass fractions of oxygen, carbon monoxide and carbon dioxide respectively. As shown in Fig. 8.7 the oxygen is not present inside the particle at any shown instant. Oxygen is consumed both in fast heterogeneous reaction of carbon with oxygen and in homogenous reaction with CO, which is produced in the reaction of carbon with oxygen and in the Boudouard reaction. At temperatures, which are present in the particle, the primary product of carbon oxidation with O_2 is mainly carbon monoxide (around 96% for 1400 K - see Eq. 6.3). Carbon monoxide molecules, which diffuse from the heterogeneous reaction front to the outer surface of the particle, react with oxygen, present in the particle boundary layer or in ash layer, giving carbon dioxide. Therefore no carbon monoxide is present in the gas surrounding the particle (see Fig. 8.8). Carbon monoxide is only present inside pores of the unreacted char particle.

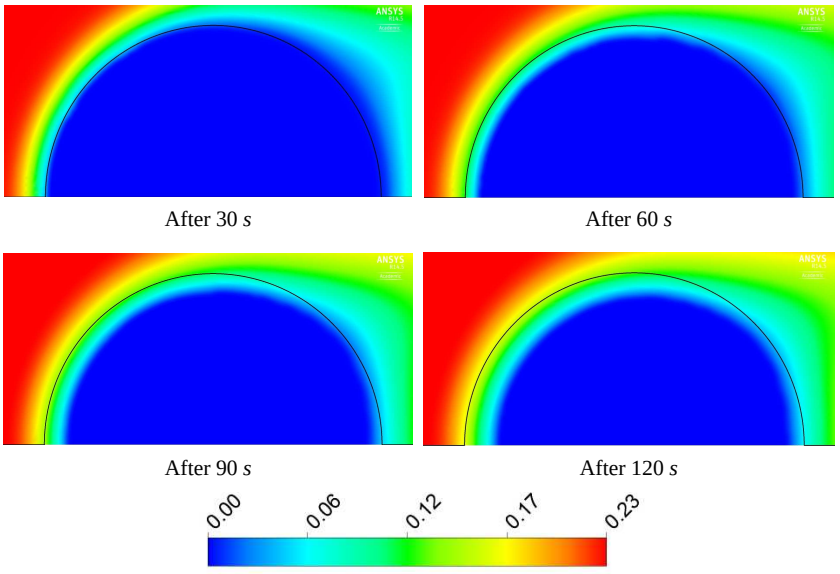

FIGURE 8.7: Oxygen mass fraction profiles of the particle and its neighborhood at 30 s, 60 s, 90 s and 120 s

Carbon dioxide molecules, produced mainly in CO oxidation, leave the particle or diffuse toward the unreacted particle core, where at sufficiently high temperatures the reaction of carbon with CO_2 occurs, as shown in Fig. 8.9. The particle center is almost carbon dioxide free, giving the outline of the high-CO_2 content ring, which surrounds the unreacted char core. This is more visible at later stages of combustion (from 60 s onwards), when the particle temperature is higher (see Fig. 8.5 for comparison) and the Boudouard reaction progresses faster. It is also seen that the diameter of the high-CO_2 content ring shrinks with time due to shrinkage of the unreacted particle core.

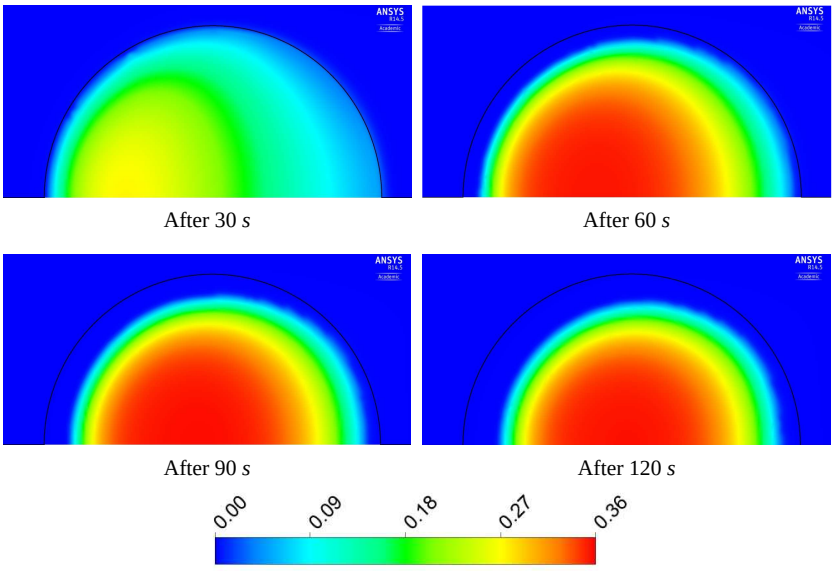

FIGURE 8.8: Carbon monoxide mass fraction profiles of the particle and its neighborhood at 30 *s*, 60 *s*, 90 *s* and 120 *s*

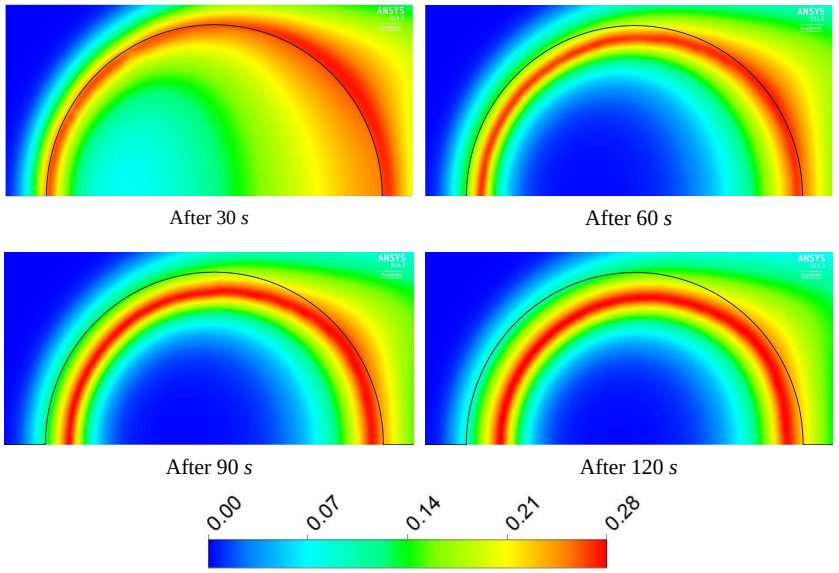

FIGURE 8.9: Carbon dioxide mass fraction profiles of the particle and its neighborhood at 30 *s*, 60 *s*, 90 *s* and 120 *s*

8.4.4 Char burnout and porosity profiles

The unreacted particle core shrinkage is visible in Fig. 8.10, which shows char burnout at four instants. At the first instant, only a thin layer of carbon on the particle surface is totally burned (marked with red color). Later stages of combustion are shown at instants of 60 s, 90 s and 120 s. The particle burnout profiles are not symmetric with respect to particle center. The windward side of the particle burns quicker, which is associated with flow of fresh gas at the windward side. The layer of partially burned particle (light blue color) widens with time. This is associated with increasing importance of Boudouard reaction at higher temperatures. Carbon dioxide, which diffuses toward the particle center, does not react inside a thin char layer, but rather inside a large part of volume of unreacted core.

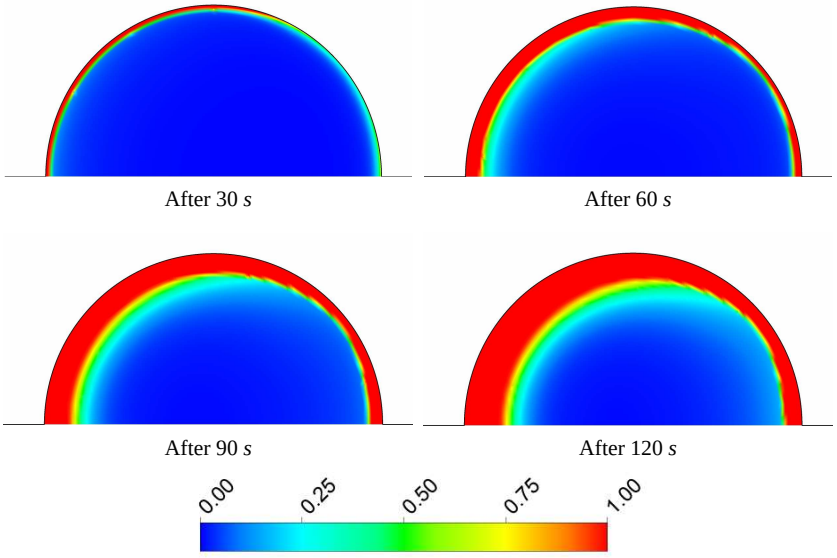

FIGURE 8.10: Char burnout profiles at 30 s, 60 s, 90 s and 120 s

Since porosity is directly dependent (through solids mass decay) on char burnout, the porosity profiles are similar to the char burnout profiles (see Fig. 8.11). The porosity changes between 0.286-0.9, while the char burnout between 0-1.

8.4.5 Char conversion rates and reactions rates

The time dependence of volume averaged char conversion rates, which are the results of the two considered heterogeneous reactions ($C + \gamma O_2 \Rightarrow (2\gamma - 1)CO_2 + (2 - 2\gamma)CO$ and $C + CO_2 \Rightarrow 2CO$) are shown in Fig. 8.12. At the beginning of the process, when the particle temperature is still relatively low (see Fig. 8.5), the carbon oxidation with oxygen (marked with red circles in Fig. 8.12) is practically the only reaction occurring. The Boudouard reaction proceeds with a very low rate due to too low temperatures. At instant of around 30 s, the

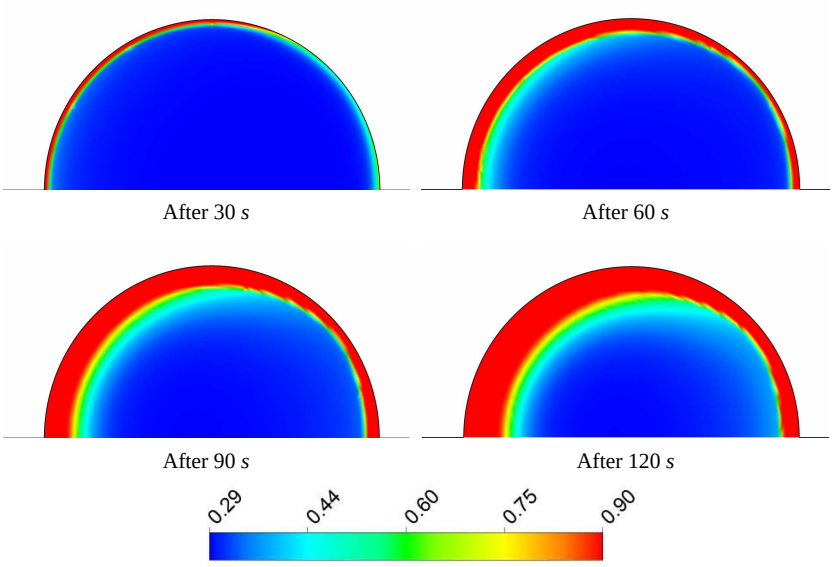

FIGURE 8.11: Porosity profiles at 30 *s*, 60 *s*, 90 *s* and 120 *s*

Boudouard reaction (marked with blue squares) begins to contribute to the char conversion, since the left part of the particle is heated to 1400 *K* (see Fig. 8.5). At this time the maximum carbon conversion rate is observed (see empty triangles). From this time onwards, the conversion rate due to the $C + \gamma O_2 \Rightarrow (2\gamma - 1)CO_2 + (2 - 2\gamma)CO$ reaction decreases significantly. The decrease is mainly associated with oxygen unavailability (see Fig. 8.7), since O_2 is consumed in the homogenous reaction. On the other hand, carbon dioxide is produced in the homogenous reaction, which reacts more and more intensively with carbon, due to temperature increase. At some instant (around 60 *s*) the carbon conversion rate, due to reaction of carbon with O_2, is equal to carbon conversion rate, which is the result of the Boudouard reaction. From this time onwards the Boudouard reaction prevails. The maximum char conversion rate for the Boudouard reaction has been found at circa 90 *s*. From this time onwards, the conversion rates due to both reactions decrease slightly, which is associated with the shrinking unreacted core volume, thus decreasing the total area available for reactions to occur. The decrease is also partially related to the ash layer widening, which makes the the oxygen diffusion path longer.

Energy to the endothermic Boudouard reaction is provided, at later stages of the particle combustion (from around 60 *s*), mainly by the homogenous reaction ($CO + 0.5O_2 \rightleftharpoons CO_2$). The change of heat release with time, due to this reaction, is shown in Fig. 8.13. In order to show, where the reaction takes place, the heat release has been summed up separately for the gas phase (Interior-1 - marked with blue squares) and the particle volume (Interiors -2 and -3 - marked with red spheres). In Interior-1 the maximum heat release rate is observed at 20 *s* instant and the amount of heat is several times larger than the heat generated due to the homogenous reaction inside the particle pores. Between 20 *s* and 30 *s* the shift of heat release rate has been indicated, which results in much higher a heat release rate inside the particle pores in comparison to gas

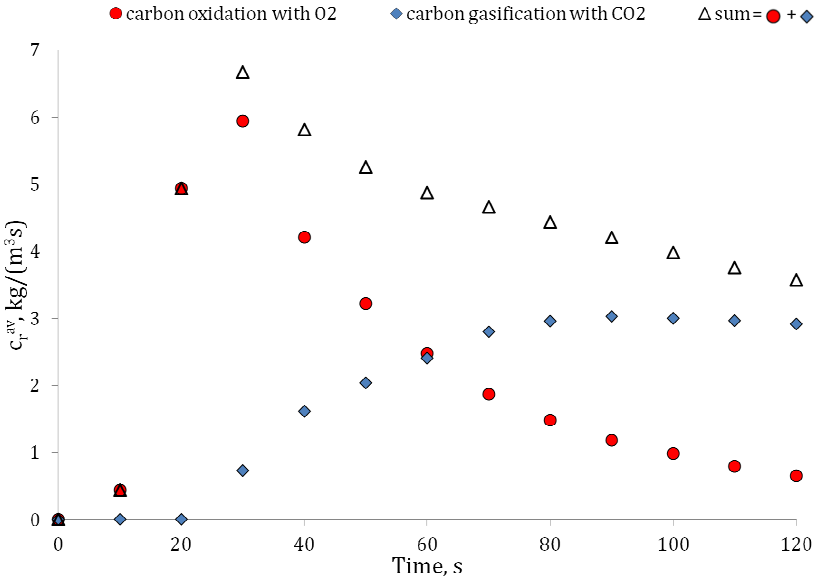

FIGURE 8.12: Modeled char conversion rates due to heterogeneous reactions

phase at 30 *s* instant. The maximum heat release rate, similarly to heterogeneous reactions (see Fig. 8.12), has been obtained at 30 *s* instant. From this instant onwards the total heat release rate, due to the homogenous reaction, decreases. From around 70 *s* onwards, the heat release is almost entirely generated inside the particle pores (in the ash layer). This means that CO is burned within the particle volume, what could be also seen in Fig. 8.8.

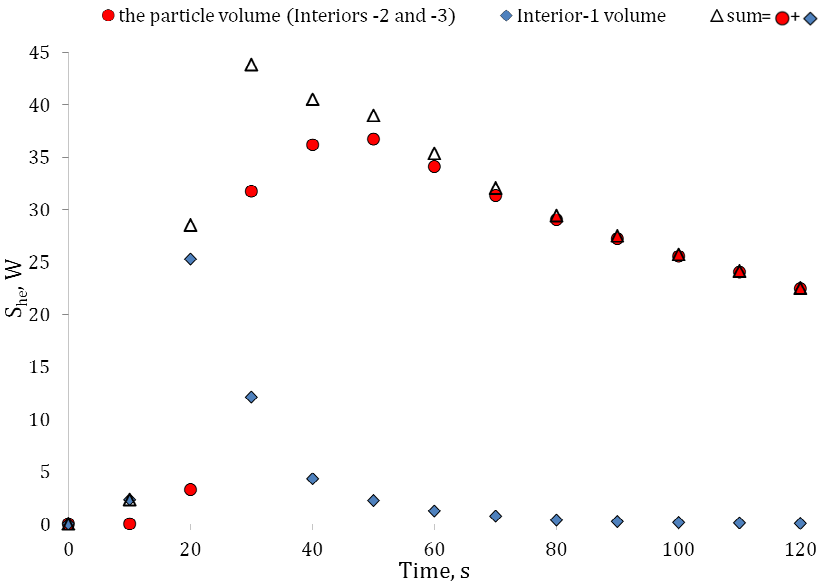

FIGURE 8.13: Modeled heat release rate due to homogenous reaction ($CO + 0.5O_2 \rightleftharpoons CO_2$)

8.5 Model validation

The 2D model validation is carried out using the experimental run no. 6, for which the particle initial mass and diameter is shown in Table 4.3 and experimental procedures and conditions are described in Chapter 4. Additionally, the 2D model predictions and experimental data are compared to the 0D Shrinking Core Model predictions (see Section 7.2.2 for the 0D SCM model description).

8.5.1 Particle mass loss, burnout and conversion rates

Figure 8.14 shows the particle mass loss obtained experimentally and using the 2D model and the 0D SCM. The 2D model predictions are marked with red circles, the experimental data (run no. 6) with blue squares and the 0D SCM predictions are represented by solid line. The mass loss predicted by the 2D model is well correlated with run no. 6 from the $30 - 40$ s instant onwards. The experimental data (blue squares) have been shifted 10 seconds forward in order to match the experimental and the modeling data at around 40 s. This has been done due to the fact that initial mass loss of the particle in run no. 6 is associated with moisture and residual volatiles release. These processes are not taken into account in the 2D model and the 0D SCM. The mass loss between 30 s and 120 s obtained in the measurements is 0.0492 g, while the 2D model calculated 0.0475 g value. The data obtained by the 0D SCM has been calculated assuming that only the $C + O_2 \rightarrow CO_2$ reaction takes place. The 2D model predictions are very well correlated with the 0D SCM predictions. The relative difference in mass loss between both models predictions (referred to the 2D model predictions), for the time period of $0 - 120$ s, is less than 3%.

Figure 8.15 shows a peak of experimentally-obtained conversion rates for the first 30 s of combustion. These high conversion rates are mainly associated with release of moisture and volatiles remains in the char particle. Due to this reason the experimental and the modeling data are not correlated. However, the data obtained using the 2D model (red spheres), the 0D SCM (empty triangles) and experimental data (blue squares) are compatible for the period of $30 - 120$ s. The calculated relative difference between char conversion rates obtained using the 2D model predictions and experimental data is less than 4%, while around 2% of relative difference between the 0D SCM predictions and the experimental data (from run no. 6) has been found (time between $30 - 120$ s has been taken into account).

In case of char burnout, the 2D model predictions are not so well correlated with the measured data as in case of mass loss. The 2D model predictions are about 30 s delayed in comparison with char burnout obtained in the experiments. For the time period of $30 - 120$ s,

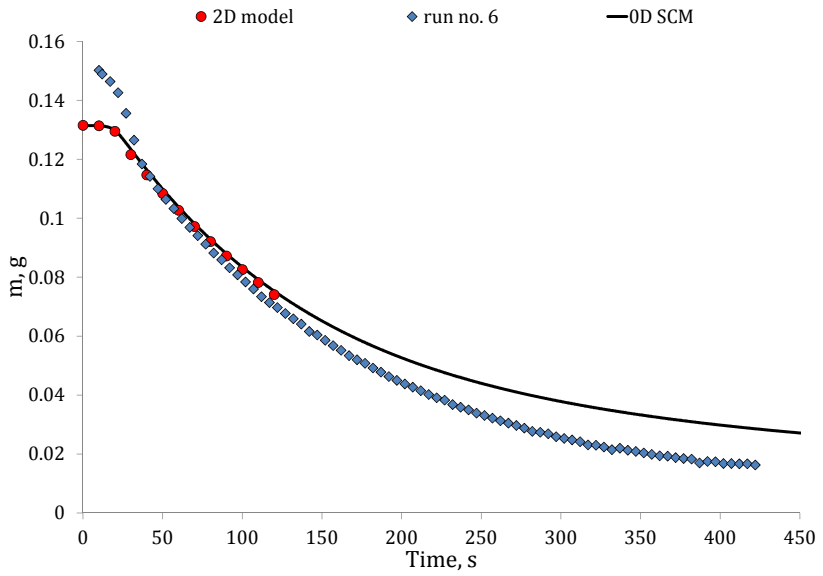

FIGURE 8.14: Comparison of the particle mass loss obtained experimentally (run no. 6 - see Table 4.3), using the 2D model and the 0D SCM calculations, where C + O_2 → CO_2 reaction is considered only

the burnout rate obtained by the 2D model is well correlated with the experimental data (around 14% of relative difference between char burnout rates is found).

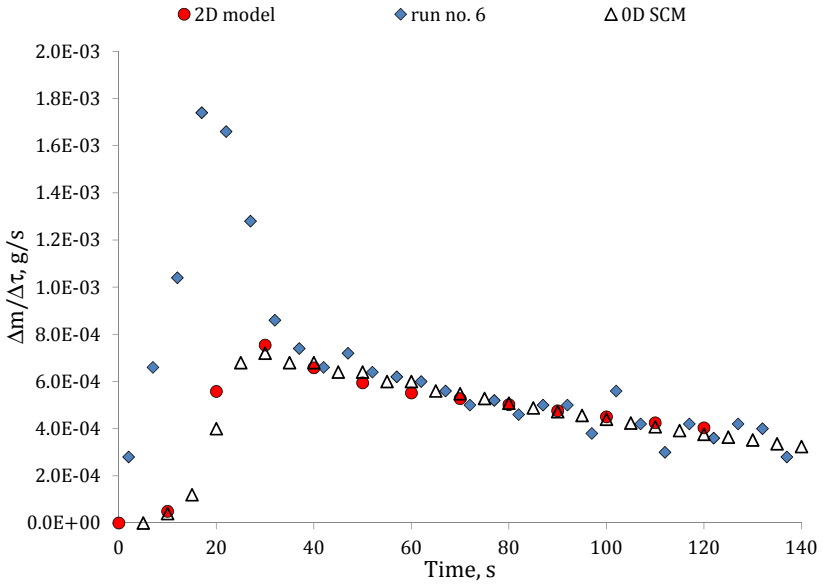

FIGURE 8.15: Comparison of char conversion rates obtained using the 0D SCM (C + O_2 → CO_2 reaction is considered only), using the 2D model and experimentally (run no. 6 - see Table 4.3)

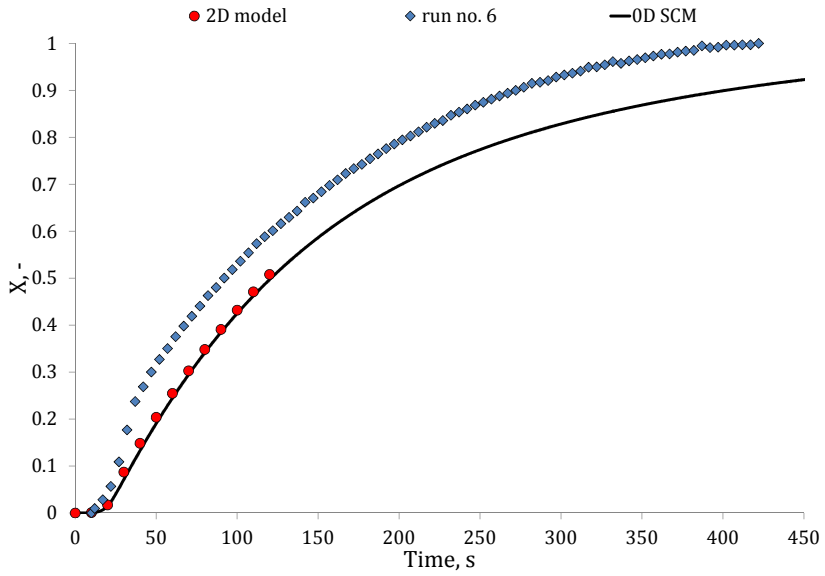

FIGURE 8.16: Comparison of the particle burnout obtained experimentally (run no. 6 - see Table 4.3), using the 2D model and the 0D SCM calculations, where C + O_2 → CO_2 reaction is considered only

8.5.2 Particle temperature

Comparison of the particle temperatures obtained using the 2D model and measured values using the IR camera is presented in Fig. 8.17. The calculated particle temperature obtained using the 0D SCM has also been included in the graph. The experimental data is represented by average surface temperature (blue squares) and maximum surface temperature (blue crosses), both measured by the IR camera facing the leeward side of the particle. From the 2D model calculations three temperatures have been estimated. The first one is the averaged particle surface temperature of the leeward hemisphere (red squares). The second calculated temperature at any instant is the volume-averaged particle temperature (red triangles) and the third represents the maximum calculated temperature in any cell within the particle volume (red spheres). The 0D SCM-calculated temperature changes only with combustion time in the entire particle volume, thus, calculation data is represented by the black solid line only.

Very good agreement between the average surface temperature calculated using the 2D model and data obtained experimentally have been found until 120 *s* of combustion time. Also the maximum registered surface temperature is well correlated with the 2D model values for the volume-averaged temperature, especially from around 70 *s* onwards. The third calculated temperature, using the 2D model, represents the maximum cell temperature. This temperature is not correlated with any measured value, since the maximum calculated temperature occurs on the windward side of the particle (see Fig. 8.5), which could not be seen by the IR camera.

The 0D SCM temperatures predictions are also well correlated with the average particle surface temperature until 120 *s* of combustion time. Calculated low temperature through the

0D model at later stages of combustion (after 120 *s*), are the reason for increasing difference in mass loss in comparison to the measured data (see Fig. 8.14). This is because the char conversion has turned from diffusion to kinetic controlled. This will probably be not observed for the 2D model, since the unreacted particle core temperature will be different to ash layer temperature, thus probably allowing the reactions to proceed with similar speed as they are at 120 *s* instant. Therefore, the char conversion rates for the 2D model will probably be still dependent on diffusion rather than kinetics and obtained mass loss (after 120 *s*) will be larger than in case of the 0D SCM.

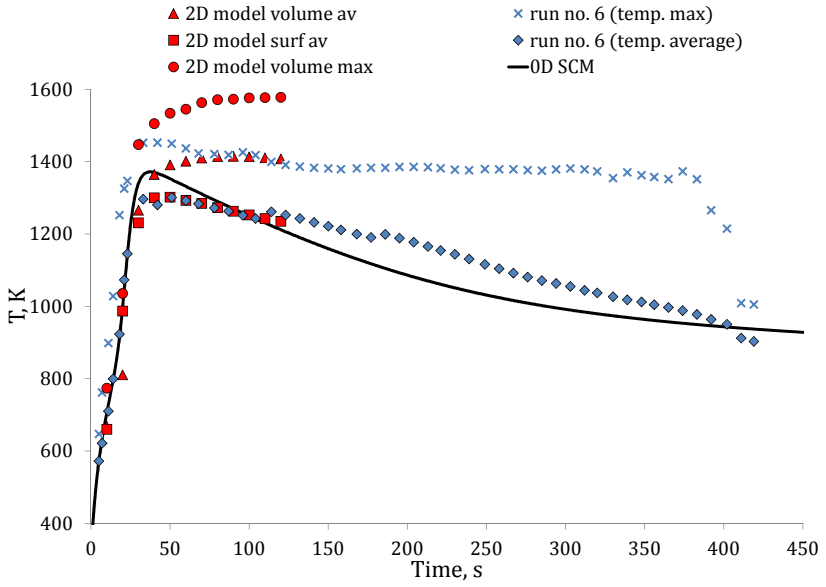

FIGURE 8.17: Comparison of the particle temperatures obtained experimentally (run no. 6 - see Table 4.3), using the 2D model and obtained from the 0D SCM calculations in which the C + $O_2 \rightarrow CO_2$ is the only reaction considered

8.6 Summary

In the present chapter the 2D axisymmetric model of single char particle combustion has been described. The model has been created in Ansys Fluent software and the calculation outcomes from this model have been validated using experimental run no. 6 (see the GTB experiments - Chapter 4). The model is able to simulate the GTB experiments (combustion of particles with high ash content) in such a way that the char combustion at any instant is represented by 2-dimensional fields of variables.

Obtained data till the 120 *s* instant show that parameters like temperature, char burnout, porosity, species mass fractions change locally in the particle. Moreover, a large temperature gradient in the particle has been found at any instant of combustion. Much higher particle temperature has been found from the windward side of the particle, which initially has been caused

by more intense convective heat transfer and later by much higher combustion rate of heterogeneous and homogenous reactions. It has been found that carbon monoxide is burned initially within the particle boundary layer. At later stages of combustion (from around 60 *s* onwards) almost all carbon oxide is burned inside the pores of the particle ash layer. The Boudouard reaction has been found to have a strong influence on char burnout when the particle reaches a sufficiently high temperature. From the combustion time of around 60 *s* onwards the Boudouard reaction determines the char conversion rate and it is faster than the carbon oxidation with oxygen. This is due to unavailability of oxygen molecules, which are consumed in homogenous reactions and due to carbon dioxide abundance on the unreacted particle core surface.

The comparison of the modeled outcomes with the experimental data shows generally a good correlation in case of mass loss, char burnout and the particle temperature, which proves the accuracy of the assumptions and correctness of the input data, obtained in the experimental studies and implemented into the model. The insufficient correlation between measured and modeled data has been found at the beginning of the combustion process, which could be explained by moisture and residual volatiles release from the particle, which have not been considered in the model. The difference in the model predictions and experimental data can be also explained by the non-spherical particle used in run no. 6, which has larger external surface area than the ideal modeled sphere. Larger surface area enhances heat transfer to the particle, thus higher char conversion rates are expected especially at the beginning of the combustion process.

Chapter 9

Conclusions

This work presents a comprehensive description of combustion phenomena of char particles, with dedication to fluidized bed combustion technology. This technology has many advantages, therefore a need of its further development exists.

In order to understand the complex phenomena, which are present during char combustion, the first research step has been undertaken to estimate the intrinsic kinetic constants for carbon oxidation with oxygen and gasification using carbon dioxide. To this end the thermogravimetric analysis has been applied. The adequate procedure has to be applied in the thermogravimetry in order to make sure that carbon conversion rate is not depended on diffusion rate of reactants to the sample surface and in particles pores. The influence of diffusion has been minimized by applying relatively low final temperatures in the device (max 500°C in the case of char oxidation with O_2 and max 950°C in the case of char gasification with CO_2), by using a relatively small sample, by grinding the char to particles smaller than 0.25 *mm* and by using the shallow crucible. Applying all mentioned procedures allow for obtaining pure kinetic-controlled char conversion rates. The influence of the char preparation method on char conversion rates has been also studied in the TGA. It has been found that devolatilization rate has significant impact on char reactivity since two kinds of char have been studied. The first char type (GTB-char) has been prepared in the special stand, which allows for a fast heating of few millimeter size coal particles and the second char type has been devolatilized in standard TGA conditions i.e. at 10 K/min heating rate (TGA-char). It has been found that lower heating rates during coal devolatilization decreases char reactivity.

To estimate intrinsic kinetic constants the char morphology has to be also known. The mercury porosimetry has been used for estimation of char porosity and internal specific surface area[1]. Both the GTB-char and the TGA-char have been investigated. It has been found that the TGA-char has much lower porosity and internal specific surface area in comparison to the

[1]Measurements have been carried out by Anna Pajdak from the Częstochowa University of Technology

GTB-char. This means that higher heating rates promote formation of small pores (meso- and micropores), which are responsible for specific surface area development and also large pores (macropores), which are responsible for higher porosity. From thermogravimetric and mercury porosimetry studies it is possible to see that carbon conversion rates are dependent on thermal history of char (preparation procedures of char). Lower carbon conversion rates for the TGA-char, in comparison with the GTB-char, can be explained by lower porosity and specific surface area. Porosity affects transport of reacting gas to the particle center and specific surface area is associated with the total area available for reactions. The other possible explanation of the lower conversion rates for the TGA-char could be that during long preparation procedure of this char in the TGA, the char undergoes annealing, which decreases its reactivity. Thus, the char annealing, slower gas diffusion in pores and smaller surface area available for reactions are responsible for a lowering the TGA-char reactivity.

The experimental study carried out using the TGA allowed for the Arrhenius parameters estimation. Because isothermal conditions have been applied in this study, the evaluation of kinetic constants is rather simple and straightforward. The Random Pore Model has been applied in the calculations, which allows for variation of specific surface area with char burnout. The Arrhenius constants for char oxidation with oxygen have been determined for both the TGA-char and the GTB-char in two temperature regions (lower temperatures between 350°C-500°C and higher temperatures between 750°C-950°C). At the higher temperatures, the evaluated Arrhenius constants are substantially different in comparison to these obtained in the lower temperatures region. In the higher temperatures the char conversion rates do not depend on reactions rates, but rather on the diffusion rate both to the sample surface and inside particles pores. Therefore, the activation temperature and pre-exponential constants for higher temperature region are around ten times lower and by a factor of 10^7 lower than these values obtained for lower temperature region (350°C-500°C), respectively. For the higher temperature region, the values obtained do not reflect the true kinetic constants, therefore they should not be used in combustion models. The Arrhenius constants have been also estimated for the Boudouard reaction of carbon with carbon dioxide. In this case only the GTB-char has been used, because it is expected that this char has similar physical properties to the char, which is obtained during devolatilization of coal particles in FBBs. The values of activation temperatures obtained for the GTB-char oxidation with oxygen at 350°C-450°C temperatures and for the GTB-char gasification with carbon dioxide at 800°C-950°C are 15450 K (for C + γ O_2 $\Rightarrow$ (2 γ-1) CO_2 + (2-2 γ) CO reaction) and 26177 K, respectively. These values are comparable to some data found in the literature.

In order to investigate the process of a single coal/char combustion the new test rig has been built (GTB test rig). The rig allows for continuous measurement of mass loss and surface temperature of the burning particle. Experimental conditions have been chosen to reflect, to some extent, these which occur during coal combustion in fluidized bed boilers. By carrying out

experiments with different initial char particle masses (range of $0.06-0.2\ g$) it has been observed that the initial shape of the char particle has negligible effect on combustion time. Generally, the larger initial mass of the char particle, the longer is the combustion time. Some deviations from this rule can be explained by differences in physical and chemical properties from particle to particle and especially by high-ash content and its compact structure, which have been found for some of the particles studied.

In this thesis several zero-dimensional models are being developed to be used in conjunction with CFD boiler models. The zero-dimensional shrinking core model (SCM) and the shrinking particle model (SPM) have been created and tested, taking various models simplifications into account. The only heterogeneous reaction considered in each model is either: C + $O_2 \rightarrow CO_2$ or C + $O_2 \rightarrow 2CO$ or C + γ $O_2 \Rightarrow$ (2 γ-1) CO_2 + (2-2 γ) CO. Comparison of results obtained by these models with measurements, performed using the GTB test rig, allows for determination of model accuracy and applicability range. From performed analysis it can be concluded that the most suitable 0D model for the fluidized bed combustion is the shrinking particle model, based on C + $O_2 \rightarrow CO_2$ reaction. This model has the smallest relative difference (8.3%) in char conversion rates between data obtained through measurements and through calculations. Moreover, the predicted particle temperatures match well the measured maximal surface temperature of the particle, for most of the combustion time. In the SPM the ash layer is removed from the particle surface, which is compatible with real fluidized bed conditions, where particles collisions are likely to remove the ash layer formed during combustion. The second considered model (SCM) may be useful in a CFD-based model of grate boilers. Due to the assumption of the particle temperature uniformity, the SCM does not represent well the experimental data at later stages of combustion process, due to too low temperature even if the C + $O_2 \rightarrow CO_2$ reaction is used. A better fit to the experimental data has been obtained, for entire combustion time, when only diffusion through the particle boundary layer and in the ash layer is simulated.

In order to simulate the GTB experiments in such a way that the char combustion at any instant is represented by two-dimensional fields of variables, the two-dimensional axisymmetric model has been created. The kinetic parameters of the C + γ $O_2 \Rightarrow$ (2 γ-1) CO_2 + (2-2 γ) CO reaction and the Boudouard reaction and the char physical properties, which have been obtained in the experimental parts of the thesis, have been implemented into this model. The 2D model has been validated using experimental run no. 6 (see Table 4.3), which represents the combustion phenomena of high-ash particles. The run no. 6 has been chosen due to the model assumption of the constant particle diameter during combustion. Because of time-consuming calculations, the first 120 *s* of combustion time has been shown in this thesis only. Model predictions indicate that parameters like temperature, char burnout, porosity, species mole fractions change locally in the particle. Large temperature gradients have been found at any instant of combustion in the particle. Much higher particle temperatures have been predicted by the model on the windward

side of the unreacted particle core. It has been found that carbon monoxide is burned within the particle boundary layer and in the pores of the ash layer. The model predictions show that the Boudouard reaction has strong influence on char burnout. Unavailability of oxygen molecules, from the combustion time of around 60 *s*, causes that the carbon conversion rate due to the Boudouard reaction is faster than carbon conversion rate, which is a result of char oxidation reaction with O_2. Strong influence of the Boudouard reaction is also a consequence of carbon dioxide abundance on the unreacted particle core surface. Comparison of the data obtained from calculations using the 2D model with the experimental data indicates generally a good correlation in case of mass loss, char burnout and the particle temperature. The insufficient correlation between the measured and modeled data has been found only at the beginning of the combustion process. This discrepancy can be explained by moisture and residual volatiles release from the particle which are not considered in the model.

The main achievement of this thesis is the development of a methodology (a series of actions) needed for calculating conversion rates of millimeter size char particles. The methodology begins with TGA measurements of kinetically-controlled char conversion rates, which is followed by determination of particle morphology. On the basis of such information, zero-dimensional or multi-dimensional models can be developed depending on what is needed.

9.1 Recommendations for further work

Almost each part of the presented thesis could be improved. The following points list some of the most important suggestions for further work:

- In case of the thermogravimetric analysis it could be beneficial to preform experiments of the TGA-char and the GTB-char combustion in O_2 for a few more final temperatures in the kinetically-controlled temperature range. It could be informative to perform experiments for the TGA-char gasification with CO_2 and also to carry out experiments for more than three final temperatures. This could improve the accuracy of obtained Arrhenius constants as well as would add additional answers for the question about the influence of char preparation method on char gasification rates. By performing experiments with the same temperature but with different mole fractions of oxygen in the TGA it would be possible to determine reactions orders with respect to oxygen and carbon dioxide;
- It could be beneficial for more accurate estimation of Arrhenius constant and for better understanding of the influence of char thermal history on its conversion rates, if the char specific surface area would be determined by gas adsorption techniques rather than the mercury porosimetry;

- The proposed improvement of the SPM model, which could be used in CFD-based models of a fluidized bed boiler, would be to add a factor, which takes into account attrition of the particle;

- Because the 0D SCM, in which chemical kinetics is applied, has been found not to calculate char conversion rates properly at later stages of combustion, thus it could be beneficial for accuracy improvement of the model to introduce the change of many parameters with the particle radius. The second possible way of improving prediction of the SCM is to modify the model in such a way that at a certain char burnout the kinetics influence on carbon conversion rates will be artificially decreased, thus allowing for a faster char conversion at later stages of combustion;

- In case of the 2D model, further calculations are required as the entire particle combustion period should be compared with the experiments. The model accuracy would be increased if moisture and volatiles release would be simulated.

Appendix A

Correction to temperature readings due to thermal radiation

Direct gas temperature measurements using a thermocouple are only possible when the walls, which surround the thermocouple bead have the same temperature as the gas. In the present study temperature of the inner wall of the pipe is lower than gas temperature, because of a poor isolation of the pipe (see Fig. 4.2). In that situation, radiative heat transfer between thermocouple bead and surrounding walls occurs.

After insertion of the thermocouple in the hot gas flow in the place, which is occupied normally by the particle (as shown in Fig. 4.3), the thermocouple bead is heated up by convection. When the temperature of this bead is greater than walls temperature, the heat loss due to radiation occurs. After a certain time, the bead temperature does not change any more. At this time the heat losses due to radiation is compensated by the heat gain due to convection. At that point the following energy conservation equation can be written:

$$\alpha \cdot S_{bead} \cdot (T_g - T_{tbead}) = \epsilon_{aver} \cdot \sigma \cdot S_{bead} \cdot (T_{tbead}^4 - T_{wall}^4) \tag{A.1}$$

where:

α	- convective heat transfer coefficient,	$W/(m^2 \cdot K)$
S_{tbead}	- surface of the thermocouple bead,	m^2
ϵ_{aver}	- emissivity of the thermocouple bead-wall arrangement,	-
σ	- Stefan-Boltzmann constant,	$W/(m^2 \cdot K^4)$
T_g	- gas temperature,	K
T_{tbead}	- thermocouple bead temperature,	K
T_{wall}	- pipe internal surface temperature,	K

Because the convective heat transfer coefficient is depended also on the fluid temperature, the Equation A.1 cannot be solved analytically. Therefore, in order to calculate gas velocity and real gas temperature an iterative procedure has to be undertaken. α can be calculated from Equation A.2.

$$\alpha = \mathtt{Nu} \cdot \lambda_b / d_{tbead} \tag{A.2}$$

where:

$\mathtt{Nu}$	- Nusselt number,	–
λ_b	- gas thermal conductivity at temperature of gas,	$W/(m \cdot K)$
d_{tbead}	- diameter of thermocouple bead,	m

Assuming the spherical thermocouple ending, the Nusselt number can be calculated as [64]:

$$\mathtt{Nu} = 2 + 0.6 \cdot \mathtt{Re}^{0.5} \cdot \mathtt{Pr}^{0.33} \tag{A.3}$$

where:

$\mathtt{Re}$	- Reynolds number,	–
$\mathtt{Pr}$	- Prandtl number,	–

The Prandtl ($\mathtt{Pr}$) and Reynolds ($\mathtt{Re}$) numbers are evaluated for gas bulk temperature. The Reynolds number is calculated according to:

$$\mathtt{Re} = w \cdot d_{tbead} \cdot \rho_g / \mu_b \tag{A.4}$$

where:

w	- average velocity,	m/s
d_{tbead}	- diameter of the thermocouple bead,	m
ρ_g	- density of gas at bulk temperature and standard pressure,	kg/m^3

The gas velocity can be calculated from continuity equation:

$$w = \dot{V}_b / S_{inner} \tag{A.5}$$

where:

$\dot{V}_b$	- volumetric flow rate at bulk conditions,	m^3/s
S_{inner}	- outlet area of ceramic pipe,	m^2

In order to calculate the volumetric flow rate of gas at bulk temperature, the ideal gas law is used.

$$\dot{V}_b = \dot{V}_{rot} \cdot T_b / T_{rot} \tag{A.6}$$

where:

$\dot{V}_{rot}$	- volumetric flow rate at scaling conditions of rotameter,	m^3/s
T_{rot}	- scaling temperature of rotameter,	K

Emissivity of the thermocouple bead-pipe wall arrangement is evaluated as:

$$\epsilon_{aver} = (1/\epsilon_{tbead} + (S_{tbead}/S_{pipe}) \cdot (1/\epsilon_{pipe} - 1))^{-1} \tag{A.7}$$

where:

S_{pipe}	- surface of the inner surface of steel pipe,	m^2
ϵ_{pipe}	- emissivity of the inner surface of steel pipe,	-
ϵ_{tbead}	- emissivity of the thermocouple bead,	-

The thermocouple bead surface comparing with area of the combustion chamber walls is negligible small, therefore $\epsilon_{aver} \rightarrow \epsilon_{tbead}$.

Table A.1 shows inputs, which are needed for calculation of output variables, presented in Table A.2. The assumed value for thermocouple bead emissivity is obtained through consultation with manufacturer (Czaki Thermo-Product). The average internal surface temperature of the steel pipe is obtained through thermocouple measurements as well as by infrared camera, assuming 0.8 surface emissivity. The obtained gas temperatures have relatively large level of uncertainty. This uncertainty is connected with the measurement of gas temperature using thermocouples. Despite the 0.4% measurement error of the thermocouple [126], the radiation process is significantly simplified in the above calculations. It is assumed that thermocouple ending exchanges the heat with the steel pipe. In reality also the ceramic tube, the part of electric heater interior and objects in the laboratory participate in radiative heat transfer. Moreover, it is assumed that the internal wall surface temperature of the steel pipe has an uniform temperature, which obviously is a simplification. Temperature measurements using thermocouples are always inaccurate, especially at such high temperatures levels.

Table A.1: Input variables

Symbol	**Value**
d_{tbead}	0.001 m
ϵ_{tbead}	0.35
T_{tbead}	1015 K
T_{wall}	600 K
$\dot{V}_{rot}$	$1.394 \cdot 10^{-4}$ m^3/s

Table A.2: Output variables

Symbol	**Value**
`Re`	24.7
`Nu`	4.67
α	328 $W/(m^2 \cdot K)$
T_g	1069 K
$\dot{V}_{rot}$	$5.08 \cdot 10^{-4}$ m^3/s
w	3.30 m/s

Appendix B

Some photos of char and coal particles used in GTB experiments

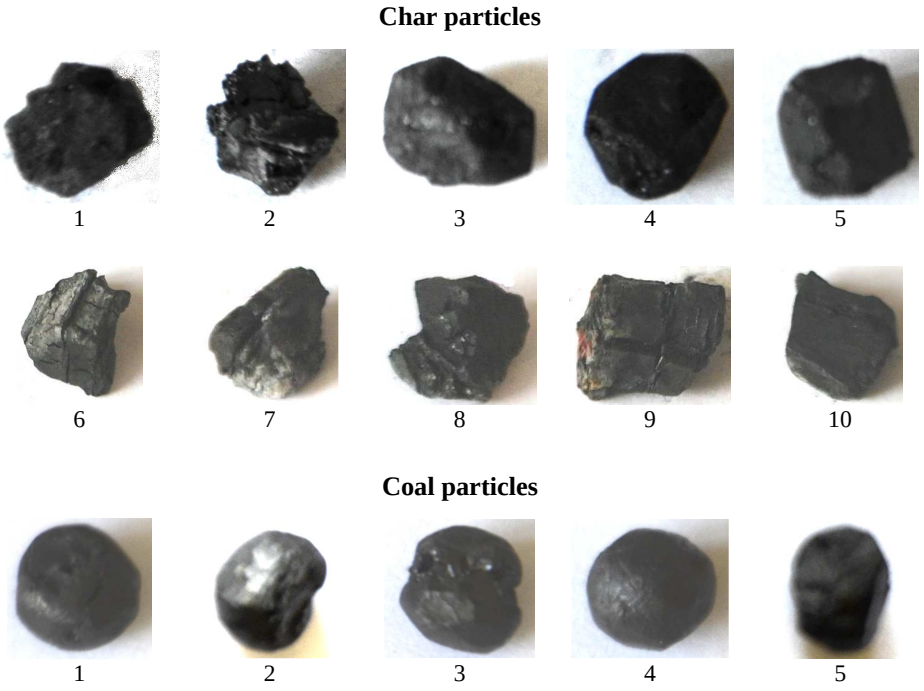

FIGURE B.1: Photos of char (see Table 4.3) and coal (see Table 4.4) particles used in the study

FIGURE B.2: Photos of char (left) and coal (right) particles combustion in GTB

FIGURE B.3: Photos of ash remains from char combustion in GTB

Bibliography

[1] Coal industry across Europe. Technical report, European Association for Coal and Lignite AISBL, November 2013.

[2] Poland - Country analysis note, September 2013. URL http://www.eia.gov/. U.S. Energy Information Agency.

[3] Technology Roadmap; High-efficiency, low-emissions coal-fired power generation. Technical report, International Energy Agency, 2012.

[4] Energy Sector in Poland, 2012. URL www.paiz.gov.pl/publikacje/opracowania_sektorowe. Polish Information and Foreign Invesment Agency.

[5] H. Andruleit, A. Bahr, H. G. Babies, D. Franke, J. Messner, R. Pierau, M. Schauer, S. Schmidt, and S. Weihmann. Energiestudie 2013 reserven, ressourcen und verfugbarkeit von energierohstoffen. Technical report, The Federal Institute for Geosciences and Natural Resources (BGR), December 2013.

[6] Key World Energy Statistics 2013. Technical report, International Energy Agency, 2013.

[7] A strategy for clean coal. Technical report, European Association for Coal and Lignite AISBL, November 2012.

[8] Germany's new energy policy. Heading towards 2050 with secure, affordable and environmentally sound energy, May 2013. URL www.efficiency-from-germany.info/EIE/Navigation/EN/downloads.html.

[9] H.-J. Feuerborn and S. Gohring. Status for new power plants and by-products in Europe. Technical report, VGB/ECOBA for ASHTRANS, April 2013.

[10] R. Scholz, M. Beckmann, Ch. Pieper, M. Muster, and R. Weber. Considerations on providing the energy needs using exclusively renewable sources: Energiewende in Germany. *Renewable and Sustainable Energy Reviews*, 35:109–125, 2014.

[11] T. Olkuski. Analysis of domestic reserves of steam coal in the light of its use in power industry. *Gospodarka Surowcami Mineralnymi*, 29:25–38, 2013.

[12] Ministerstwo Administracji i Cyfryzacji. Polska 2030. Trzecia fala nowoczesności. Długookresowa strategia rozwoju kraju. Available online 17.03.2014, November 2012. URL mac.gov.pl/files/wp-content/uploads/2013/02/Strategia-DSRK-PL2030-RM.pdf.

[13] Ministerstwo Gospodarki. Polityka energetyczna Polski do 2030 roku, November 2009. Załącznik do uchwały nr 202/2009 Rady Ministrów z dnia 10 listopada 2009 r.

[14] S. Jenkins and G. Brown. A Comparison of PC, CFB and IGCC Technologies for Basin Electric Power Cooperative's Dry Fork Station. Technical report, Basin Electric Power Cooperative, June 2007. CH2M HILL, INC.

[15] F. Johnsson. Fluidized Bed Combustion for Clean Energy. In *The 12th International Conference on Fluidization - New Horizons in Fluidization Engineering*, pages 47–62, 2007.

[16] W. Kordylewski, E.M. Bulewicz, A. Dyjakon, T. Hardy, S. Słupek, R. Miller, and A. Wanik. *Spalanie i paliwa*. Oficyna Wydawnicza Politechniki Wrocławskiej, 2008. ISBN 9788374933780.

[17] P. Basu. *Combustion and Gasification in Fluidized Beds*. Taylor & Francis Group, 2006.

[18] C. A. Heidenreich, H. M. Yan, and D. K. Zhang. Mathematical modelling of pyrolysis of large coal particles - estimation of kinetic parameters for methane evolution. *Fuel*, 78: 557–566, 1999.

[19] H. Spliethoff. *Power Generation from Solid Fuels*. Power Systems. Springer, 2010.

[20] T. Cukiernik. Parametry nadkrytyczne w technologii fluidalnej. *Pracodawca*, 1 (157): 6–8, January 2011.

[21] S. Teir. Modern Boiler Types and Applications. available online 19.03.2014, 2002. URL http://www.energy.kth.se/compedu/webcompedu/ManualCopy/Steam_Boiler_Technology/Modern_boiler_applications/modern_boiler_types_and_applications.pdf. Energy Engineering and Environmental Protection Publications.

[22] W. Nowak. Fluidized Bed Technology in Research and Application - Part i. Clean Industrial Fuel Utilization Seminar, March 2011.

[23] R. Wilk. *Low-emission combustion*. Wydawnictwo Politechniki Śląskiej, 2002.

[24] M. Bujny, P. Burmistrz, S. Gruszka, W. Janicki, K. Kogut, and A. Strugała. Instalacja demonstracyjna do monitorowania i redukcji emisji rtęci ze spalania węgla kamiennego w kotłach pyłowych. *Polityka Energetyczna*, 15:161–174, 2012.

[25] T. Dziok, A. Strugała, and A. Rozwadowski. Badania zawartości rtęci w węglu - uwagi dotyczące sposobu prezentacji wyników. *Polityka Energetyczna*, 16:273–285, 2013.

[26] IPCC. *Climate Change 2013: The Physical Science Basis. Contribution of Working Group I to the Fifth Assessment Report of the Intergovernmental Panel on Climate Change*. Cambridge University Press, 2013.

[27] World Economic Outlook. Transitions and Tensions. Technical report, International Monetary Fund, 2013.

[28] Natural gas prices in selected countries as of June 1, 2012, available online March 2014. URL www.statista.com/statistics/253047/natural-gas-prices-in-selected-countries/.

[29] Electricity prices in selected countries as of June 1, 2012, available online March 2014. URL http://www.statista.com/statistics/263492/electricity-prices-in-selected-countries/.

[30] N. M. Laurendeau. Heterogeneous kinetics of coal char gasification and combustion. *Progress in Energy and Combustion Science*, 4:221–270, 1978.

[31] I. W. Smith. The combustion rates of coal chars: A review. *Proceedings of the Combustion Institute*, 19:1045–1065, 1982.

[32] Y. B. Yang, V. N. Sharifi, J. Swithenbank, L. Ma, L. I. Darvell, J. M. Jones, M. Pourkashanian, and A. Williams. Combustion of a single particle of biomass. *Energy & Fuels*, 22: 306–316, 2008.

[33] C. Wendt, C. Eigenbrod, O. Moriue, and H. J. Rath. A model for devolatilization and ignition of an axisymmetric coal particles. *Proceedings of the Combustion Institute*, 29: 449–457, 2002.

[34] A. M. Carpenter and N. M. Skorupka. Coal combustion - analysis and testing. Technical report, IEA Coal Research, November 1993.

[35] R. Buczyński. *Investigation of Fixed-Bed Combustion Process in Small Scale Boilers*. PhD thesis, Silesian University of Technology and Clausthal University of Technology, 2011.

[36] R. Buczyński, R. Weber, A. Szlęk, and R. Nosek. Time-dependent combustion of solid fuels in a fixed-bed: Measurements and mathematical modeling. *Energy & Fuels*, 26: 4767–4774, 2012.

[37] R. Buczyński, R. Weber, and A. Szlęk. Innovative design solutions for small-scale domestic boilers; Combustion improvements using a CFD-based mathematical model. Journal of the Energy Institute, 2014.

[38] A. Szlęk. Badania procesu spalania paliw stałych w warstwie nieruchomej, 2001. Zeszyty Naukowe Politechniki Śląskiej, Energetyka, z. 135.

[39] R. Bońda, D. Brzeziński, M. Czapigo-Czapla, G. Czapkowski, J. Dyląg, A. Malon, S. Z. Mikulski, W. Miśkiewicz, S. Oszczepalski, A. Piotrowska, D. Siekierka, L. Skrzypczyk, J. Sokołowski, W. Szczygielski, M. Szuflicki, M. Tymiński, and A. Wałkuska. Bilans zasobów złóż kopalin w Polsce wg stanu na 31 xii 2012 r. Technical report, Państwowy Instytut Geologiczny - Państwowy Instytut Badawczy, 2013.

[40] March 2014. URL www.tauron-wydobycie.pl/spolka/zg-janina/charakterystyka-zakladu.

[41] M. Wilczyński. Zmierzch węgla kamiennego w Polsce. Technical report, Fundacja Instytut na rzecz Ekorozwoju, 2013.

[42] M. Wasilewska. *Struktura zmienności parametrów złóż węgla kamiennego w wybranych kopalniach Górnośląskiego Zagłębia Węglowego*. PhD thesis, Akademia Górniczo-Hutnicza im. Stanisława Staszica, 2007.

[43] M. Radovanowic, editor. *Fluidized bed combustion*. Hemisphere Publishing Corporation, 1986.

[44] J.-S. Chern and A. N. Hayhurst. A model for the devolatilization of a coal particle sufficiently large to be controlled by heat transfer. *Combustion and Flame*, 146:553–571, 2006.

[45] B. A. Adesanya and H. N. Pham. Mathematical modelling of devolatilization of large coal particles in a convective environment. *Fuel*, 74:896–902, 1995.

[46] M. Komatina, V. Manovic, and A. Saljnikov. Temperatures of coal particle during devolatilization in fluidized bed combustion reactor. *Energy Sources, Part A*, 28:1387–1396, 2006.

[47] F. Winter, M. E. Prach, and H. Hofbauer. Temperatures in a fuel particle burning in a fluidized bed: The effect of drying, devolatilization, and char combustion. *Combustion and Flame*, 108:302–314, 1997.

[48] A. K. Sadhukhan, P. Gupta, and R. K. Saha. Modeling and experimental studies on single particle coal devolatilization and residual char combustion in fluidized bed. *Fuel*, 90: 2132–2141, 2011.

[49] D.P. Ross, C.A. Heidenreich, and D.K. Zhang. Devolatilisation times of coal particles in a fluidised-bed. *Fuel*, 79:873–883, 2000.

[50] C. A. Heidenreich and D. K. Zhang. Measuring the temperature response of large wet coal particles during heating. *Fuel*, 78:991–994, 1999.

[51] C. N. Eatough and L. D. Smoot. Devolatilization of large coal particles at high pressure. *Fuel*, 75:1601–1605, 1996.

[52] G. H. Wood Jr., T. M. Kehn, M. Devereux Carter, and W. C. Culbertson. Coal Resource Classification System of the U.S. Geological Survey. Technical report, Geological Survey, 1983.

[53] H. Gao, Jicheng H., and M. Nomura. Devolatilization characteristics of coal particles heated with a CO_2 laser controlled by double shutters: A simulation investigation. *Energy & Fuels*, 24:18–28, 2010.

[54] P.R. Solomon, D.G. Hamblen, R.M. Carangelo, M.A. Serio, and G.V. Deshpande. A general model of coal devolatilization. Technical report, Advanced Fuel Research Inc., 1988.

[55] B. Remiarova, J. Markos, R. Zajdlik, and L. Jelemensky. Identification of the mechanism of coal char particle combustion by porous structure characterization. *Fuel Processing Technology*, 85:303–321, 2004.

[56] V. Manovic, M. Komatina, and S. Oka. Modeling the temperature in coal char particle during fluidized bed combustion. *Fuel*, 87:905–914, 2008.

[57] A. K. Sadhukhan, P. Gupta, and R. K. Saha. Characterization of porous structure of coal char from a single devolatilized coal particle: Coal combustion in a fluidized bed. *Fuel Processing Technology*, 90:692–700, 2009.

[58] K. Holikova, R. Zajdlik, J. Markos, and L. Jelemensky. Comparison of single coal char particle combustion at different conditions. *Chemical Papers*, 59(6a):413–420, 2005.

[59] A. N. Hayhurst and M. S. Parmar. Measurement of the mass transfer coefficient and Sherwood number for carbon spheres burning in a bubbling fluidized bed. *Combustion and Flame*, 130:2002, 2002.

[60] F. Scala. Fluidized-bed combustion of single coal char particles: An analysis of the burning rate and of the primary CO/CO_2 ratio. *Energy & Fuels*, 25:1051–1059, 2011.

[61] F. Scala and R. Chirone. Fluidized bed combustion of single coal char particles at high CO_2 concentration. *Chemical Engineering Journal*, 165:902–906, 2010.

[62] R. Zajdlik, L. Jelemensky, B. Remiarova, and J. Markos. Experimental and modelling investigations of single coal particle combustion. *Chemical Engineering Science*, 56: 1355–1361, 2001.

[63] M. Komatina, V. Manovic, and D. Dakic. An experimental study of temperature of burning coal particle in fluidized bed. *Energy & Fuels*, 20:114–119, 2006.

[64] I. Guedea, D. Pallares, L. I. Diez, and F. Johnsson. Conversion of large coal particles under O_2/N_2 and O_2/CO_2 atmospheres - experiments and modeling. *Fuel Processing Technology*, 112:118–128, 2013.

[65] M. J. Biggs and P. K. Agarwa. The CO/CO_2 product ratio for a porous char particle within an incipiently fluidized bed: a numerical study. *Chemical Engineering Science*, 52:941–952, 1997.

[66] A. Gomez-Barea, P. Ollero, and R. Arjona. Reaction-diffusion model of TGA gasification experiments for estimating diffusional effects. *Fuel*, 84:1695–1704, 2005.

[67] K. Svoboda, M. Hartman, M. Pohorely, and O. Tranka. Modelling of effects of operating conditions and coal reactivity on temperature of burning particles in fluidized bed combustion. *Acta Geodynamica et Geomaterialia*, 1:261–274, 2004.

[68] T. H. Fletcher, L. L. Baxter, and D. K. Ottesen. Spectral emission characteristics of size-graded coal particles. Technical report, Sandia National Laboratories, 1987.

[69] W. Gajewski and A. Kijo-Kleczkowska. Analysis of combustion of solid fuels in the fluidized bed. *Archivum Combustionis*, 25:65–84, 2005.

[70] A. A. Malik, D. Pehlivan, and C. R. Howarth. The effect of agitation on the char combustion characteristics of large coal particles. *Fuel*, 75:379–383, 1996.

[71] P. Pełka. Analysis of mass loss of a coal particle during the course of burning in a flow of inert material. *Combustion and Flame*, 156:1604–1613, 2009.

[72] P. Pełka. Modelling of mass loss of char particles during combustion in flow of inert material. *Fuel*, 90:932–940, 2011.

[73] S. Ulzama. *A Theoretical Analysis of Single Coal Particle Behavior during Spontaneous Devolatilization and Combustion*. PhD thesis, Otto von Guericke University Magdeburg, 2007.

[74] R. Weber. Extracting mathematically exact kinetic parameters from experimental data on combustion and pyrolysis of solid fuels. *Journal of the Energy Institute*, 81:226–233, 2008.

[75] *Netzsch Thermal Analysis Instrument Manual*.

[76] P. Ollero, A. Serrera, R. Arjona, and S. Alcantarilla. Diffusional effects in TGA gasification experiments for kinetic determination. *Fuel*, 81:1989–2000, 2002.

[77] B. Nowak, O. Karlstrom, P. Backman, A. Brink, M. Zevenhoven, S. Voglsam, F. Winter, and M. Hupa. Mass transfer limitation in thermogravimetry of biomass. *Journal of Thermal Analysis and Calorimetry*, 111:183–192, 2012.

[78] L. Gasparovic, Z. Korenova, and L. Jelemensky. Kinetic study of wood chips decomposition by TGA. In *36th International Conference of Slovak Society of Chemical Engineering*, 2009.

[79] A. Gomez-Barea, P. Ollero, and C. Fernandez-Baco. Diffusional effects in CO_2 gasification experiments with single biomass char particles. 1. Experimental investigation. *Energy & Fuels*, 20:2202–2210, 2006.

[80] A. Zolin, A. D. Jensen, P. A. Jensen, and K. Dam-Johansen. Experimental study of char thermal deactivation. *Fuel*, 81:1065–1075, 2002.

[81] H. Sis. Evaluation of combustion characteristics of different size elbistan lignite by using TG/DTG and DTA. *Journal of Thermal Analysis and Calorimetry*, 88:863–870, 2007.

[82] S. Brunello, I. Flour, P. Maissa, and B. Bruyet. Kinetic study of char combustion in a fluidized bed. *Fuel*, 75:536–544, 1996.

[83] D. G. Roberts and D. J. Harris. Char gasification with O_2, CO_2, and H_2O: Effects of pressure on intrinsic reaction kinetics. *Energy & Fuels*, 14:483–489, 2000.

[84] G. Hakvoort, J. C. Schouten, and P. J. M. Valkenburg. The determination of coal combustion kinetics with thermorgavimetry. *Journal of Thermal Analysis*, 35:335–346, 1989.

[85] L. Kelebopile, R. Sun, H. Wang, X. Zhang, and S. Wu. Pore development and combustion behavior of gasified semi-char in a drop tube furnace. *Fuel Processing Technology*, 111: 42–54, 2013.

[86] N. V. Russell, J. R. Gibbins, C. K. Man, and J. Williamson. Coal char thermal deactivation under pulverized fuel combustion conditions. *Energy & Fuels*, 14:883–888, 2000.

[87] A. Zolin, A. Jensen, and K. Dam-Johansen. Kinetic analysis of char thermal deactivation. *Proceedings of the Combustion Institute*, 28:2181–2188, 2000.

[88] W. C. Hecker, K. M. McDonald, W. Reade, M. R. Swensen, and R. F. Cope. Effect of burnout on char oxidation kinetics. *Proceedings of the Combustion Institute*, 24:1225–1231, 1992.

[89] D. G. Roberts, E. M. Hodge, D. J. Harris, and J. F. Stubington. Kinetics of char gasification with CO_2 under regime II conditions: Effects of temperature, reactant, and total pressure. *Energy & Fuels*, 24:5300–5308, 2010.

[90] G. Chen, Q. Yu, and K. Sjostrom. Reactivity of char from pyrolysis of birch wood. *Journal of Analytical and Applied Pyrolysis*, 40-41:491–499, 1997.

[91] O. Karlstrom, A. Brink, E. Biagini, M. Hupa, and L. Tognotti. Comparing reaction orders of anthracite chars with bituminous coal chars at high temperature oxidation conditions. *Proceedings of the Combustion Institute*, 34:2427–2434, 2013.

[92] J.R. Arthur. Reactions between carbon and oxygen. *Transactions of the Faraday Society*, 47:164–178, 1951.

[93] C. Chen and T. Kojima. Single char particle combustion at moderate temperature: Effects of ash. *Fuel Processing Technology*, 47:215–232, 1996.

[94] H. R. Batchelder, R. M. Busche, and W. P. Armstrong. Kinetics of coal gasification. *Industrial and Engineering Chemistry*, 45:1856–1878, 1953.

[95] A. Jess and A.-K. Andresen. Influence of mass transfer on thermogravimetric analysis of combustion and gasification reactivity of coke. *Fuel*, 89:1541–1548, 2010.

[96] S. K. Bhatia and D. D. Perlmutter. A random pore model for fluid-solid reactions: 1. Isothermal, kinetic control. *AIChE Journal*, 26:379–386, 1980.

[97] B. Feng and S. K. Bhatia. Variation of the pore structure of coal chars during gasification. *Carbon*, 41:507–523, 2003.

[98] P. A. Webb. An introduction to the physical characterization of materials by mercury intrusion porosimetry with emphasis on reduction and presentation of experimental data. Technical report, Micromeritics Instrument Corp., 2001.

[99] T. DeSousa and P. A. Webb. Special section/instrumentation: Mercury intrusion porosimetry. *Ceramic Industry*, June 2010.

[100] P. A. Webb and C. Orr. Modern methods of particle characterization. www.micromeritics.com, available online on March 2014.

[101] L. Jelemensky, R. Zajdlik, J. Markos, and B. Remiarova. Modeling of coal particle combustion. *Acta Montanistica Slovaca*, 3:295–300, 1998.

[102] C.R. Clarkson and R.M. Bustin. The effect of pore structure and gas pressure upon the transport properties of coal: a laboratory and modeling study. 1. Isotherms and pore volume distributions. *Fuel*, 78:1333–1344, 1999.

[103] S. Katta and D. L. Keairns. Char reactivities and their relationship to pore characteristics. Technical report, Westinghouse R&D Center, 1980.

[104] *AutoPore IV Series Automated Mercury Porosimeters*. Micromeritics Instrument Corporation, www.micromeritics.com, available online in March 2014.

[105] E. Sima-Ella, G. Yuan, and T. Mays. A simple kinetic analysis to determine the intrinsic reactivity of coal chars. *Fuel*, 84:1920–1925, 2005.

[106] B. Arias, C. Pevida, F. Rubiera, and J. J. Pis. Changes in coal char reactivity and texture during combustion in an entrained flow reactor. *Journal of Thermal Analysis and Calorimetry*, 90:859–863, 2007.

[107] F. Chejne and J. P. Hernandez. Modelling and simulation of coal gasification process in fluidized bed. *Fuel*, 81:1687–1702, 2002.

[108] R. C. Everson, H. W. J. P. Neomagus, and D. Njapha. Kinetic analysis of non-isothermal thermogravimetric analyser results using a new method for the evaluation of the temperature integral and multi-heating rates. *Fuel*, 85:418–422, 2006.

[109] A. Mianowski, Z. Robak, M. Tomaszewicz, and S. Stelmach. The Boudouard-Bell reaction analysis under high pressure conditions. *Journal of Thermal Analysis and Calorimetry*, 110:93–102, 2012.

[110] W.-B. Fu, Y.-P. Zhan, and H.-Q. Han. *Coal Combustion: Science and Technology of Industrial and Utility Applications*, chapter : A Generalized Devolatilization Model for Large Coal Particles in Fluidized-Bed, pages 121–129. Hemisphere Publishing, 1988.

[111] C. L. Sun, Y. 0. Xiong, Q. X. Liu, and M. Y. Zhang. Thermogravimetric study of the pyrolysis of two Chinese coals under pressure. *Fuel*, 76:639–644, 1997.

[112] URL kinetics.nist.gov/janaf.

[113] D. Merrick. Mathematical models of the thermal decomposition of coal: 2. specific heats and heats of reaction. *Fuel*, 62(5):540 – 546, 1983. ISSN 0016-2361. doi: http://dx.doi.org/10.1016/0016-2361(83)90223-5. URL http://www.sciencedirect.com/science/article/pii/0016236183902235.

[114] B. Leśniak, L. Słupik, and G. Jakubina. The determination of the specific heat capacity of coal based on literature data. *Chemik*, 67:560–571, 2013.

[115] E. W. Thiele. Relation between Catalytic Activity and Size of Particle. *Industrial & Engineering Chemistry*, 31:916–920, July 1939.

[116] B. Peters, A. Dziugys, and R. Navakas. A shrinking model for combustion/gasification of char based on transport and reaction time scales. *Mechanika*, 18:177–185, 2012.

[117] W. E. Ranz and W. R. Marshall. Evaporation from drops. *Chemical Engineering Progress*, 48:141–146, March 1952.

[118] F. P. Incropera, D. P. Dewitt, T. L. Bergman, and A. S. Lavine. *Fundamentals of Heat and Mass Transfer. Sixth edition*. John Wiley & Sons, 2007.

[119] H. M. Tolvanen, L. I. Kokko, and R. Raiko. The factors controlling combustion and gasification kinetics of solid fuels. In *Challenges in Combustion Technology today*. The National Committees of Sweden and Finland of the International Flame Research Foundation and the Scandinavian-Nordic Section of the Combustion Institute, 26-27 January 2011. Swedish-Finnish Flame Days, Pitea, Sweden.

[120] Y. Shuang, C. Wu, B. Yan, and Y. Cheng. Heat transfer inside particles and devolatilization for coal pyrolysis to acetylene at ultrahigh temperatures. *Energy & Fuels*, 24:2991–2998, 2010.

[121] B. Atkinson and D. Merrick. Mathematical models of the thermal decomposition of coal: 4. heat transfer and temperature profiles in a coke-oven charge. *Fuel*, 62(5):553 – 561, 1983. ISSN 0016-2361. doi: http://dx.doi.org/10.1016/0016-2361(83)90225-9. URL http://www.sciencedirect.com/science/article/pii/0016236183902259.

[122] C. R. Wilke. Diffusional properties of multicomponent gases. *Chemical Engineering Progress*, 46:95–104, 1950.

[123] J. R. Welty, Ch. E. Wicks, R. E. Wilson, and G. L. Rorrer. *Fundamentals of momentum, heat and mass transfer*. John Wiley & Sons, Inc., 5th edition edition, 2008.

[124] *Ansys Fluent 14.5 User's Guide*.

[125] P. Edge, M. Gharebaghi, R. Irons, R. Porter, R. T. J. Porter, M. Pourkashanian, D. Smith, P. Stephenson, and A. Williams. Combustion modelling opportunities and challenges for oxy-coal carbon capture technology. *Chemical Engineering Research and Design*, 89: 1470–1493, 2011.

[126] URL http://www.czaki.pl/czaki2/plik/czaki-wsparcie-techniczne-czujniki_termoelektryczne-pdf_nn3272.pdf.